NASA-CR-193227

GRANT
IN-32-CR
171488
P. 100

Development of a 9.3 µm CW Lidar for the study of atmospheric aerosol

FINAL TECHNICAL REPORT
NASA NAG8-766

B. N. Whiteside
R. M. Schotland

Institute of Atmospheric Physics
The University of Arizona, Tucson, Arizona 85721

Research Period
February 14, 1989 to January 12, 1993

June 29, 1993

(NASA-CR-193227) DEVELOPMENT OF A
9.3 MICROMETER CW LIDAR FOR THE
STUDY OF ATMOSPHERIC AEROSOL Final
Technical Report, 14 Feb. 1989 - 12
Jan. 1993 (Arizona Univ.) 100 p

N93-29105

Unclas

G3/32 0171488

TABLE OF CONTENTS

CHAPTER

CHAPTER Page

LIST OF ILLUSTRATIONS

LIST OF TABLES

ABSTRACT

This report provides a brief summary of the basic requirements to obtain coherent or heterodyne mixing of the optical radiation backscattered by atmospheric aerosols with that from a fixed frequency source. The CW mode of operation for a coherent lidar is reviewed along with the associated lidar transfer equation.

A complete optical design of the three major subsystems of a CW, coherent lidar is given. Lens design software is implemented to model and optimize receiver performance.

Techniques for the opto-mechanical assembly and some of the critical tolerances of the coherent lidar are provided along with preliminary tests of the subsystems. Included in these tests is a comparison of the experimental and the theoretical average power signal-to-noise ratio.

The analog to digital software used to evaluate the power spectrum of the backscattered signal is presented in the Appendix of this report.

CHAPTER 1

INTRODUCTION

1.1 Objectives

The motivation for this research was a need by NASA for a portable, coherent lidar which would be capable of sensing the extremely low power backscattered by atmospheric aerosols. The sensor described in this paper needed to be small and lightweight to permit remote field studies, in order to gather useful data in support of NASA's LAWS program.

1.2 Coherent LIDAR

A coherent laser radar or coherent LIDAR (which stands for *li*ght *d*etecting *a*nd *r*anging) is a device which enables a precise means of determining both the position and velocity of a target. A coherent lidar optically mixes the extremely low power backscattered from the atmospheric aerosol with a much higher power local oscillator, enabling the detection of aerosols with extremely small scattering cross sections.

A coherent lidar in its simplest conception consists of a Twyman-Green Interferometer which has been modified into a Fourier-Transform Spectrometer as shown below in Figure 1.1. Instead of using a test mirror, as in the case of a Twyman-Green Interferometer, randomly located scattering centers produce the reflected beam in the test arm of the interferometer. Depending on the optical path difference, constructive or destructive interference will take place at the photodetector plane. In order to use this apparatus as a means of determining the velocity of atmospheric winds, the frequency spectrum of the detected signal must be determined. In other words, this instrument must operate as a spectrometer. Since all of the radiation captured by the system is analyzed simultaneously, a Fourier Transform operation must be performed on the electrical signal produced within the photodetector, in order to separate the various frequency components.

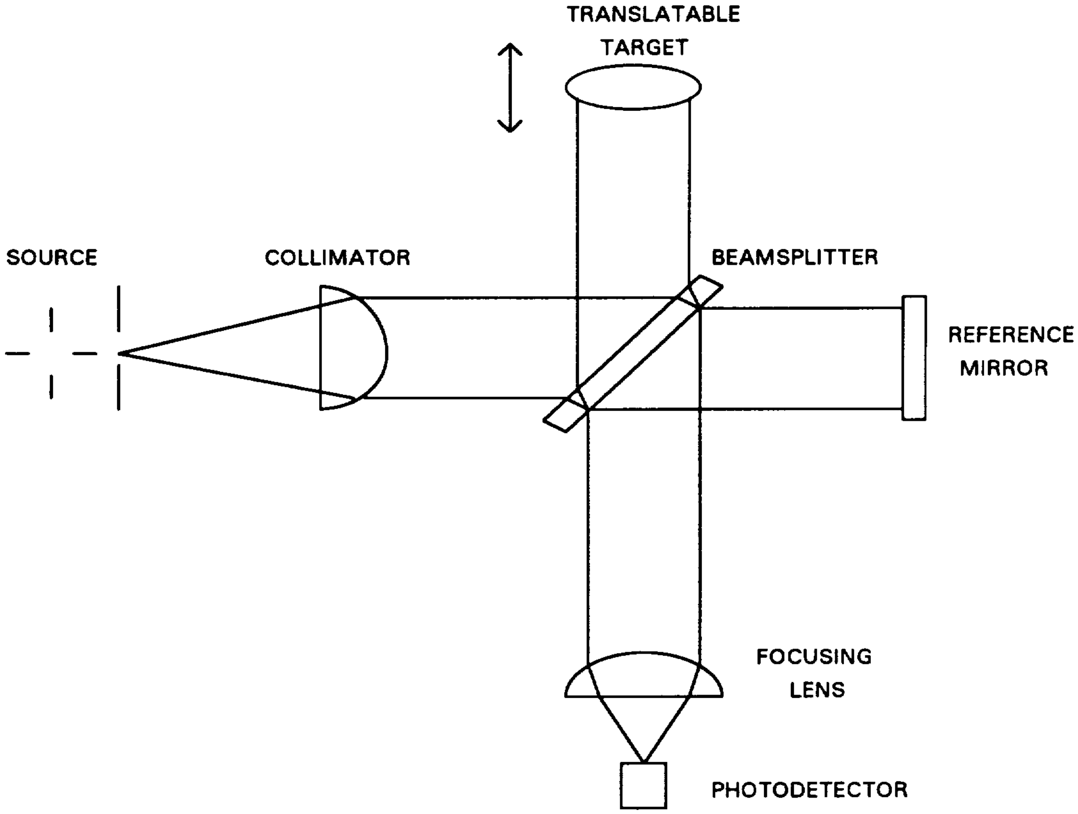

Figure 1.1. Fourier Transform Spectrometer

In order to determine the position of a group of scatterers, two methods are employed. One involves the use of a pulsed laser with range-gated electronics to precisely measure the round trip travel time of the pulse, where the outgoing beam is focused at maximum range. The second method uses a focused continuous-wave beam to precisely define the scattering volume at a fixed location in space. The location of the scattering volume can be scanned over a minimum and maximum range by changing the focusing properties of a laser beam expander.

The coherent lidar which will be described in detail throughout this paper will, in fact, resemble a Mach-Zehnder Interferometer because of a separate path for the transmitter and receiver and because the reference arm, *i.e.*, the local oscillator, does not actually employ a reference mirror to direct the wavefronts back toward the detector. Figure 1.2 shows the separate transmitter, receiver, and local oscillator arms.

Since the power backscattered by the aerosols is proportional to the transmitted power, high-power lasers are required which additionally maintain a high degree of frequency stability, in order to permit optical heterodyning. A CO_2 laser was chosen for the reasons stated above and because these lasers operate in the spectral region near 10.6 μm, where absorption due to the intervening atmospheric molecules is a minimum.

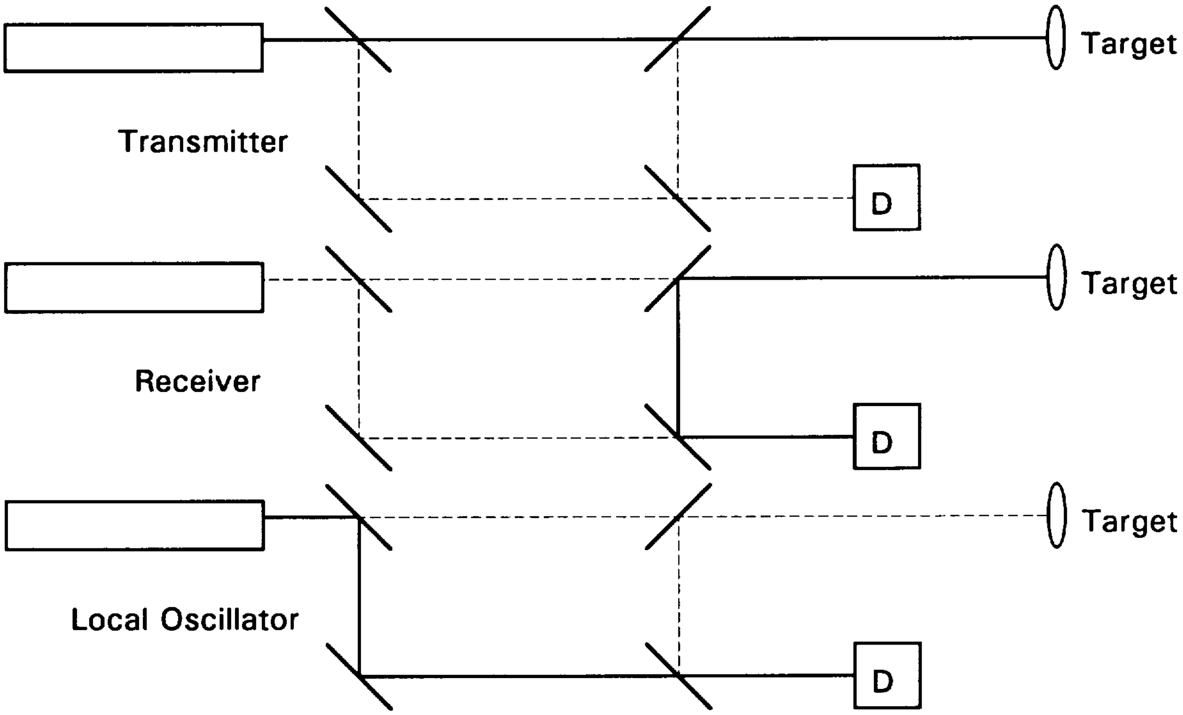

Figure 1.2. Subsystems of modified Mach-Zehnder interferometer

CHAPTER 2

CHARACTERISTICS OF COHERENT LIDAR

Coherent lidar systems are considered to be active sensors, as opposed to passive, since they transmit the radiation which is subsequently scattered by the aerosol and collected again by the receiver. Coherent lidars can not only measure the energy scattered by the target particles, but can additionally determine the velocity of a target by optical mixing or coherent detection. Using this technique involves the comparison of the phase of the scattered signal beam to that of a stable reference beam (Sonnenschein and Horrigan, 1971). The location and volume containing the scattering centers must be known or the information obtained is of little value.

2.1 Coherent Detection

2.1.1 Optical Mixing

Optical mixing is the basis for coherent or heterodyne detection as applied to coherent lidar systems. A single scatterer located a distance r_0 from the lidar will scatter light of a particular phase which is temporally coherent with respect to the incident radiation. The electric field at the detector plane due to this scattered radiation will have a phase shift proportional to the round-trip distance $2r_0$, and the scalar electric field can be written as:

$$E_r = E_{0r} \cos\left[\omega t - (2\pi / \lambda) 2r_0\right] \tag{2.1}$$

If the particle moves with constant velocity, v, in a direction parallel to the transmitted beam, then the phase at the detector plane will change with time and can be written as:

$$E_r = E_{0r} \cos[\omega t - (4\pi / \lambda)(r_0 \pm vt)] \tag{2.2}$$

where the positive sign refers to the particle moving away from the lidar and the negative sign to one moving toward it. The time-dependent terms in the argument can be combined to obtain:

$$E_r = E_{0r} \cos\left[\left\{\omega \mp \frac{4\pi v}{\lambda}\right\} t - \frac{4\pi r_0}{\lambda}\right] \tag{2.3}$$

This constant velocity will produce a doppler shift in the received wave, as compared to the transmitted wave, which is given by:

$$f_D = \pm \frac{2v}{\lambda} \tag{2.4}$$

where the plus sign means that the frequency has increased in the case of a scatterer travelling toward the lidar, and the minus sign means that the frequency has decreased for the case of the scatterer travelling away from the lidar.

Heterodyne detection refers to the fact that two different beams are focused onto the detector. One beam is referred to as the local oscillator, *i.e.*, the original beam of frequency ω_L, and the other is the return or signal beam at frequency $\omega = (\omega_L + \omega_D)$. Since these two beams are temporally coherent, their electric fields will be combined in the detector plane. Because the detector is a square-law detector, the current in the detector will be proportional to the irradiance or the square of the resultant electric field. The two fields can be expressed by:

$$E_L = E_{0L}\cos[\omega_L t - \alpha_L]\ , \qquad E_r = E_{0r}\cos[\{\omega_L + \omega_D\}t - \alpha_r] \tag{2.5}$$

where α_L and α_r represent the initial phases of the fields at time $t = 0$. When these two fields are optically mixed in the plane of the photodetector, the photodetector will measure the average irradiance, where the average is taken over a period long compared to an optical cycle but short compared to the period of the doppler frequency. Thus the cosine squared terms average to 1/2, and thus the resulting detector current will be proportional to:

$$\left\langle [E_L + E_r]^2 \right\rangle = \tfrac{1}{2}\left[E_{0L}^2 + E_{0r}^2 + 2E_{0L}E_{0r}\cos\{\omega_D t - \Delta\alpha\}\right] \tag{2.6}$$

where $\Delta\alpha$ represents the initial phase difference between the two beams, *i.e.*, $\Delta\alpha = \alpha_L - \alpha_r$. Note that the current will have an ac and a dc component, where the first two terms are the dc and the last represent the ac signal, which varies sinusoidally at the doppler frequency. Note also that the sign of the doppler frequency will have no effect on the detected signal, and thus the direction of motion of the scattering center, *i.e.*, toward or away from the lidar, cannot be determined from a transmitted beam with a fixed propagation direction.

In addition, it should also be noted that the ac term in (2.6), which provides the velocity information, has the amplitude of the electric field due to the local oscillator as a factor. Therefore, the signal power spectrum will have an associated heterodyne gain proportional to the power of the local oscillator beam incident on the photodetector. This fact allows the coherent lidar to be sensitive to extremely low energy scattered by atmospheric aerosol.

2.1.2 Phase Front Alignment

The local oscillator and return beams must be aligned very carefully so as not to lose the ac component of the current which carries all the information about the velocity of the target. The phase surfaces of the two beams must be parallel for maximum detection efficiency. In practice, however, perfect alignment is impossible, and so a maximum angular misalignment can be determined. Close to the detector plane, the two beams will have nearly planar phase fronts, but with some finite angular misalignment, θ (see Figure 2.1).

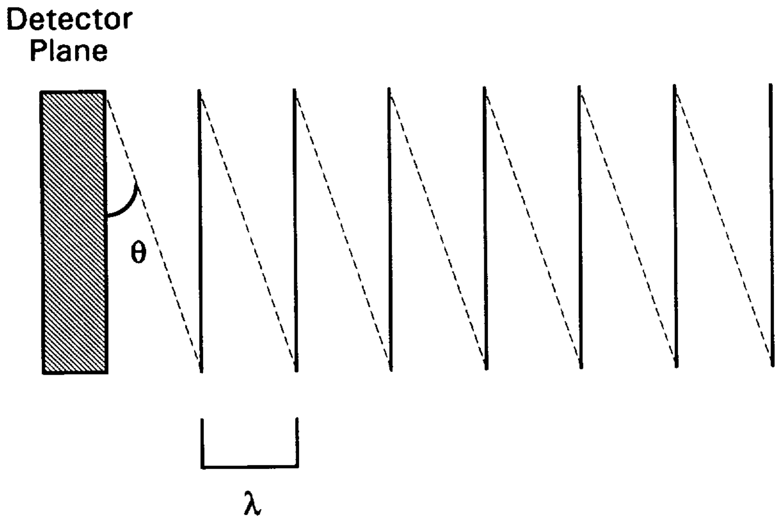

Figure 2.1. Maximum misalignment angle between local oscillator and signal beams

If the two beams are misaligned, as shown above, there will be one complete fringe (bright and dark band for plane waves) on the detector. For a return beam due to a scatterer moving with constant velocity, the phase of the return beam at the detector plane will change with time, as shown below in Figure 2.2. For the misalignment angle shown, there will always be one complete fringe, and thus the detector current will be constant, *i.e.*, the term in (2.6) which represents the ac component remains close to zero for angles greater than or equal to the above misalignment. Thus, in order to have a sinusoidally varying current at the beat frequency, ω_D, the maximum misalignment angle is approximated by:

$$\theta_{\text{misalignment}} \cong \lambda / D_d \tag{2.7}$$

where D_d is the diameter of the detector.

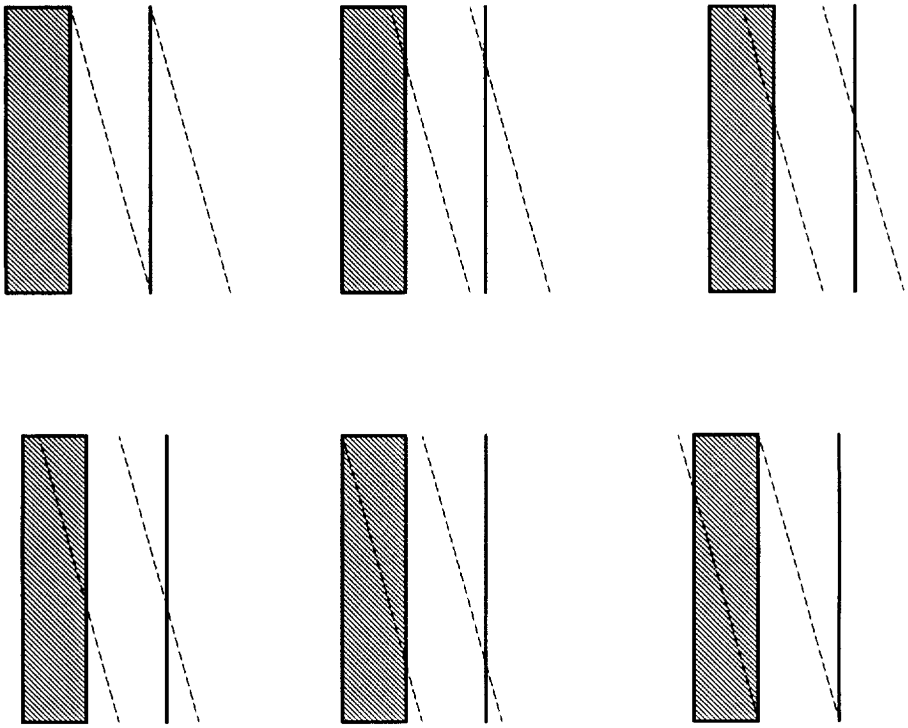

Figure 2.2. Phase change of signal beam with time for maximum misalignment

Because of this misalignment limitation, coherent lidars operated at 10.6 μm are much less affected by misalignment than those operated at 1.06 μm. In addition, coherent lidars must use very small detectors (typically $D_d < 0.3$ mm). For the case of a coherent system with λ = 10.6 μm and D = 0.15 mm, the misalignment tolerance would be:

$$\theta_{\text{misalignment}} < 70.7\text{mrad} \tag{2.8}$$

If equation (2.7) is rewritten in terms of solid angle, the relation:

$$A_d \Omega_r \cong \lambda^2 \tag{2.9}$$

(Siegman, 1966) results, where A_d is the area of the photodetecting surface and Ω_r is the solid angle defined by the allowed cone of the signal beam. Thus, for a given detector area and wavelength, the solid angle subtended by the receiver is limited by the above expression (see Figure 2.3).

2.1.3 Coherent FOV

From Figure 2.3, it can be seen that, because of the invariance of throughput (Wyatt, 1978), equation (2.9) can be rewritten as:

$$A_r \Omega_d \cong \lambda^2 \tag{2.10}$$

where A_r is the area of the receiver plane and Ω_d is the solid angle subtended by the photodetector at the receiver plane. Likewise equation (2.7) can be rewritten as:

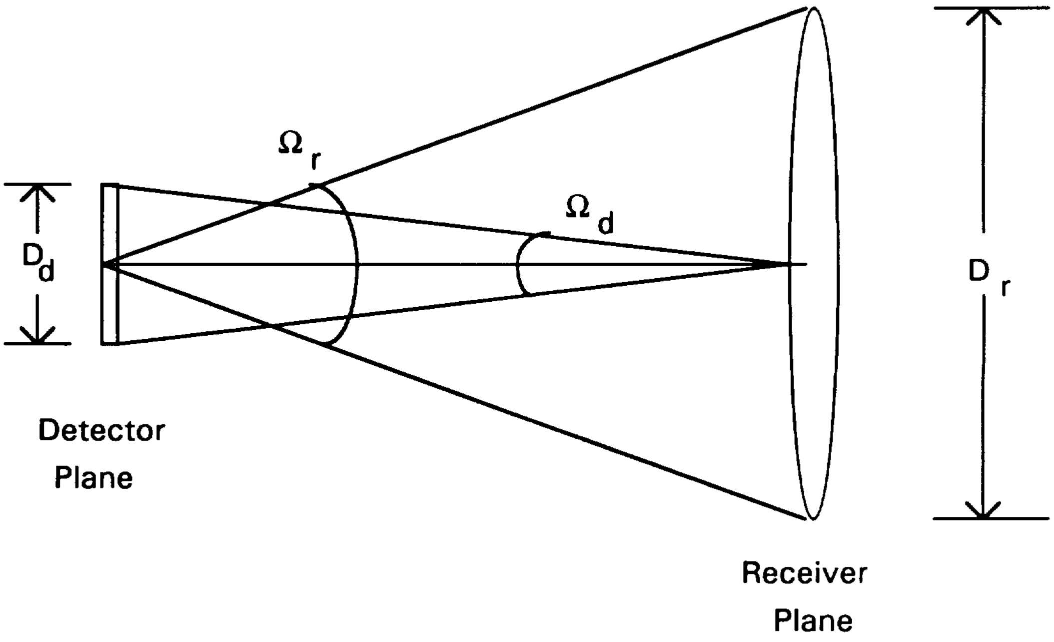

Figure 2.3. Relationship between detector and receiver

$$\theta_{\text{semi-FOV}} \cong \lambda / D_r \tag{2.11}$$

where D_r is the diameter of the receiver. A more rigorous analysis would show that for a circular incoherent source, which is the case for aerosols that are spatially incoherent (Sonnenschein and Horrigan, 1971), the finite, coherent semi-field of view is given by (Saleh and Teich, 1991):

$$\theta_{\text{semi-FOV}} = 1.22\lambda / D_r \tag{2.12}$$

Since the receiver diameter is typically one thousand times larger than the detector diameter, the field of view for a coherent lidar is about one thousand times smaller than (2.8) and so with $\lambda = 10.6$ μm and $D_r = 15$ cm, $\theta_{\text{semi-FOV}}$ will be given by:

$$\theta_{\text{semi-FOV}} = 86.2\ \mu\text{rad} \tag{2.13}$$

Using (2.12), the field height over which the received signal will be coherent at the detector plane is given by:

$$L_{\text{coherence}} = 1.22\lambda f / D_r = 1.22\lambda(f/\#) \tag{2.14}$$

where f is the effective focal length of the receiver (see Figure 2.4).

Note that the coherence length is equal to the radius of the Airy disk. Because each scattering center is a source of spherical waves which are apertured by the receiver, each point source will produce an Airy function irradiance profile at the detector plane. Only the irradiance at the detector plane due to an axial particle will have an Airy disk which is fully coherent (Zhao *et al.*, 1990*a,b*).

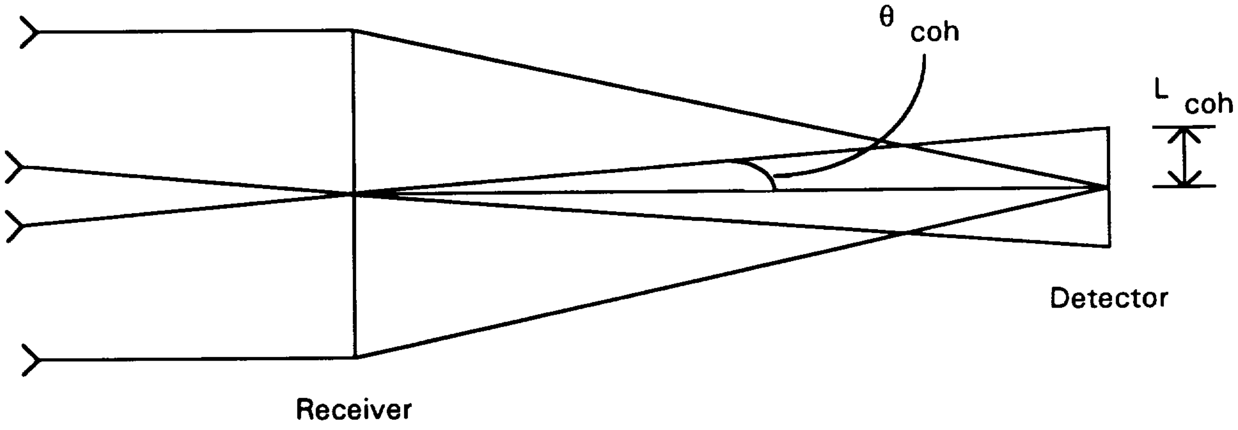

Figure 2.4. Dependence of coherence length at detector plane on the coherent field of view

2.1.4 Spot Size Matching

Looking at (2.6), note that the ac signal term is proportional to the product of the amplitude of the electric fields of the local oscillator and the return beam. Thus, in order to attain the largest ac signal, the product of the electric field amplitudes must be maximized. Assuming that the two beams which are being mixed on the photodetector have Gaussian irradiance profiles, with no net phase difference between the two, their transverse irradiances as a function of the radial distance ρ from the beam axis may be written as:

$$I_1 = I_{01} \exp\left[-2(\rho / w_{01})^2\right], \qquad I_2 = I_{02} \exp\left[-2(\rho / w_{02})^2\right] \qquad \textbf{(2.15)}$$

(Saleh and Teich, 1991), where the symbol, *I*, represents irradiance instead of using the correct symbol, *E* (so as not to confuse irradiance with the electric field), and the waists are located in the plane of the photodetector. I_{01} and I_{02} are the axial irradiances and can be written as:

$$I_{01} = \frac{2P_1}{\pi w_{01}^2} \qquad \text{and} \qquad I_{02} = \frac{2P_2}{\pi w_{02}^2} \tag{2.16}$$

(Saleh and Teich, 1991), where P_1 and P_2 are the total power of beam 1 and beam 2, respectively (which are assumed in the following derivation to be constants). Applying (2.6) and the fact that irradiance is proportional to the square of the amplitude of the electric field (Hecht, 1987), the total power in the detector plane (assuming a plane of infinite extent) will be proportional to:

$$P_{\text{total}} \propto \left(I_{01} I_{02}\right)^{1/2} \int_0^{\infty} \exp\left\{-\rho^2\left(1/w_{01}^2 + 1/w_{02}^2\right)\right\} 2\pi\rho\, d\rho \tag{2.17}$$

which after substituting (2.16) for I_{01} and I_{02}, results in:

$$P_{\text{total}} \propto 1/\left(w_{01} w_{02}\right) \int_0^{\infty} \exp\left\{-\rho^2\left(1/w_{01}^2 + 1/w_{02}^2\right)\right\} \rho\, d\rho \tag{2.18}$$

Upon evaluating (2.18), the total power will be proportional to:

$$P_{\text{total}} \propto \frac{w_{01} w_{02}}{w_{01}^2 + w_{02}^2} \tag{2.19}$$

To determine the relationship between the spot sizes for maximum power detection, the derivative of equation (2.19) is taken with respect to w_{01} when w_{02} is constant, which gives:

$$w_{01}^2 = w_{02}^2 \tag{2.20}$$

and since the spot sizes are real and positive, the only possible solution is:

$$w_{01} = w_{02} \tag{2.21}$$

Thus the spot sizes for two Gaussian beams should be equal even if the two beams have different total powers. Since the product of the two Gaussian electric field profiles will still maintain a Gaussian irradiance profile, the total power in the finite detector plane will increase monotonically for increasing detector radius; thus, beyond a certain radius, the detector current will show little increase. Cohen (1975) shows that, for the case of a backscattered beam with an Airy function irradiance profile and a Gaussian local oscillator irradiance profile, the maximum coherent detection efficiency can be attained when the radius of the Airy disk is 1.4 times the spot size (radius of $1/e^2$ irradiance surface) of the Gaussian beam.

2.1.5 Relationship between Transmitter and Receiver

A coherent lidar can be viewed with the transmitting aperture as shown in Figure 2.5. From this diagram it can be seen that the following expression will hold for a lossless system:

$$A_d\Omega_{r2} = A_r\Omega_d = A_r\Omega_{s2} = A_s\Omega_{r1} = A_s\Omega_t = A_t\Omega_{s1} \tag{2.22}$$

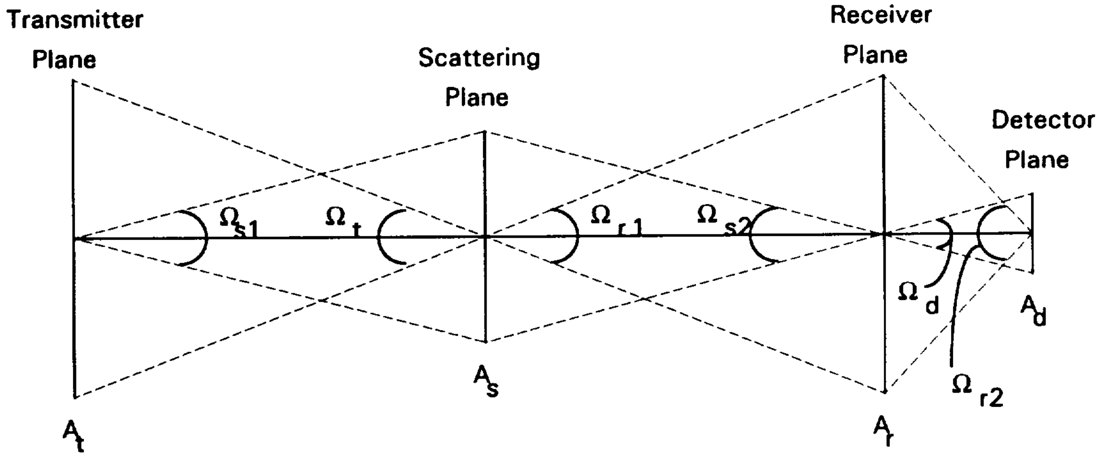

Figure 2.5. Relationship between transmitter and receiver

An equality involving the transmitter and receiver area may be written as:

$$A_t \Omega_{s1} = A_r \Omega_{s2} \tag{2.23}$$

and since $\Omega_{s1} = A_s/R_1^2$ and $\Omega_{s2} = A_s/R_2^2$, where R_1 is the distance from transmitter plane to scattering plane and R_2 is the distance from receiver plane to scattering plane, therefore:

$$\Omega_{s1} = \Omega_{s2} \tag{2.24}$$

for $R_1 = R_2$; therefore, the transmitter and receiver FOV's should be equal. Under these conditions, it is apparent that:

$$A_{\text{transmitter}} = A_{\text{receiver}} \tag{2.25}$$

Thus, the area of the transmitting and receiving apertures should be identical for maximum throughput of energy, and, from the previous discussion, the area of the receiver and the receiver field of view is limited by coherent detection considerations. Note that the above discussion does not take into account the effects of diffraction by the transmitting/receiving aperture.

2.2 Continuous-Wave Operation

In the case of CW operation, the laser emits coherent radiation continuously and so the scattering volume must be defined by the finite depth of focus of both the transmitter and the receiver. If the outgoing Gaussian beam has a waist of radius w_0, located at range R, then the irradiance along the optic axis with the distance z measured relative to the location of the waist is given by:

$$I(z) = I_0 \frac{w_0^2}{w(z)^2} \tag{2.26}$$

where I_0 is the axial irradiance in the plane of the waist, and since $w(z) = w_0[1+(z/z_R)^2]^{1/2}$, where z_R is called the Rayleigh Range ($z_R = \pi w_0^2/\lambda$), equation (2.26) may be rewritten as:

$$I(z) = \frac{I_0}{1+(z/z_R)^2} \tag{2.27}$$

Thus, when $z = z_R$, the on-axis irradiance falls to 50% of its peak value at $z = 0$. Because the irradiance decreases on either side of the waist, the power scattered by particles located far from the waist is reduced in comparison to those near the waist. In addition, since the receiver is designed to image the points near the waist onto the detector plane, object points located far from the waist will produce wavefronts with nonzero curvature in the plane of the detector. This phase front curvature, as discussed earlier, leads to inefficient mixing of the radiation scattered by these particles. Thus the longitudinal length of the scattering volume is generally accepted as $2z_R$, and the cross-sectional area can be approximated by πw_0^2. Therefore, the scattering volume may be approximated by the expression (see Figure 2.6):

$$v = 2\pi w_0^2 z_R \tag{2.28}$$

The power collected at the plane of the receiver may expressed as:

$$\overline{P}_r = \frac{2P_t\beta_\pi z_R A_r}{R^2}\cdot T^2 \tag{2.29}$$

where $T = \exp\{-\int \alpha(R')dR'\}$ is the one-way atmospheric transmittance evaluated from the lidar to the scattering volume, $\alpha(R')$ is the atmospheric extinction coefficient (m^{-1}), and β_π is the atmospheric backscattering coefficient ($m^{-1}sr^{-1}$).

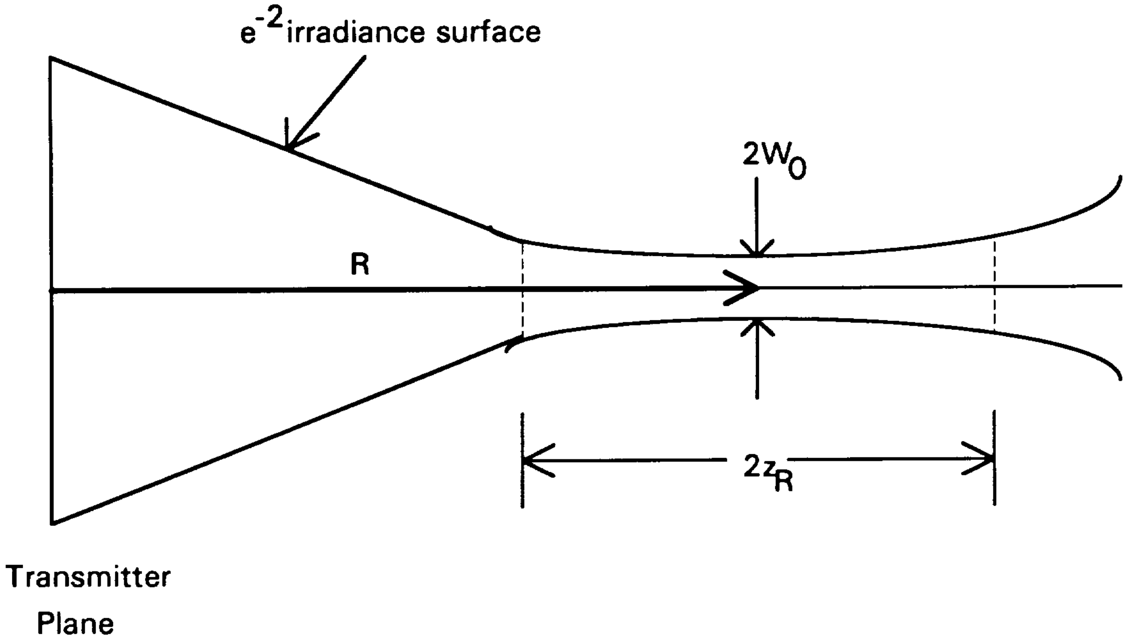

Figure 2.6. Parameters defining the scattering volume for continuous-wave operation

CHAPTER 3

OPTICAL DESIGN OF COHERENT LIDAR

As with most engineering problems, solutions involve practical constraints. Thus, due to fiscal constraints, certain components were not considered even though their inclusion in the lidar would have been preferred. All of the major optical components were prepurchased, which further limited the design considerations, although additional optical mounts were open to requisition. The optics inventory available for the optical design of the coherent lidar is summarized in Table 3.1.

TABLE 3.1

Optics Inventory for Coherent Lidar

COMPONENT DESCRIPTION	MIN. CLEAR APERTURE	COATING: Surface 1	Surface 2	RADIUS OF CURV.: Surface 1	Surface 2	CENTER THICKNESS
f/4 Paraboloid, 1/8 Wave	6"	Prot. Al	N/A	48"	N/A	N/A
ZnSe, Meniscus Lens, 0.75" efl	10.16 mm	AR	AR	16.600 mm	41.500 mm	1.820 mm
ZnSe, Meniscus Lens, 1.5" efl	15.240 mm	AR	AR	33.547 mm	85.400 mm	2.870 mm
ZnSe, Meniscus Lens, 2.0" efl	20.320 mm	AR	AR	44.250 mm	111.310 mm	3.150 mm
ZnSe, Plane Parallel Window	1"	AR	96%	Large	Large	3 mm
ZnSe, Plane Parallel Window	1"	AR	5%	"	"	3 mm
ZnSe, Plane Parallel Window	1"	AR	AR	"	"	3 mm
ZnSe, Brewster Window	39mm x 15m	Uncoated	Uncoated	"	"	3 mm
Wire Grid Polarizer (100:1)	25 mm	AR	AR	"	"	5 mm
CdS, Half-Wave Plate (9.4 mic.)	0.7"	AR	AR	"	"	5 mm
CdS, Quarter-Wave Plate (9.4 mic.)	0.7"	AR	AR	"	"	5 mm
Elliptical Mirror, 1/8 Wave	1.502"x1.062"	Prot. Gold	N/A	"	"	N/A
Si, CO2 Laser Mirror, 1/2 Wave	1.0"	Enh. Ag	N/A	"	"	N/A

3.1 Transmitter Considerations

3.1.1 Maximum Range

In order to reduce the associated cost and complexity of the laser source and the associated electronics, the coherent lidar described here was to be operated CW. Thus, the range and the scattering volume would be determined by focusing of the transmitted beam. Since this system was developed for remote sensing work, the maximum focal range needed to be as large as possible. According to Self (1983), a lens will transform a waist of radius w_0 located a distance z from the lens to a waist w_0' located at a distance z' (Self uses s and s', respectively) from the lens by the relation (see Figure 3.1):

$$[z'/f] = 1 + \frac{(z/f)-1}{[(z/f)-1]^2 + (z_R/f)^2} \tag{3.1}$$

The relationship between the input spot size and the output spot size is given by:

$$w_0' = mw_0 \text{ with } m = \frac{1}{\left\{[1-(z/f)]^2 + (z_R/f)^2\right\}^{1/2}} \tag{3.2}$$

and the relation between the input and output Rayleigh range is given by:

$$z_R' = m^2 z_R \tag{3.3}$$

where m is defined in (3.2). Self shows that the ratio of the Rayleigh range to the focal length of the lens determines the characteristics of the transformed spherical Gaussian beam. In the limit that the ratio z_R/f approaches 0, the spherical Gaussian beam can be treated as a uniform spherical wave; thus, the usual behavior predicted by geometrical optics can be applied. He also demonstrates that only a true geometrical beam can be imaged at infinity; thus, the smaller the z_R/f ratio, the further the waist can be located from the lens.

Figure 3.1

(z'/f) vs. (z/f)

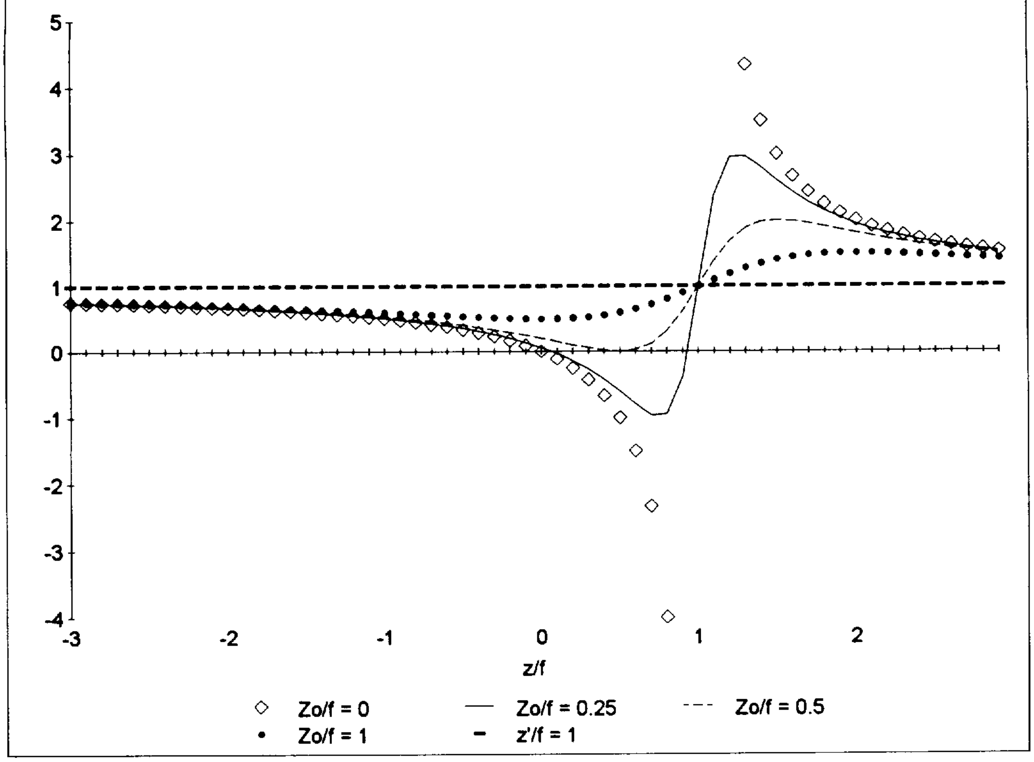

Therefore, in order to image the initial Gaussian beam produced by the laser at a long range, either the Rayleigh range can be minimized before reaching the transmitting optic and/or the focal length of the transmitter must be maximized. Due to the need to make the lidar as portable, *i.e.*, as small as possible, a very long focal length would not be appropriate. Thus, the obvious choice is to minimize the Rayleigh range. Since the Rayleigh range is proportional to the square of the spot size:

$$z_R = \frac{\pi w_0^2}{\lambda} \tag{3.4}$$

the spot size prior to transformation by the transmitter must be minimized.

The physical rationale behind the relationship between the ratio of z_R/f and the characteristics of the transformed beam can be explained on the basis of the curvature of the wavefronts of a Gaussian beam along the beam axis. The radius of curvature varies with distance z measured along the axis and can be written as:

$$R(z) = z\left\{1 + [z_R / z]^2\right\} \tag{3.5}$$

where $z = 0$ at the beam waist. From this expression, it should be noted that for $z >> z_R$ the radius of curvature is approximately equal to z and thus behaves like a geometric spherical wave. From a perusal of Figure 3.1, note that a Gaussian beam differs most markedly from a geometric beam when the beam waist is located near the front focal plane of the lens. Thus, when the waist is located near the front focal plane and the Rayleigh range is small in comparison to the focal length, then the lens will be located a distance z from the waist where $z >> z_R$, and the phase fronts incident on the lens will be spherical.

The characteristics of the Gaussian beam emerging from the laser are as shown in Table 3.2:

	TABLE 3.2. CO2 LASER SPECIFICATIONS.			
Wavelength:	Spot Size:	Rayleigh Range:	Divergence:	CW Power:
9.3 microns	1.5 mm	76 cm	2.0 mrad	7 Watts

where θ_0 is called the divergence angle (see Figure 2.1) and is given by:

$$\theta_0 = \frac{\lambda}{\pi w_0} \tag{3.6}$$

The spot size and radius of curvature as a function of z are given in Table 3.2, where use has been made of the relation:

$$w = w_0\left[1+(z/z_R)^2\right]^{1/2} \tag{3.7}$$

The last column in Table 3.3 gives the minimum aperture diameter required, which according to Siegman (1986) will transmit over 99.9% of the incident radiation with near field and far field irradiance ripples with variation ($\Delta I/I$) less than 1%. The necessary aperture diameter to satisfy this condition is given by:

$$D = 4.6w \tag{3.8}$$

where w is the spot size in the plane of the aperture. The optical table chosen for the lidar measured 2' x 3' (60.96 cm × 91.44 cm), and thus the longest distance from laser to beam expander would be less than 150 cm. Thus, the largest clear aperture required would be 1.5 cm.

As was discussed earlier, the initial waist, which is located at the output coupler of the CO_2 laser (since the coupler is a flat), must be transformed by a lens into as small a spot as possible in order for the secondary waist to be transformed once again into a waist at a remote location. Assuming, as in the case of ray optics, that a small magnification can be obtained by a short focal length lens, then it can be shown that in the case of $z >> f$, equation (3.2) may be rewritten as:

$$w = mw_0 \text{ where } m = \frac{f}{\left[z^2 + z_R^2\right]^{1/2}} \tag{3.9}$$

TABLE 3.3

Spot Size and Radius of Curvature

as a Function of z

z (cm)	w (mm)	R (cm)	Aperture Diameter (mm)
0	1.50	Infinite	6.9
5	1.50	1160	6.9
10	1.51	588	7.0
15	1.53	400	7.0
20	1.55	309	7.1
25	1.58	256	7.3
30	1.61	223	7.4
35	1.65	200	7.6
40	1.70	184	7.8
45	1.74	173	8.0
50	1.80	166	8.3
55	1.85	160	8.5
60	1.91	156	8.8
65	1.97	154	9.1
70	2.04	153	9.4
75	2.11	152	9.7
80	2.18	152	10.0
85	2.25	153	10.4
90	2.32	154	10.7
95	2.40	156	11.0
100	2.48	158	11.4
105	2.56	160	11.8
110	2.64	163	12.1
115	2.72	165	12.5
120	2.80	168	12.9
125	2.89	171	13.3
130	2.97	174	13.7
135	3.06	178	14.1
140	3.14	181	14.5
145	3.23	185	14.9
150	3.32	189	15.3
1000	19.79	1006	91.1

and thus the spot size varies directly with the focal length. Since, according to (3.6), the beam divergence is inversely proportional to the spot size, the beam will expand rapidly after being transformed by the expansion lens and must be properly sized to keep from overfilling and thus losing some of the incident power.

3.1.2 Maximum Power Transmission

The collimating mirror (following the expansion lens), *i.e.*, the transmitter, was a 6", *f*/4 paraboloid reflector. This was the shortest focal length paraboloid available as an off-the-shelf component which would fit within the project budget. Since the FOV of both transmitter and receiver, as discussed previously, will be very small (< 14 arcsec), the most significant third order aberration would be spherical; thus, a paraboloid is necessary to correct for this, since $W_{040} = 0$ in this case. The combination of expansion lens and collimating mirror form what is typically referred to as a beam expander. When the separation between these two elements is equal to the sum of their respective focal lengths, an afocal telescope results. A Newtonian telescope arrangement was determined to be the simplest beam expander as shown below (see Figure 3.2).

As is obvious from the above drawing, the outgoing beam will be apertured by both the paraboloid and the diagonal mirror. As was stated earlier, the waist formed by the expansion lens needs to have as small a spot size as possible, in order that the waist formed by the collimating lens be located as far away as possible from the lidar. As much of the paraboloid as possible should be used without losing too much power; however, if the spot size at the paraboloid is reduced too far, most of the power in the outgoing beam will be lost because of the central obscuration. Since the irradiance in a given transverse plane located a distance z from the waist at some radial distance ρ from the beam axis is given by:

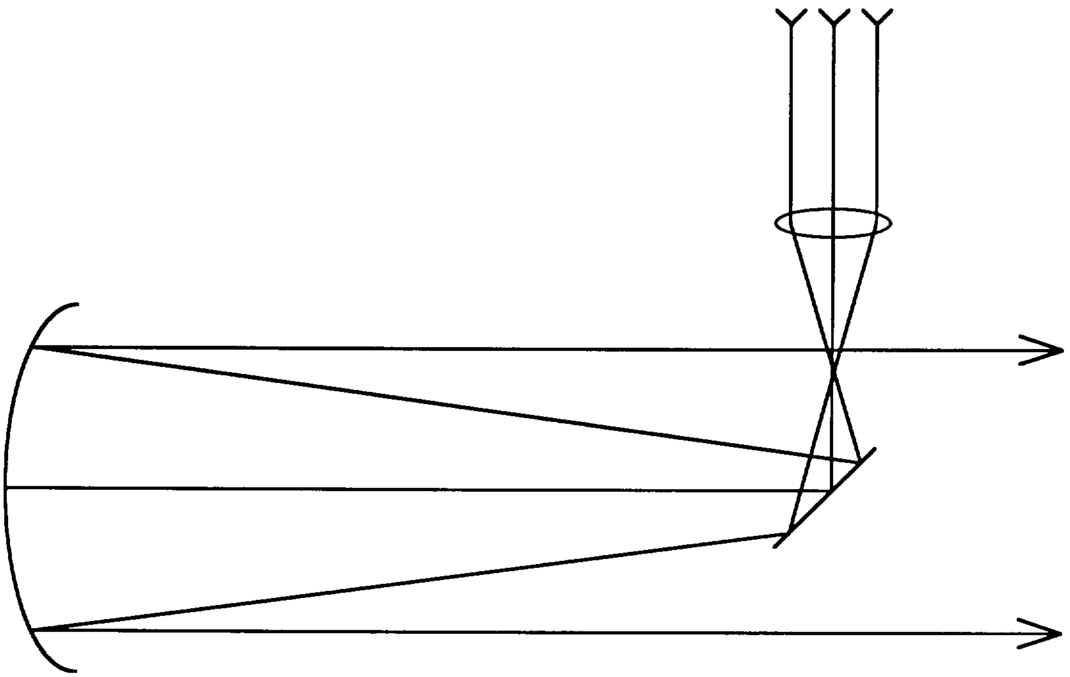

Figure 3.2. Beam Expander

$$I(\rho,z) = I_0\left\{\frac{w_0}{w(z)}\right\}^2 \exp\left\{\frac{-2\rho^2}{w^2(z)}\right\} \tag{3.10}$$

and the total power which is transmitted through an aperture of radius a at some location z along the beam axis is given by the expression:

$$P_{\text{transmitted}} = \int_0^a 2\pi\rho I(\rho)d\rho \tag{3.11}$$

which when evaluated becomes:

$$P_{\text{transmitted}} = \tfrac{1}{2} I_0 \pi w_0^2 \left\{1 - \exp\left[\frac{-2a^2}{w^2(z)}\right]\right\} \tag{3.12}$$

Since $P_{\text{total}} = I_0\pi(w_0^2/2)$, an expression for the percentage of power transmitted through an aperture of radius a may be written as:

$$\%P_{\text{transmitted}} = 1-\exp\left\{\frac{-2a^2}{w^2(z)}\right\} \quad \textbf{(3.13)}$$

(Siegman, 1986).

The problem then is to determine the correct spot size of the beam at the parabolic reflector, knowing that it has a fixed radius of r_2 and that the diagonal mirror has a fixed radius of r_1, as shown in Figure 3.3. Equation (3.13) will give the percentage of power lost due to the paraboloid, and so (3.13) must be subtracted from one to give the percentage of power transmitted around the obscuration. Once the two expressions for the power transmitted by each aperture are determined, the two can be multiplied to give the percentage of power transmitted by the beam expander:

$$\%P_{\text{transmitted}} = \left[1-\exp\left\{-2\left[\frac{r_2}{w}\right]^2\right\}\right]\exp\left\{-2\left[\frac{r_1}{w}\right]^2\right\} \quad \textbf{(3.14)}$$

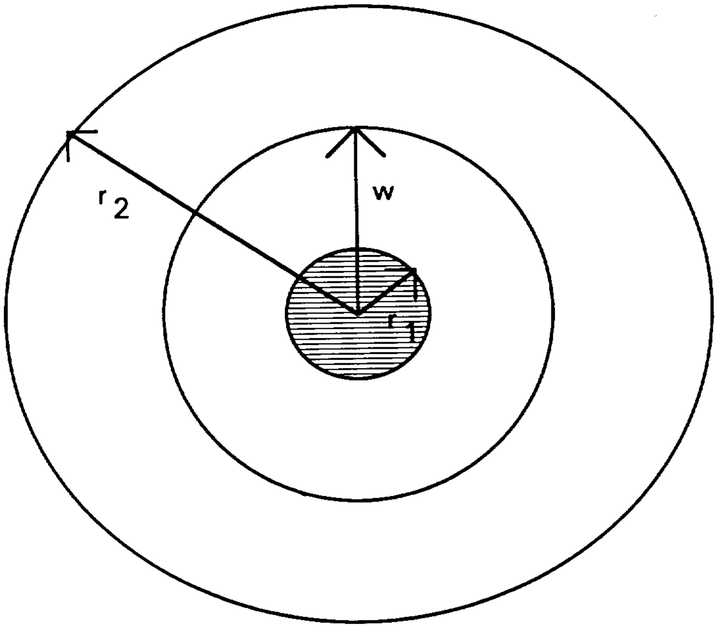

Figure 3.3. Parameters for calculation of maximum power transmission through beam expander

Since the elliptical diagonal mirror has a circular projection in a plane perpendicular to the propagation direction of the outgoing beam, it has a projected radius of 0.5", and the paraboloid has a fixed radius of 3". Equation (3.14) can be plotted as a function of spot size (see Figure 3.4).

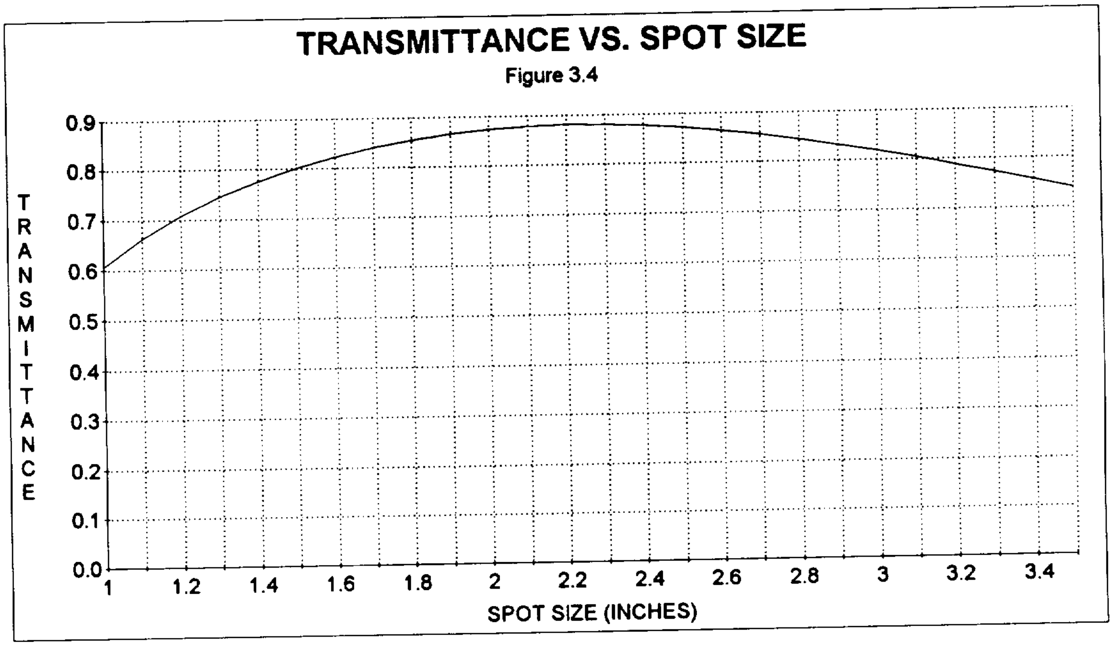
TRANSMITTANCE VS. SPOT SIZE

Figure 3.4

From the above graph, note that a maximum transmittance of almost 90% can be obtained for a spot size of about 2.2 inches. Holmes *et al.* (1972) demonstrate that for the above obscuration ratio ($r_1/r_2 \cong 0.2$), only minor changes in the shape of the focal plane encircled energy will be found with a 10% shift of the energy into the tails of the Gaussian irradiance profile. This spot size for maximum transmittance and the focal length of the paraboloid may be used to determine the proper focal length for the expansion lens.

Using equation (3.9), the magnification and thus the spot sizes at the waist transformed by the expansion lens using the three different focal length lenses available are found to be:

$f = 0.75''$, $w_0 = 21\ \mu\text{m}$, $z_R = 150\ \mu\text{m}$
$f = 1.5''$, $w_0 = 43\ \mu\text{m}$, $z_R = 625\ \mu\text{m}$
$f = 2.0''$, $w_0 = 57\ \mu\text{m}$, $z_R = 1100\ \mu\text{m}$

where the object distance, z, was chosen to be 115 cm, based on a preliminary layout of the laser and paraboloid. Initially, the beam expander was designed to focus the waist at maximum range. In order to determine what the distance, z, should be to maximize the distance, z', a derivative of (3.1) must first be taken:

$$\frac{d[z'/f]}{d[z/f]} = \frac{[(z/f)-1]^2 + (z_R/f)^2 - 2[(z/f)-1]^2}{\left\{[(z/f)-1]^2 + (z_R/f)^2\right\}^2} \tag{3.15}$$

which after setting equal to zero, the extremum is:

$$[(z/f)-1]^2 = [z_R/f]^2 \tag{3.16}$$

and solving for z results in:

$$z = f \pm z_R \tag{3.17}$$

The plus sign gives the distance, z, for a real waist, and the minus sign gives the distance, z, for a virtual waist (see Figure 3.1). Using the following object distances to determine the best expansion lens:

$z = 60.98$ cm for $f = 0.75''$
$z = 61.02$ cm for $f = 1.5''$
$z = 61.07$ cm for $f = 2.0''$

in equation (3.7), the spot sizes at the paraboloid will be:

$$w\,(60.98) = 3.4'' \text{ for } f = 0.75''$$
$$w\,(61.02) = 1.7'' \text{ for } f = 1.5''$$
$$w\,(61.07) = 1.3'' \text{ for } f = 2.0''$$

After examining Figure 3.4, the 1.5" efl lens is the best choice.

3.1.3 Multi-Configuration Beam Expander

In order to determine the minimum separation between the expansion and collimating optical elements, the following derivation was necessary. The minimum separation will focus the transmitted waist at maximum range, *i.e.*, will produce a nearly collimated beam. By increasing this separation, the waist can be focused at various finite distances from the transmitting paraboloid. The geometry for the following derivation is shown in Figure 3.5.

As was discussed previously, it may be assumed that $z_1 >> f_1$, and thus (3.1) simplifies to:

$$z_1' \cong f_1 \qquad \textbf{(3.18)}$$

and equation (3.17) may be used to write:

$$z_2' = f_2 + z_R' \qquad \textbf{(3.19)}$$

where $z_R' = m^2 z_R$. Upon squaring (3.9), the separation distance d can be expressed as:

$$d = f_1 + f_2 + \left[\frac{f_1^2}{z_1^2 + z_R^2}\right] z_R \qquad \textbf{(3.20)}$$

The following parameters can be substituted for the variables in (3.20):

$$f_1 = 3.81 \text{ cm},\quad f_2 = 60.96 \text{ cm},\quad z_1 = 115 \text{ cm},\quad z_R = 76 \text{ cm}$$

The required length for the afocal Newtonian telescope is approximately equal to:

$$d \cong 65 \text{ cm}$$

Table 3.4 summarizes the characteristics of the transmitted Gaussian beam. Figure 3.6 demonstrates the reason for the selection of the maximum focal range of 50 meters for actual use. As can be seen from this figure, the resolution, *i.e.*, the Rayleigh range, will be less than 10% of the focal range for ranges less than 50 meters, which was considered to be the upper limit on the resolution for precise experimental results. Table 3.5 summarizes the transmission characteristics of the beam expander, with the clear aperture dimensions of the diagonal mirror immediately after the expansion lens also contributing to additional losses in the transmitted power. Figure 3.7 shows a sketch of the transmitter portion of the lidar, where all distances are given in centimeters.

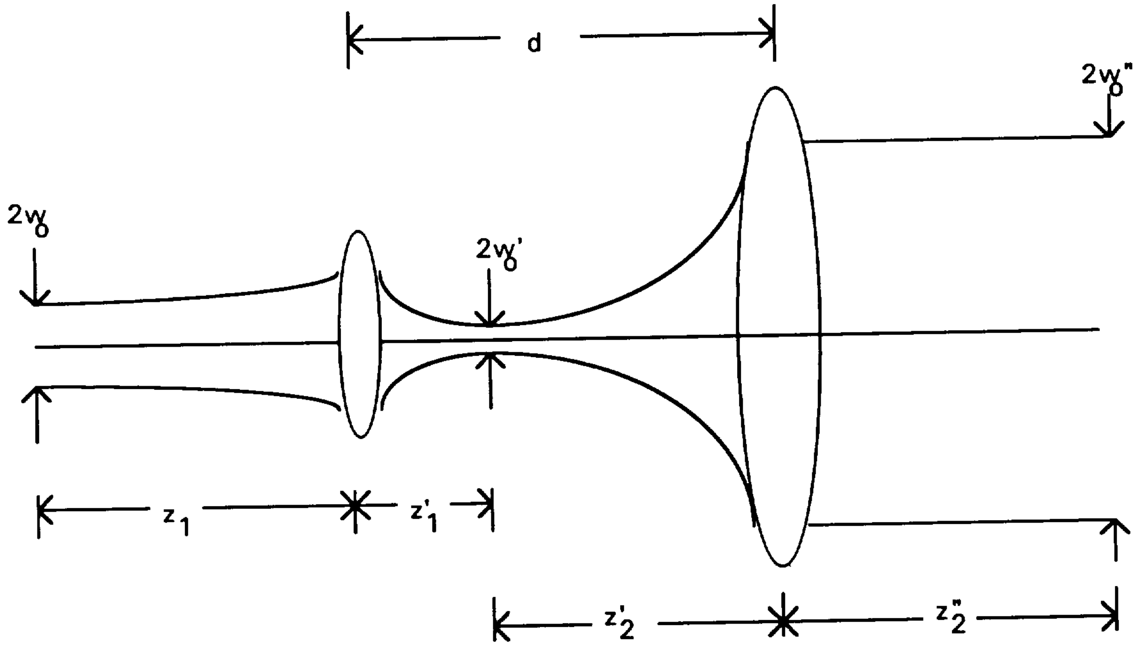

Figure 3.5. Gaussian beam parameters relative to transmitter components

FIGURE 3.6

RANGE RESOLUTION VS. RANGE

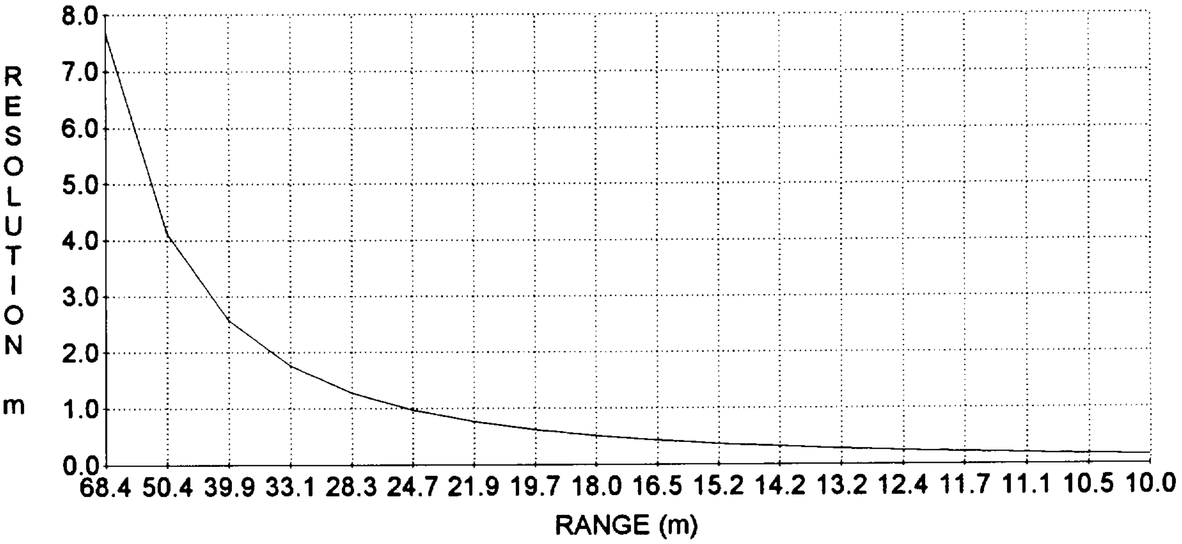

TABLE 3.4

GAUSSIAN BEAM PARAMETERS OF TRANSMITTER

Z1 (cm)	Z1' (cm)	Wo' (mm)	Zo' (cm)	d (cm)	Z2' (cm)	Z2" (cm)	Wo" (mm)	Zo" (cm)
114.9	3.90	4.25E-02	6.09E-02	65	61.1	2.23E+04	1.69E+01	9.59E+03
114.7	3.90	4.25E-02	6.10E-02	65.2	61.3	1.06E+04	7.48E+00	1.89E+03
114.5	3.90	4.26E-02	6.12E-02	65.4	61.5	6.84E+03	4.77E+00	7.68E+02
114.3	3.90	4.26E-02	6.13E-02	65.6	61.7	5.04E+03	3.49E+00	4.13E+02
114.1	3.90	4.27E-02	6.15E-02	65.8	61.9	3.99E+03	2.76E+00	2.57E+02
113.9	3.90	4.27E-02	6.17E-02	66	62.1	3.31E+03	2.28E+00	1.76E+02
113.7	3.90	4.28E-02	6.18E-02	66.2	62.3	2.83E+03	1.94E+00	1.28E+02
113.5	3.90	4.28E-02	6.20E-02	66.4	62.5	2.47E+03	1.69E+00	9.69E+01
113.3	3.90	4.29E-02	6.21E-02	66.6	62.7	2.19E+03	1.50E+00	7.61E+01
113.1	3.90	4.29E-02	6.23E-02	66.8	62.9	1.97E+03	1.35E+00	6.14E+01
112.9	3.90	4.30E-02	6.24E-02	67	63.1	1.80E+03	1.22E+00	5.06E+01
112.7	3.90	4.30E-02	6.26E-02	67.2	63.3	1.65E+03	1.12E+00	4.24E+01
112.5	3.90	4.31E-02	6.27E-02	67.4	63.5	1.52E+03	1.03E+00	3.61E+01
112.3	3.90	4.31E-02	6.29E-02	67.6	63.7	1.42E+03	9.60E-01	3.11E+01
112.1	3.90	4.32E-02	6.30E-02	67.8	63.9	1.32E+03	8.95E-01	2.71E+01
111.9	3.90	4.33E-02	6.32E-02	68	64.1	1.24E+03	8.39E-01	2.38E+01
111.7	3.90	4.33E-02	6.33E-02	68.2	64.3	1.17E+03	7.90E-01	2.11E+01
111.5	3.90	4.34E-02	6.35E-02	68.4	64.5	1.11E+03	7.47E-01	1.88E+01
111.3	3.90	4.34E-02	6.37E-02	68.6	64.7	1.05E+03	7.08E-01	1.69E+01
111.1	3.90	4.35E-02	6.38E-02	68.8	64.9	1.00E+03	6.72E-01	1.53E+01
110.9	3.90	4.35E-02	6.40E-02	69	65.1	9.58E+02	6.41E-01	1.39E+01
110.7	3.90	4.36E-02	6.41E-02	69.2	65.3	9.17E+02	6.12E-01	1.27E+01
110.5	3.90	4.36E-02	6.43E-02	69.4	65.5	8.79E+02	5.86E-01	1.16E+01
110.3	3.90	4.37E-02	6.45E-02	69.6	65.7	8.45E+02	5.62E-01	1.07E+01
110.1	3.90	4.37E-02	6.46E-02	69.8	65.9	8.13E+02	5.40E-01	9.84E+00
109.9	3.90	4.38E-02	6.48E-02	70	66.1	7.84E+02	5.19E-01	9.11E+00
109.7	3.90	4.38E-02	6.49E-02	70.2	66.3	7.57E+02	5.01E-01	8.46E+00
109.5	3.90	4.39E-02	6.51E-02	70.4	66.5	7.32E+02	4.83E-01	7.88E+00
109.3	3.90	4.40E-02	6.53E-02	70.6	66.7	7.08E+02	4.67E-01	7.36E+00
109.1	3.90	4.40E-02	6.54E-02	70.8	66.9	6.87E+02	4.52E-01	6.89E+00
108.9	3.90	4.41E-02	6.56E-02	71	67.1	6.66E+02	4.38E-01	6.47E+00
108.7	3.90	4.41E-02	6.58E-02	71.2	67.3	6.47E+02	4.24E-01	6.08E+00
108.5	3.90	4.42E-02	6.59E-02	71.4	67.5	6.29E+02	4.12E-01	5.73E+00
108.3	3.90	4.42E-02	6.61E-02	71.6	67.7	6.12E+02	4.00E-01	5.41E+00
108.1	3.90	4.43E-02	6.63E-02	71.8	67.9	5.96E+02	3.89E-01	5.11E+00
107.9	3.90	4.43E-02	6.64E-02	72	68.1	5.81E+02	3.79E-01	4.84E+00
107.7	3.90	4.44E-02	6.66E-02	72.2	68.3	5.67E+02	3.69E-01	4.59E+00
107.5	3.90	4.45E-02	6.68E-02	72.4	68.5	5.54E+02	3.59E-01	4.36E+00

TABLE 3.5

TRANSMITTANCE OF TRANSMITTER

d (cm)	Spot Size at Diagonal Mirror (in.	Transmittance of Diagonal Mirror	Spot Size at Paraboloid (in.)	Transmittance of Obscuration	Total Transmittance
65	0.261	99.9%	1.68	83.6%	83.5%
65.2	0.266	99.9%	1.68	83.6%	83.6%
65.4	0.271	99.9%	1.68	83.7%	83.6%
65.6	0.276	99.9%	1.69	83.7%	83.6%
65.8	0.281	99.8%	1.69	83.8%	83.6%
66	0.286	99.8%	1.69	83.9%	83.7%
66.2	0.292	99.7%	1.70	83.9%	83.7%
66.4	0.297	99.7%	1.70	84.0%	83.7%
66.6	0.302	99.6%	1.70	84.0%	83.7%
66.8	0.307	99.5%	1.71	84.1%	83.7%
67	0.312	99.4%	1.71	84.1%	83.6%
67.2	0.317	99.3%	1.71	84.2%	83.6%
67.4	0.322	99.2%	1.72	84.2%	83.5%
67.6	0.327	99.1%	1.72	84.3%	83.5%
67.8	0.332	98.9%	1.72	84.3%	83.4%
68	0.337	98.8%	1.73	84.4%	83.3%
68.2	0.342	98.6%	1.73	84.4%	83.2%
68.4	0.347	98.4%	1.73	84.5%	83.1%
68.6	0.352	98.2%	1.74	84.5%	83.0%
68.8	0.357	98.0%	1.74	84.6%	82.9%
69	0.362	97.8%	1.74	84.6%	82.8%
69.2	0.366	97.6%	1.75	84.6%	82.6%
69.4	0.371	97.3%	1.75	84.7%	82.4%
69.6	0.376	97.1%	1.75	84.7%	82.3%
69.8	0.381	96.8%	1.76	84.8%	82.1%
70	0.386	96.5%	1.76	84.8%	81.9%
70.2	0.391	96.2%	1.76	84.9%	81.7%
70.4	0.396	95.9%	1.77	84.9%	81.4%
70.6	0.400	95.6%	1.77	85.0%	81.2%
70.8	0.405	95.2%	1.77	85.0%	81.0%
71	0.410	94.9%	1.77	85.0%	80.7%
71.2	0.415	94.5%	1.78	85.1%	80.4%
71.4	0.419	94.2%	1.78	85.1%	80.2%
71.6	0.424	93.8%	1.78	85.2%	79.9%
71.8	0.429	93.4%	1.79	85.2%	79.6%
72	0.434	93.0%	1.79	85.2%	79.3%
72.2	0.438	92.6%	1.79	85.3%	79.0%
72.4	0.443	92.2%	1.80	85.3%	78.6%

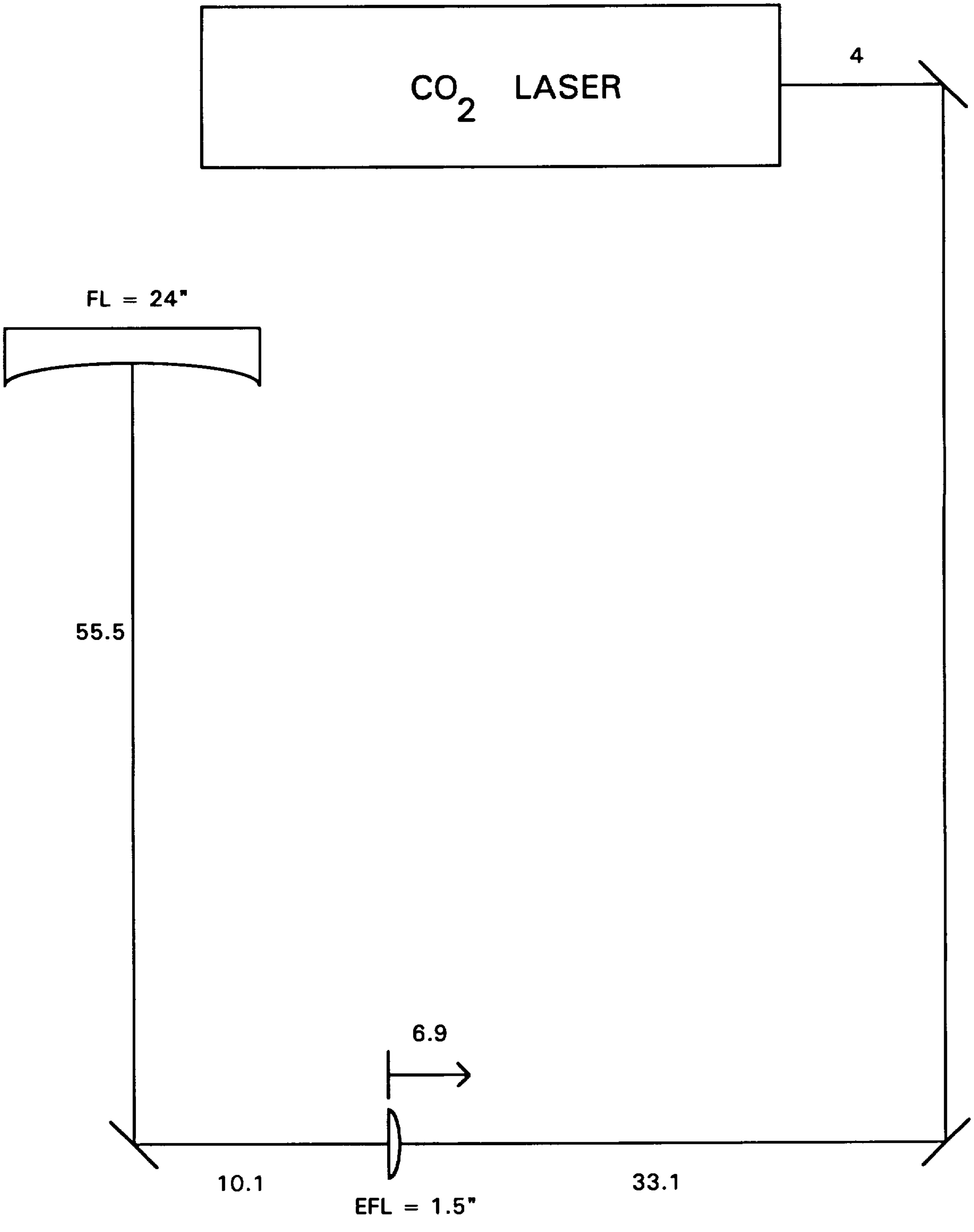

Figure 3.7. Layout of Transmitter (component separations in centimeters)

3.2 Local Oscillator Considerations

3.2.1 Detector DC Current Level

The local oscillator arm of the lidar can be thought of as the reference arm of a Twyman-Green Interferometer (see Figure 1.1). From equation (2.6), note that the backscattered power will contribute to the dc current; however, because it depends on the differential scattering cross-section (see equation 2.32), β_π, which is typically less than 10^{-6} $m^{-1}sr^{-1}$, its contribution will be negligible in comparison to that due to the local oscillator. As was stated previously, the local oscillator power is deliberately made to be much larger than the power backscattered by the aerosols, in order to increase the heterodyne gain of the system. Thus the dc current will be entirely dependent on the local oscillator power incident on the photodetector. The characteristics of the HgCdTe photovoltaic detector are as shown in Table 3.6:

TABLE 3.6

HgCdTe PHOTOVOLTAIC DETECTOR SPECIFICATIONS

	SMA-1:	SMA-2:
Element Size (mm)	0.25 x 0.25	0.2 x 0.2
Spectral Responsivity (A/W)	5.62	5.85
Cutoff Wavelength (microns)	10.67	10.68
Quantum Efficiency (%)	65	68
Maximum DC Current (mA)	1	1

Using the above specifications, the local oscillator path should transmit a maximum of 0.17 mW onto the photodetector. Using the windows listed in Table 3.1, the maximum power transmitted will be 0.14 mW by using one (1) 5% reflecting window, one (1) AR/AR (1% reflecting) window, and one (1) 4% transmitting window.

3.2.2 Optical Attenuator

In order to allow for possible changes in the output power of the laser (since it does not have stabilization electronics), an optical attenuator was used to further decrease the power by a factor of 100 or more. An optical attenuator consists of the combination of a Half-Wave Plate followed by a Wire Grid Polarizer, respectively. The thickness of the half-wave plate, *d*, is determined by the expression:

$$d(|n_0 - n_e|) = (2m + 1)\lambda/2 \qquad \textbf{(3.21)}$$

where m is the order of the wave plate. Equation (3.21) demonstrates that a half-wave plate is designed to introduce a relative phase difference of π radians or 180° between the ordinary and extraordinary waves. For a given angle ϕ between the fast axis of the half-wave plate and the E-field of the linearly polarized laser beam, the E-field will be rotated by 2ϕ (see Figure 3.8).

The wire grid polarizer behaves according to Malus' Law:

$$I = I_0 \cos^2 \theta \qquad \textbf{(3.22)}$$

where θ is the angle between the E-field of the incident beam and the transmission axis of the polarizer. Thus, if the transmission axis of the polarizer remains fixed (the correct orientation will be discussed in section 3.3), the transmittance of the polarizer can vary between 1 and 0 (experimentally between 0.85 and 0.01).

3.2.3 Gaussian Beam Spot Size

The local oscillator arm was determined to have a minimum length of 70 cm to a maximum length of 100 cm based on available space. The spot size of the Gaussian beam must be reduced in order that it have a magnitude at the detector

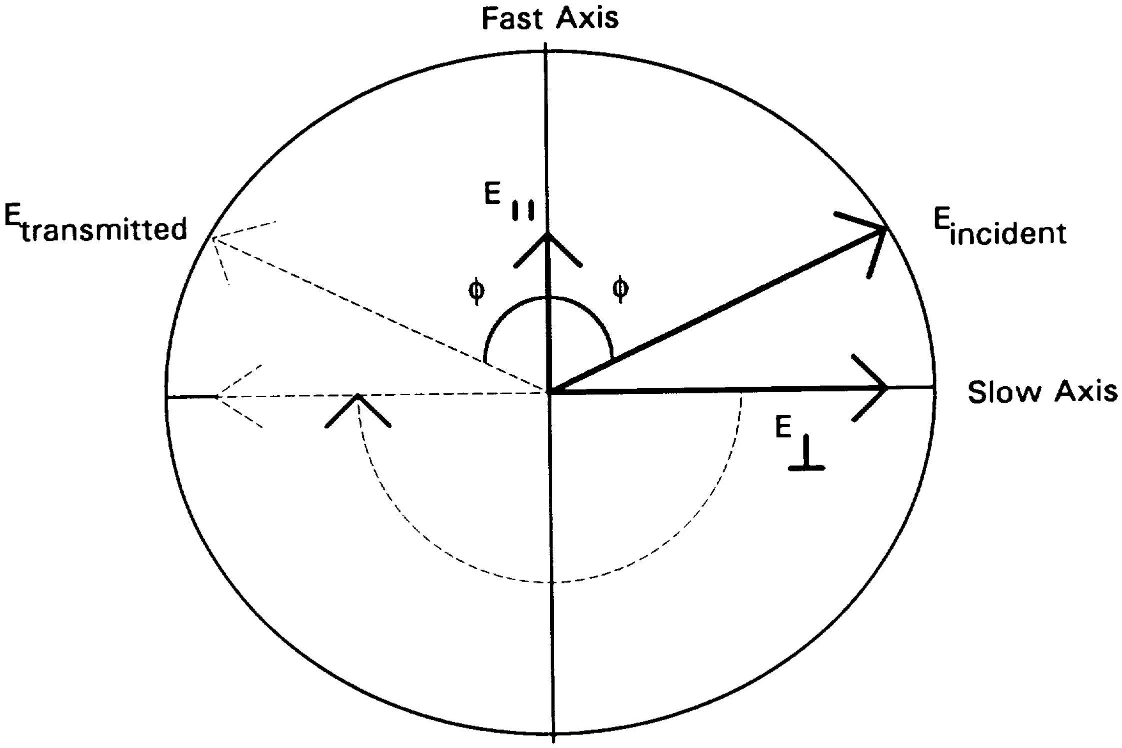

Figure 3.8. Properties of half-wave plate

plane which is smaller than 100 micrometers. Because of equation (3.18), the transformed waist will be located near the back focal plane of the chosen lens. Equation (3.9) may be used to determine the magnification and thus the spot size of the waist for the three different focal lengths available. Using 70 cm, since it will produce the largest spot size, the three possible spot sizes are as follows:

$$\text{for } f = 0.75'' \Rightarrow w_0 = 28\ \mu\text{m}$$
$$\text{for } f = 1.5'' \Rightarrow w_0 = 55\ \mu\text{m}$$
$$\text{for } f = 2.0'' \Rightarrow w_0 = 74\ \mu\text{m}$$

If the smaller of the two detector chips is used, then a correctly matched Gaussian local oscillator irradiance profile with an Airy function backscattered irradiance profile (which has an Airy disk radius of just under 100 micrometers) dictates that the Gaussian spot size should be less than 70 μm. Thus, a 1.5" efl lens was chosen, since it gives a spot size of less than 70 μm but illuminates more of the detector plane than the 0.75" efl lens and therefore will not produce as high an irradiance, which could damage the photodiode. The spot size and distance, *z'*, of the Gaussian beam are provided in Table 3.7 as a function of distance, *z*. The local oscillator arm is sketched in Figure 3.9.

TABLE 3.7
FOCUSING PROPERTIES OF
LOCAL OSCILLATOR

Z (cm)	Z' (cm)	Wo' (microns)
70	3.90	56.7
71	3.90	56.3
72	3.90	56.0
73	3.91	55.6
74	3.91	55.2
75	3.91	54.9
76	3.91	54.5
77	3.91	54.2
78	3.91	53.8
79	3.91	53.5
80	3.91	53.1
81	3.91	52.8
82	3.91	52.4
83	3.91	52.1
84	3.91	51.7
85	3.91	51.4
86	3.91	51.1
87	3.91	50.7
88	3.91	50.4
89	3.90	50.1
90	3.90	49.7
91	3.90	49.4
92	3.90	49.1
93	3.90	48.8
94	3.90	48.5
95	3.90	48.1
96	3.90	47.8
97	3.90	47.5
98	3.90	47.2
99	3.90	46.9
100	3.90	46.6

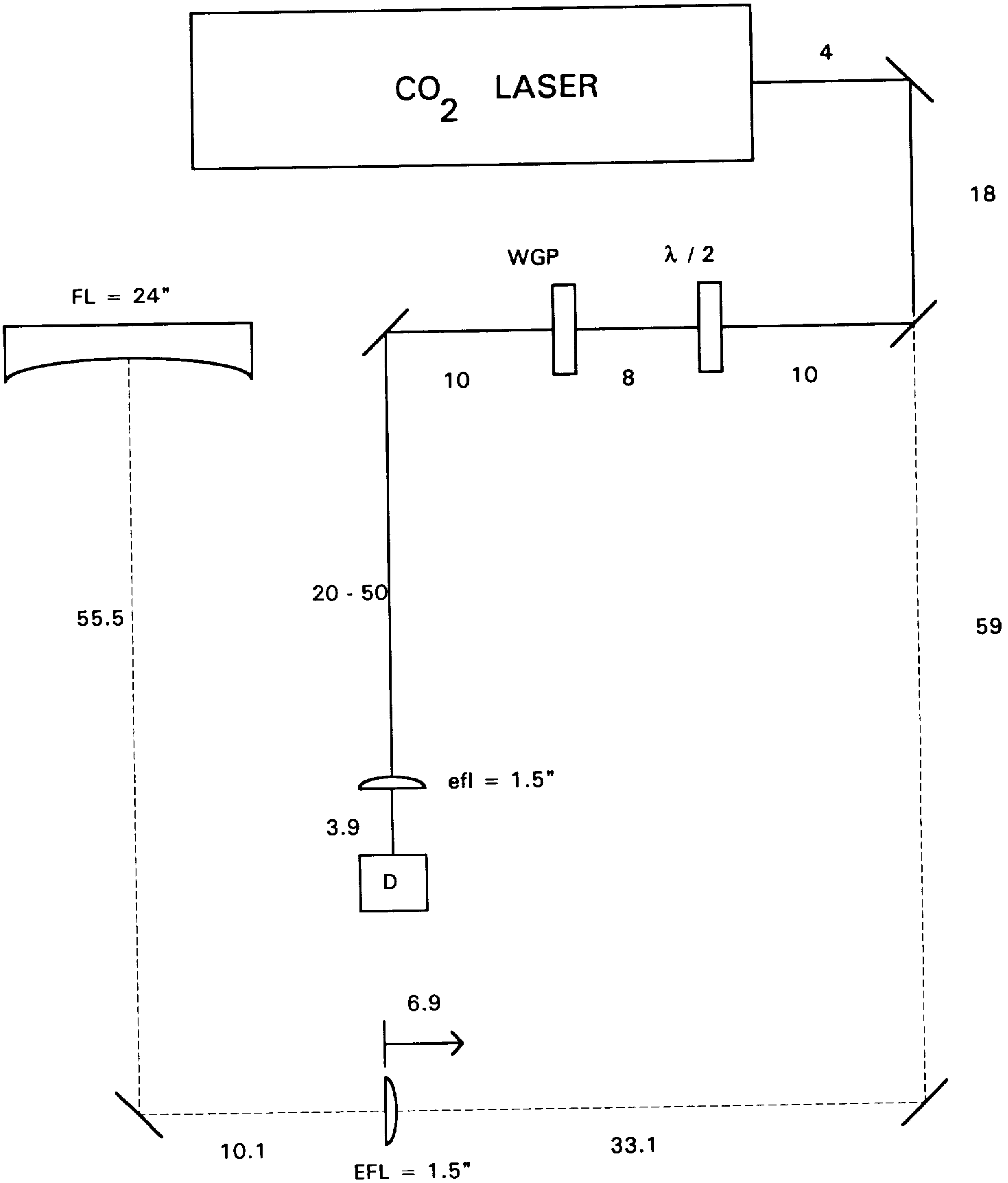

Figure 3.9. Layout of Local Oscillator (component separations in centimeters)

3.3 Receiver Considerations

As was stated earlier, the backscattered irradiance profile in the detector plane due to a single scatterer will be an Airy function. Thus, the system must be diffraction limited in order that the spot size at the detector plane may be determined by diffraction and not aberration. A sophisticated lens design program was used to model the receiver and determine the correct separation between the beam expander and detector lens for optimum diffraction limited performance.

Using equation (2.12) and noting that our laser operated at a wavelength of 9.3 micrometers, the semi-FOV is given by:

$$\theta_{\text{semi-FOV}} = 4.3 \times 10^{-3} \text{ Degrees} \tag{3.23}$$

and thus the aberrations were evaluated for an image point on-axis and for an image point at the edge of the field determined by the above angle. In addition, the receiver was optimized for the minimum focal range, 5.5 meters (see Figures 3.10-3.16), and maximum focal range, 50 meters (see Figures 3.17-3.23).

3.3.1 Short Range

For the range of 5.5 meters, note that because the Airy disk radius is about 72 microns (see Figure 3.10), the local oscillator spot size should be about 50 microns. This will give a ratio of Airy disk radius to Gaussian beam spot size of 1.4:1. The receiver is diffraction limited, as can be seen from the Intensity Point Spread Function (Figure 3.11), which shows the familiar Airy function. In addition, the OPD plots show that the maximum wave aberration across the pupil is less than

$\lambda/4$ (see Figure 3.13). The dominant aberration present is spherical aberration with defocus being used to minimize the peak-to-valley spot size (see Figure 3.14).

Due to the central obscuration within the beam expander, some of the energy normally found within the bright Airy disk has been diffracted into the outer rings. Figure 3.12 shows that the total energy within the Airy disk is about 80% for the 5.5-meter range, as compared to a perfect system without any obscuration which would contain 84% of the total energy within the Airy disk.

From Figure 3.15, note that the paraxial focus as a function of field height shows little longitudinal shift, *i.e.*, the field is quite flat with very little astigmatism, which is necessary for proper focusing onto a flat detector plane. Finally, with reference to Figure 3.16, it can be seen that not more than 5% of the rays traced through the receiver are vignetted, which prevents a loss of irradiance at the edges of the field.

3.3.2 Long Range

As the focal range is increased to 50 meters, the Airy disk radius decreases to 48 microns. Therefore, the correct spot size for the local oscillator is 34 microns, which, as can be seen from Table 3.5, is not possible for the local oscillator path lengths available. Thus, the two beams will be matched exactly, resulting in a fractional decrease in heterodyne efficiency of less than 20% (Zhao *et al.*, 1990*a,b*).

With reference to Figures 3.18 and 3.20, for the case of the long range configuration, the system remains diffraction limited. There is slightly less total energy in the Airy disk at about 78% (see Figure 3.19). Spherical aberration is again the dominant aberration, with defocus used to correct for it (see Figure 3.21). As before, the field is quite flat and unvignetted (see Figures 3.22 and 3.23).

3.3.3 Optical Switching

As shown in Figure 1.2, there is a beam splitter which separates the transmitter from the receiver. In actual practice, a combination of a quarter-wave plate and a plane parallel plate oriented at Brewster's angle is used to further increase the total signal power incident on the detector plane. From the Fresnel equations, the reflectance of a material such as ZnSe *vs.* angle of incidence may be plotted, as shown in Figure 3.24. At Brewster's angle, the *p*-polarized component of the electric field approaches a reflectance of 0% and a transmittance of nearly 100%, while the *s*-polarized component has a reflectance and transmittance of about 50% at Brewster's angle. Thus, if the linear polarization state can be rotated from *p*-polarized to *s*-polarized after passing through the plate oriented at Brewster's angle, then upon passing through the plate the second time, 50% of the energy will be reflected. The only way to rotate the plane of polarization as described above is, of course, to use a quarter-wave plate after the Brewster plate, where the ordinary and extraordinary rays see an optical path difference given by:

$$d(|n_0 - n_e|) = (2m+1)\lambda/4 \tag{3.24}$$

where d is the physical thickness of the quarter-wave plate and m is the order. After passing through the quarter-wave plate twice, the optical path difference is the same as that due to a half-wave plate as described in equation (3.21). Thus, for the fast axis of the quarter-wave oriented at 45 degrees with respect to the incident *p*-polarized radiation, after passing through it the second time, the plane of polarization will have rotated through twice the angle or 90 degrees.

Since the signal beam after reflection from the Brewster plate is *s*-polarized, the wire grid polarizer must also be oriented with its transmission axis vertical. This orientation ensures that the electric field vector of the local oscillator will be in a vertical plane, which allows the optical mixing discussed in section 2.1.1 to occur.

The relative placement of the Brewster plate and the quarter-wave plate, as well as the spacings between the optical elements for the maximum focal range of 50 meters down to the minimum range of 5.5 meters, respectively, is shown in Figure 3.25.

REFLECT. OF ZnSe V. ANGLE OF INCIDENCE

Figure 3.24

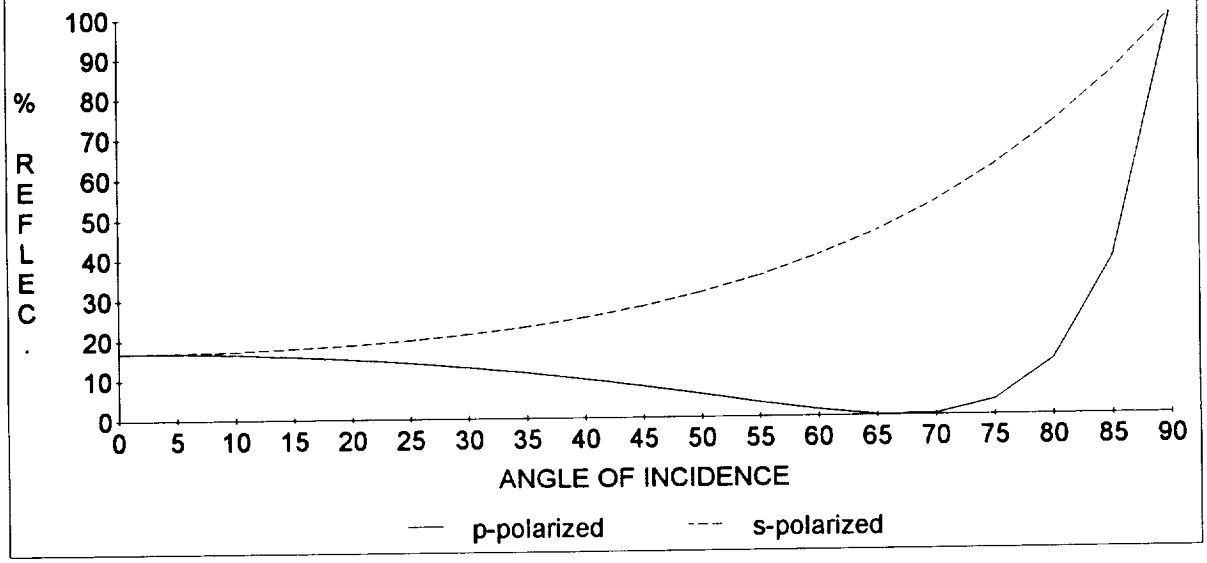

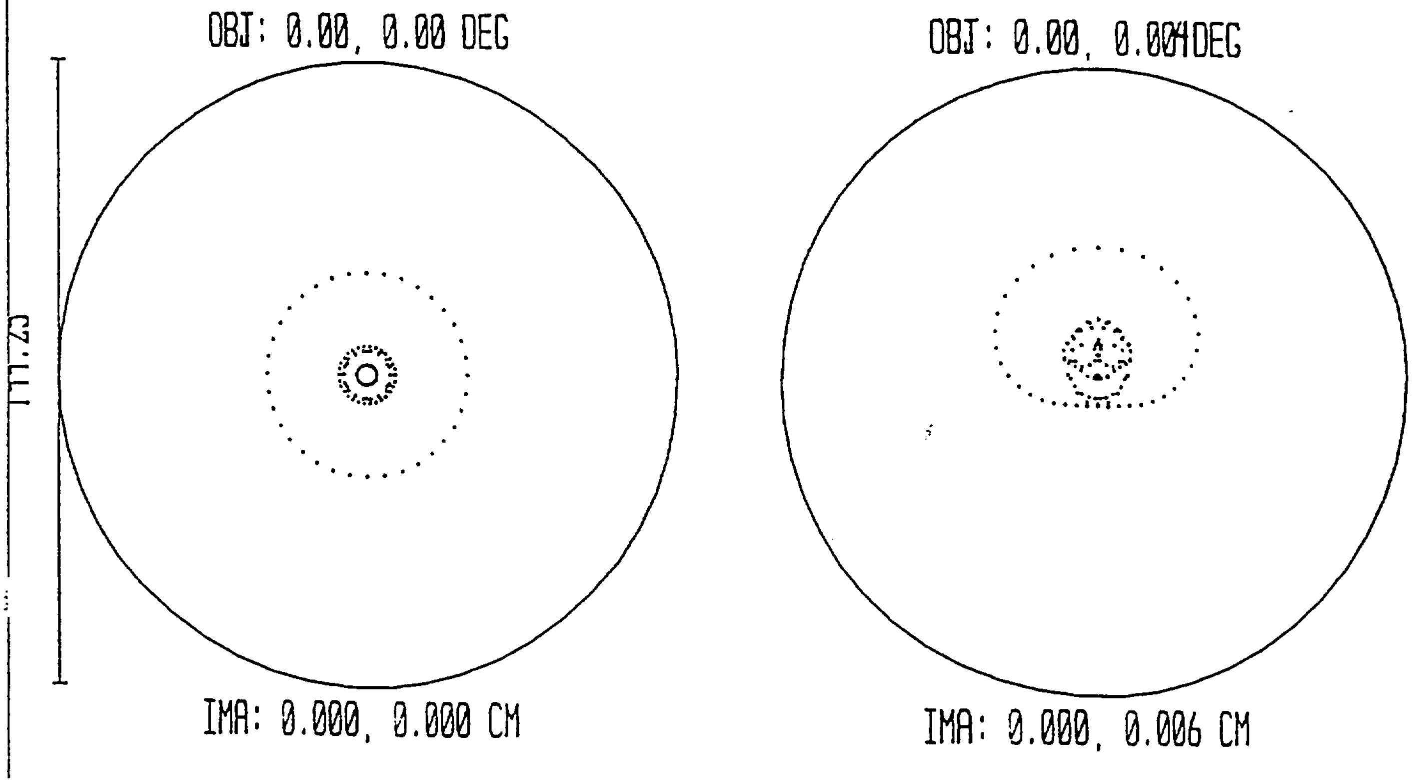

SPOT DIAGRAM

24 EFL PRIMARY, FOCAL DISTANCE = 5.5 METERS
SAT MAR 13 1993 UNITS ARE MICRONS.

FIELD	:	1	2
RMS RADIUS	:	13.61	14.06
GEO RADIUS	:	23.53	31.10
AIRY DISK	:	72.12	

REFERENCE : CHIEF RAY

BRET WHITESIDE

FIGURE 3.10

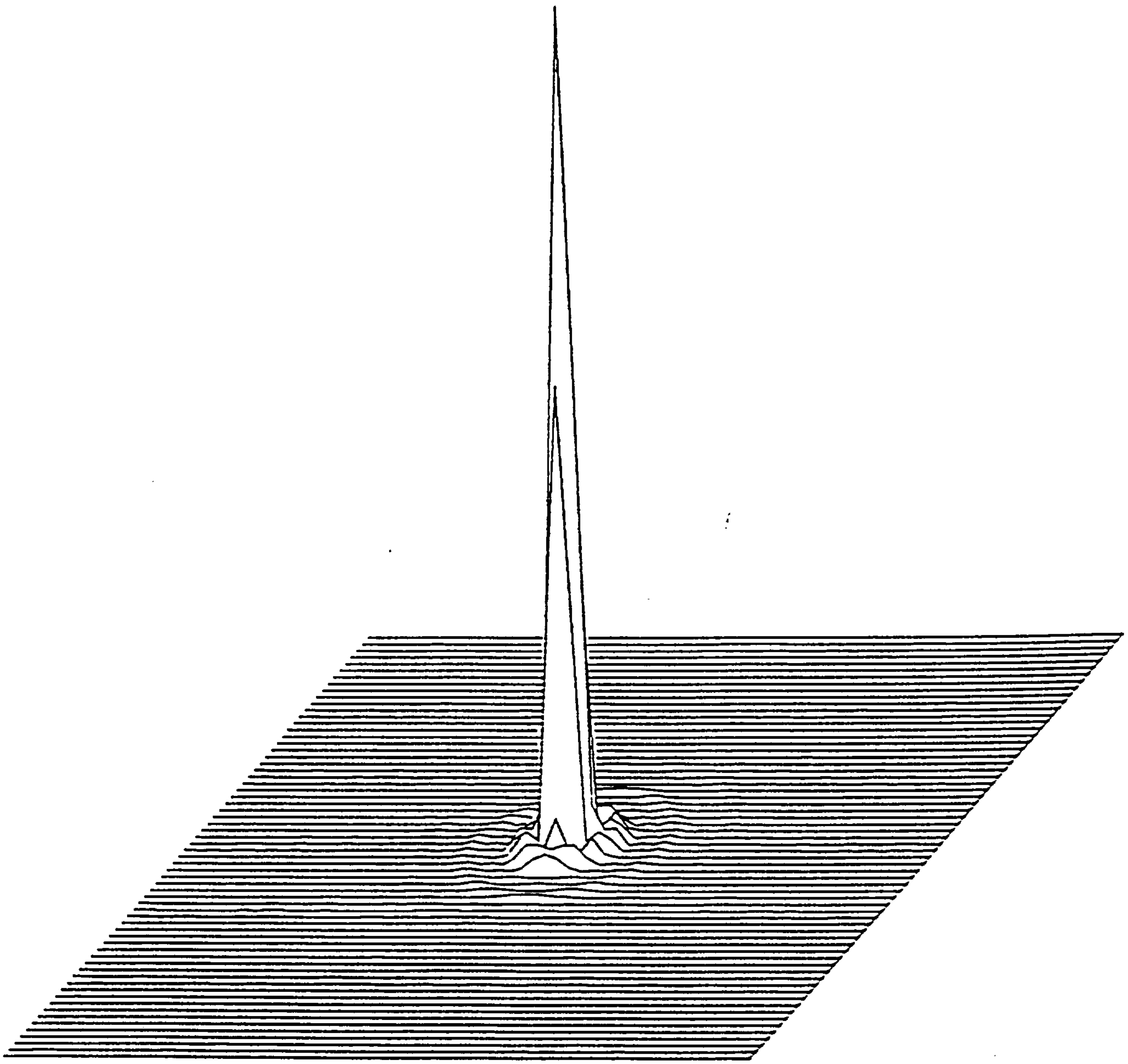

INTENSITY POINT SPREAD FUNCTION

24 EFL PRIMARY, FOCAL DISTANCE = 5.5 METERS
SAT MAR 13 1993
9.3000 MICRONS AT 0.00, 0.004 DEG.
SIDE IS 1891.75 MICRONS.

BRET WHITESIDE
FIGURE 3.11

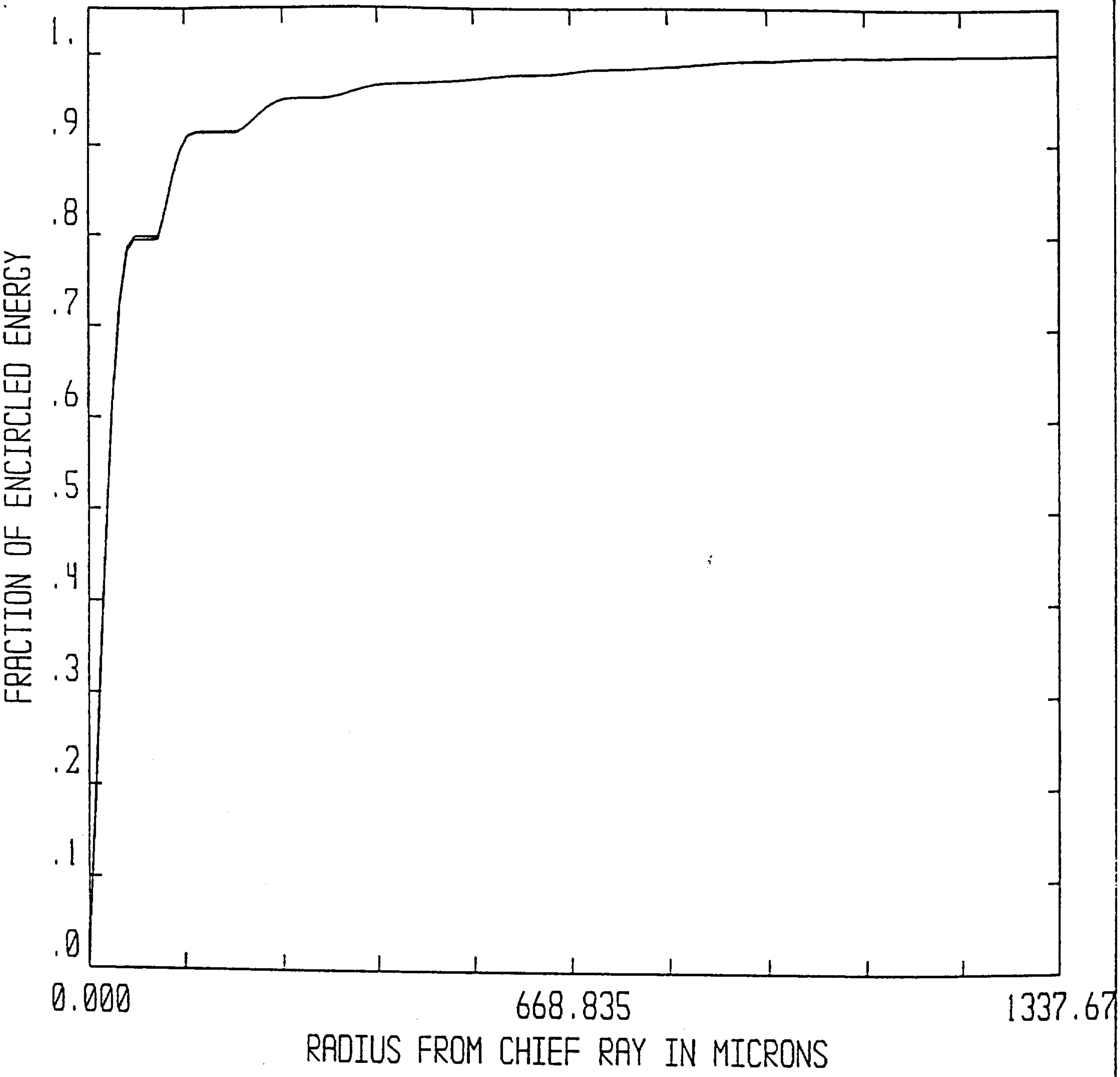

DIFFRACTION ENCIRCLED ENERGY

24 EFL PRIMARY, FOCAL DISTANCE = 5.5 METERS
SAT MAR 13 1993
FIELDS: 0.00, 0.00 DEG 0.00, 0.00 DEG

BRET WHITESIDE
FIGURE 3.12

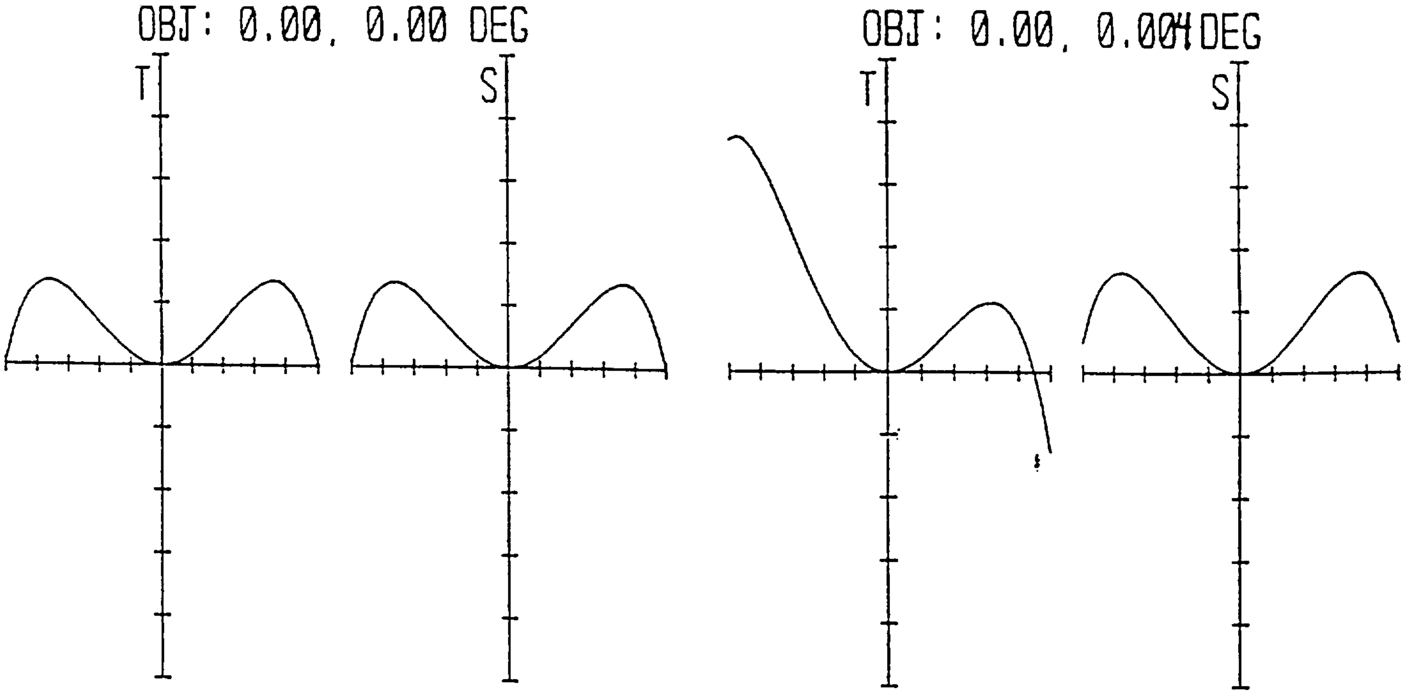

OPTICAL PATH DIFFERENCE

24 EFL PRIMARY, FOCAL DISTANCE = 5.5 METERS
SAT MAR 13 1993
MAXIMUM SCALE: -0.1000 TO 0.1000 WAVES.
9.300

BRET WHITESIDE
FIGURE 3.13

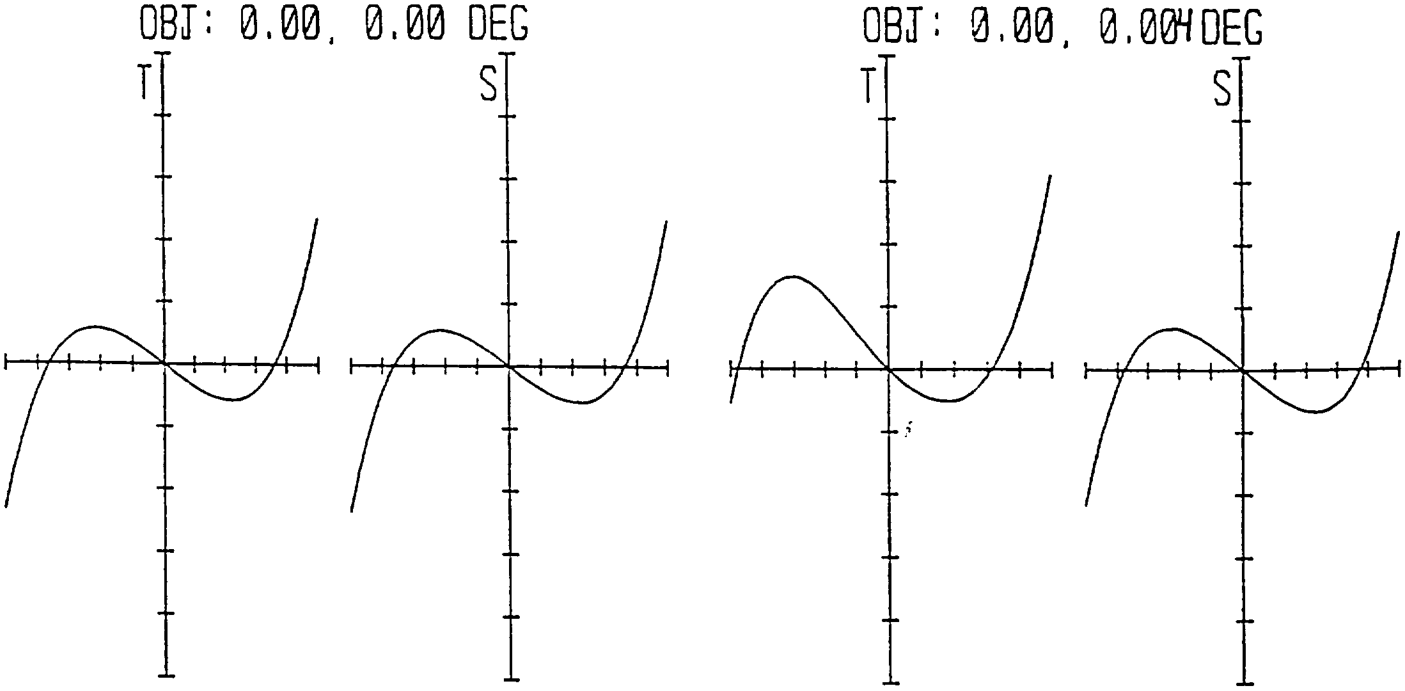

TRANSVERSE RAY FAN PLOT

24 EFL PRIMARY, FOCAL DISTANCE = 5.5 METERS
SAT MAR 13 1993
MAXIMUM SCALE: -50.0000 TO 50.0000 MICRONS.
9.300

BRET WHITESIDE
FIGURE 3.14

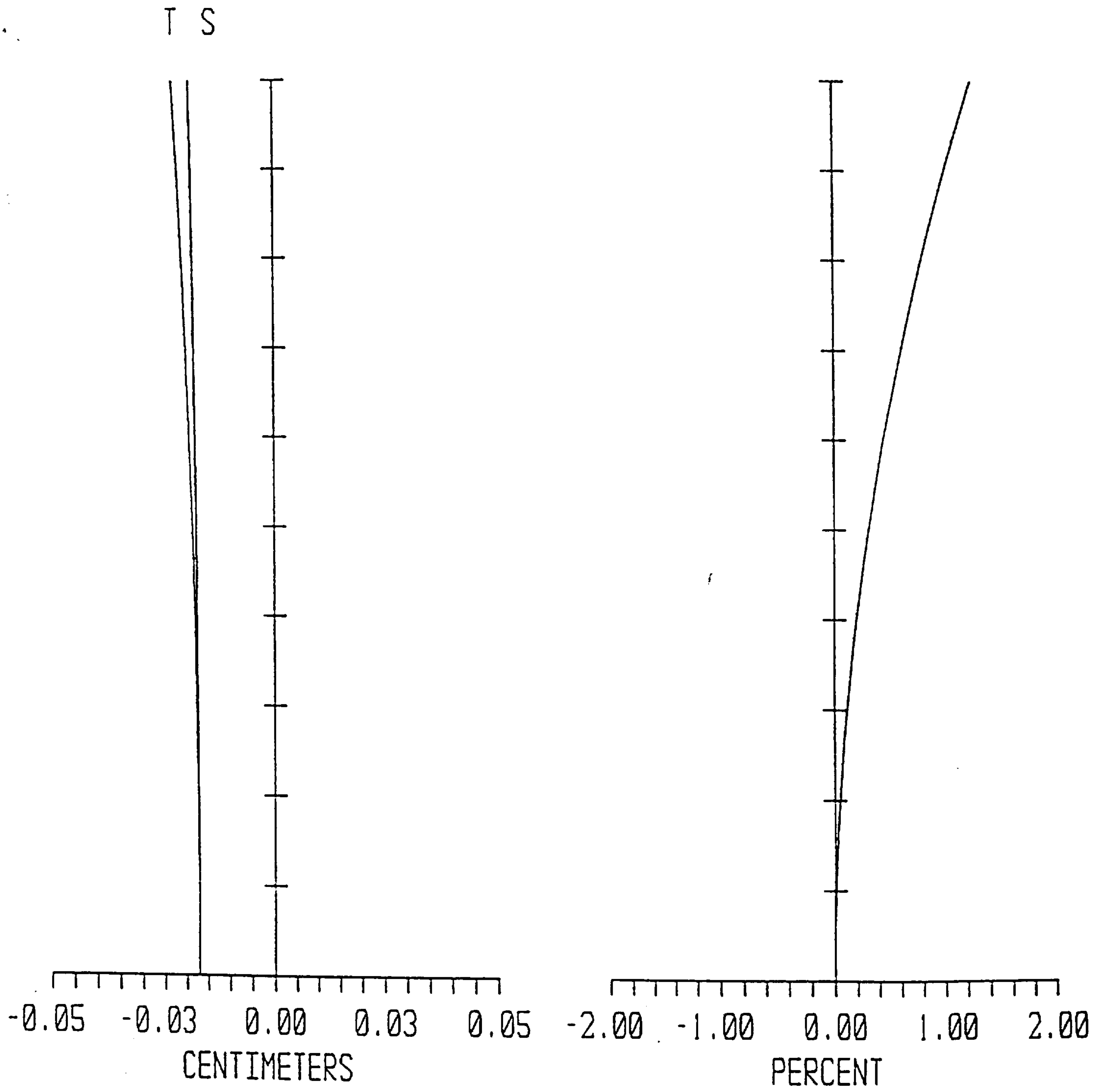

FIELD CURVATURE / DISTORTION

24 EFL PRIMARY, FOCAL DISTANCE = 5.5 METERS
SAT MAR 13 1993
MAXIMUM FIELD IS 0.004 DEGREES
WAVELENGTHS: 9.300

BRET WHITESIDE
FIGURE 3.15

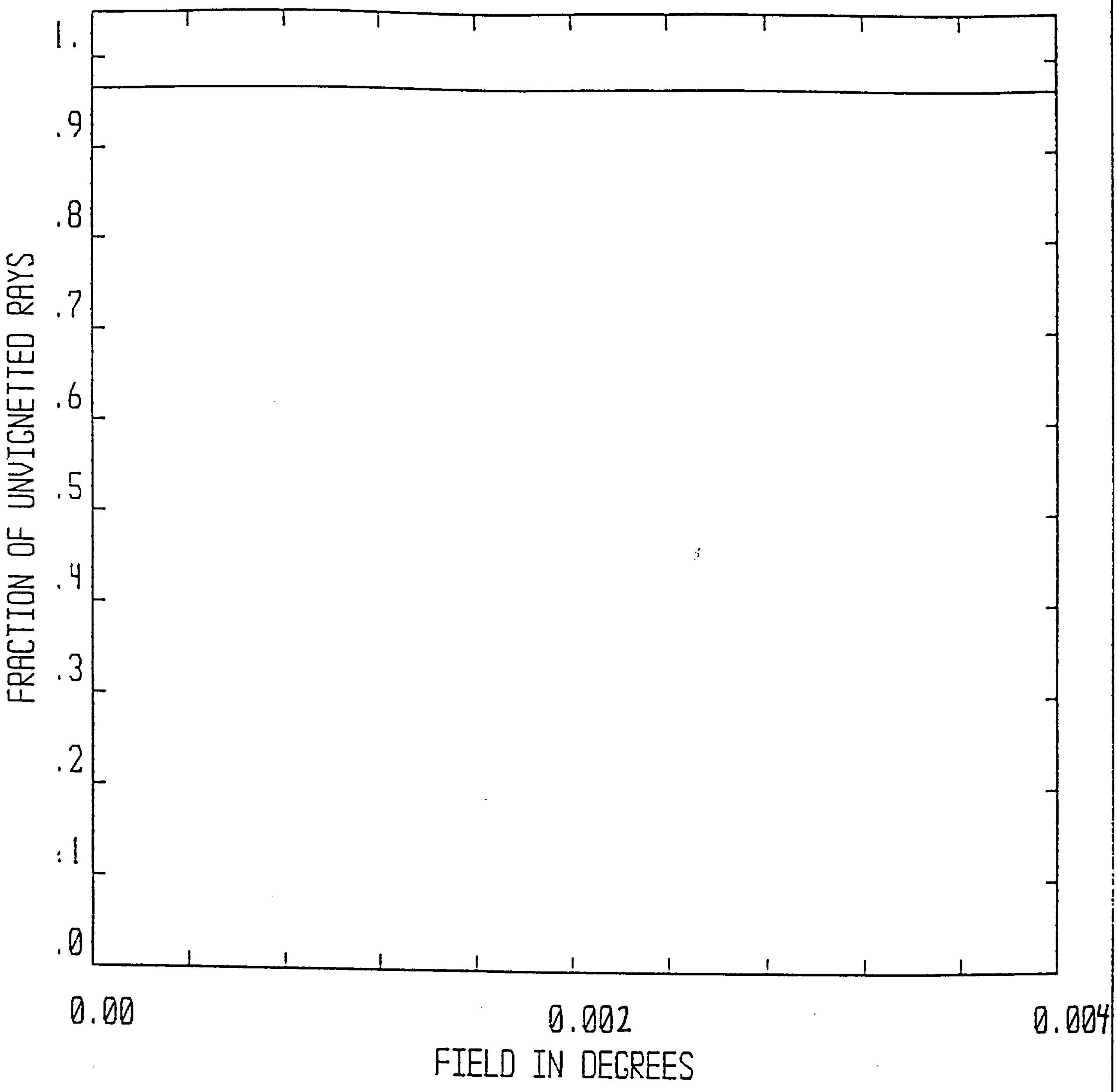

VIGNETTING DIAGRAM

24 EFL PRIMARY, FOCAL DISTANCE = 5.5 METERS
SAT MAR 13 1993

BRET WHITESIDE
FIGURE 3.16

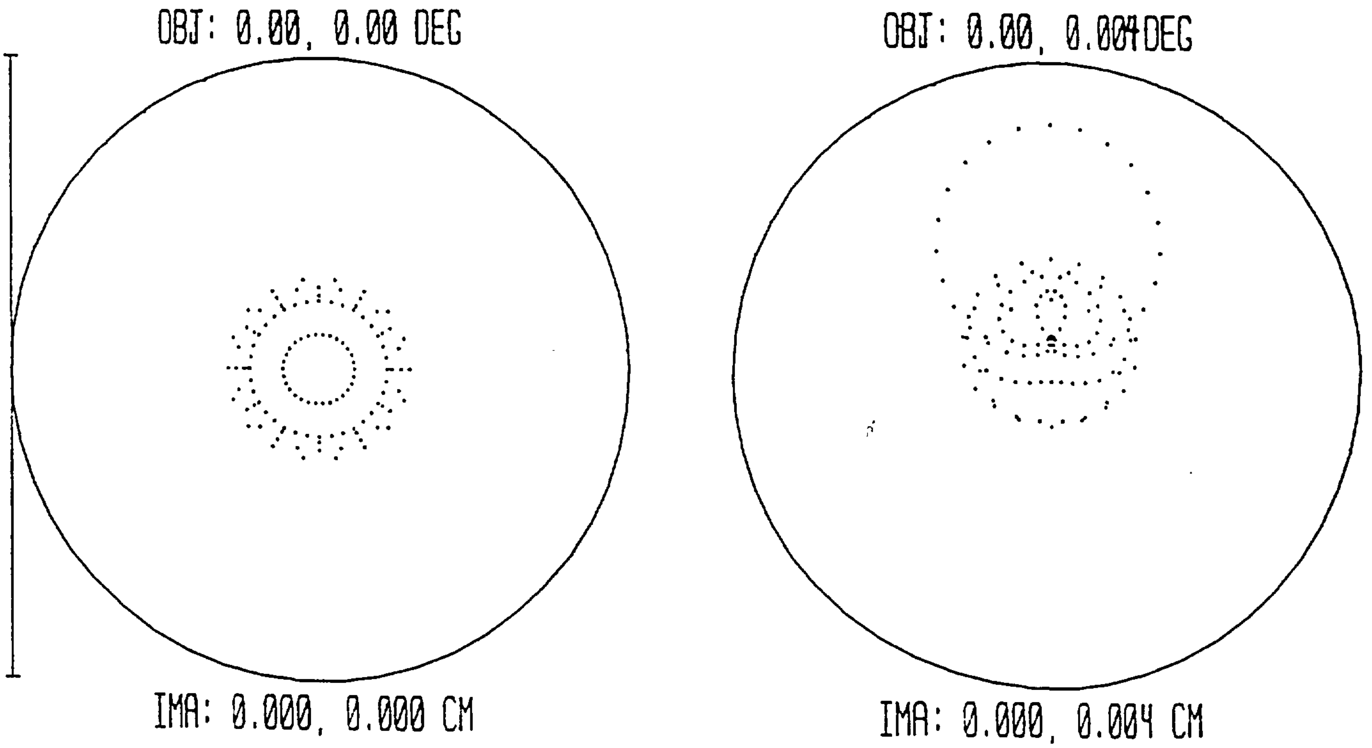

SPOT DIAGRAM

24 EFL PRIMARY, 50 METER FOCAL RANGE
SUN MAR 14 1993 UNITS ARE MICRONS.

FIELD	:	1	2
RMS RADIUS	:	10.80	15.66
GEO RADIUS	:	14.08	38.85
AIRY DISK	:	48.41	

REFERENCE : CHIEF RAY

BRET WHITESIDE

FIGURE 3.17

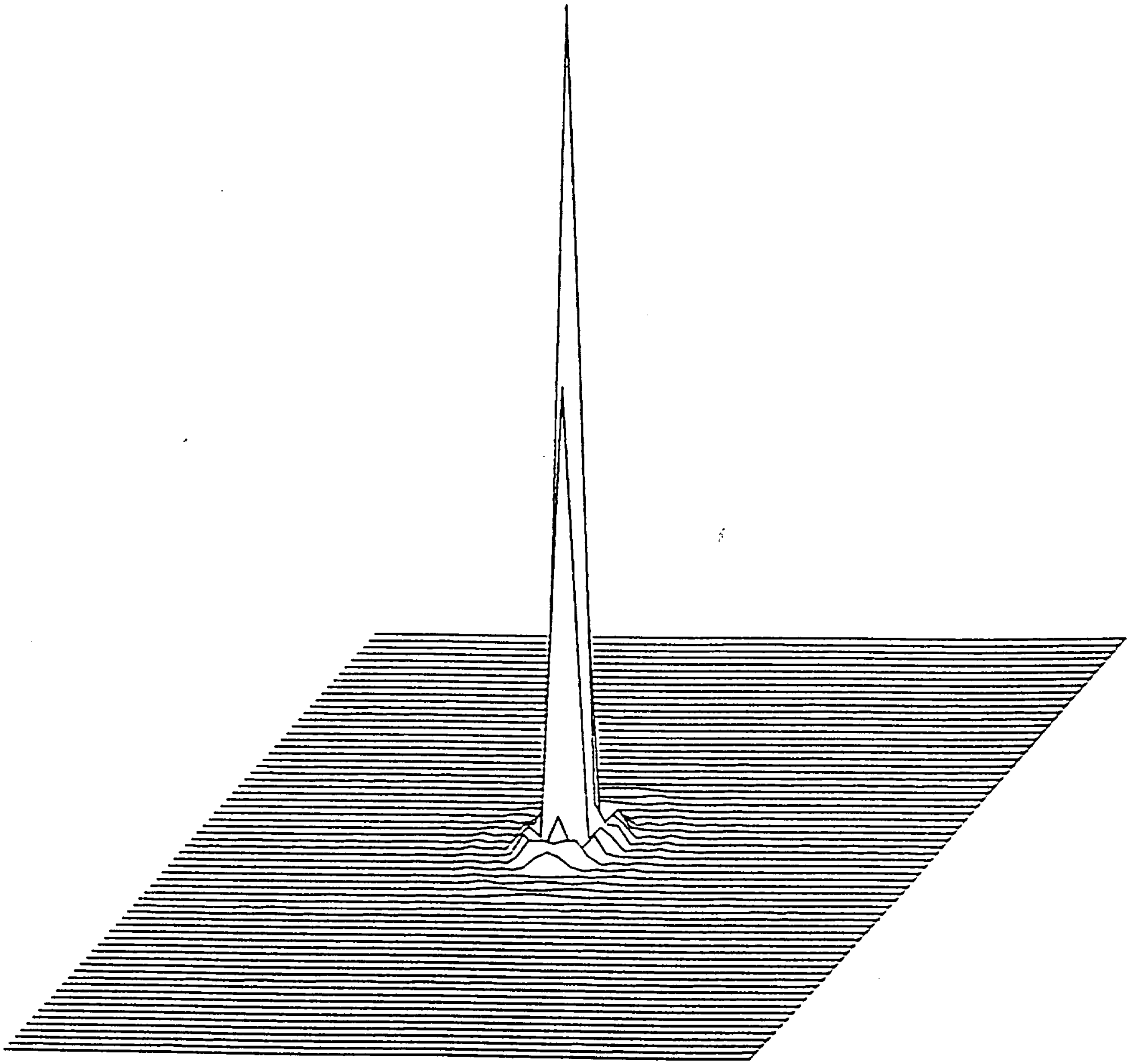

INTENSITY POINT SPREAD FUNCTION

24 EFL PRIMARY, 50 METER FOCAL RANGE
SUN MAR 14 1993
9.3000 MICRONS AT 0.00, 0.004DEG.
SIDE IS 1269.65 MICRONS.

BRET WHITESIDE
FIGURE 3.18

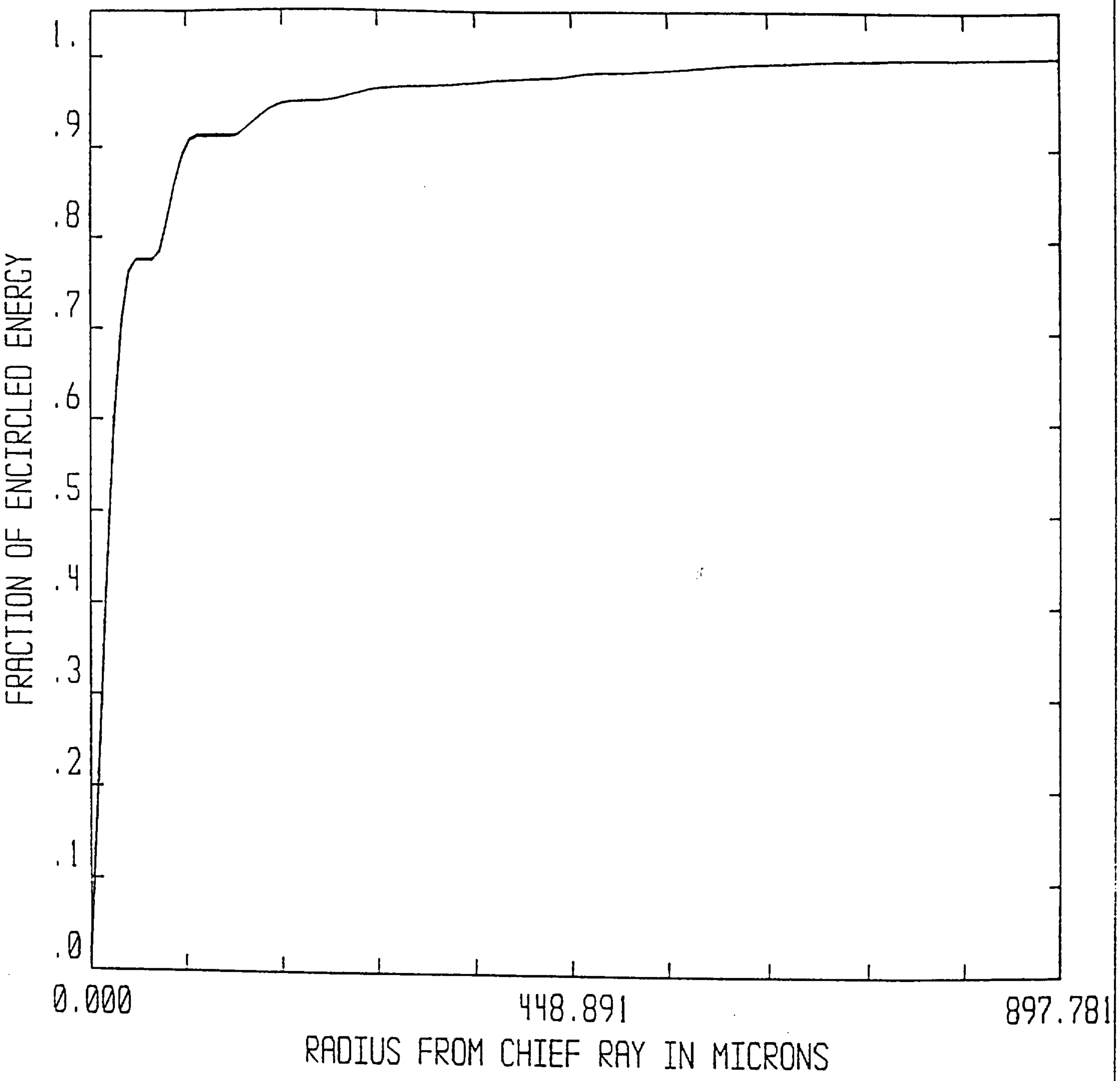

DIFFRACTION ENCIRCLED ENERGY

24 EFL PRIMARY, 50 METER FOCAL RANGE
SUN MAR 14 1993
FIELDS: 0.00, 0.00 DEG 0.00, 0.00 DEG

BRET WHITESIDE
FIGURE 3.19

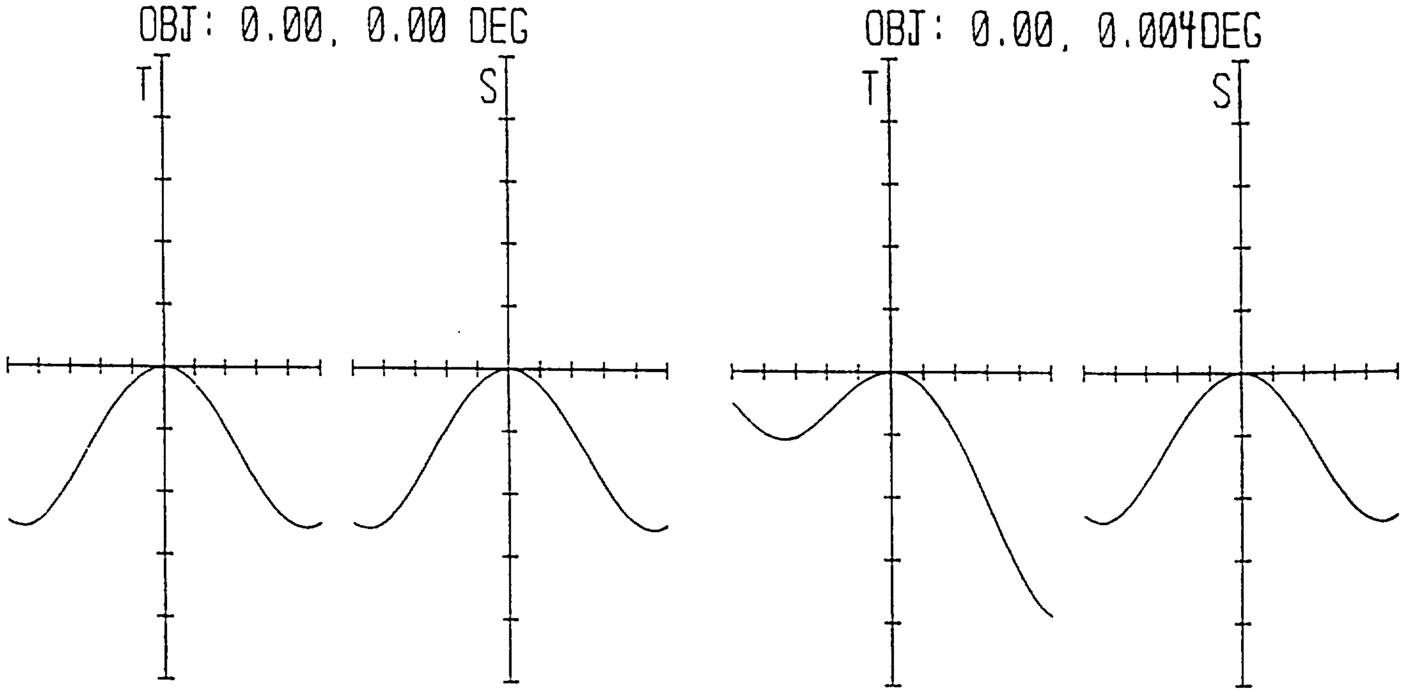

OPTICAL PATH DIFFERENCE

24 EFL PRIMARY, 50 METER FOCAL RANGE
SUN MAR 14 1993
MAXIMUM SCALE: -0.2000 TO 0.2000 WAVES.
9.300

BRET WHITESIDE
FIGURE 3.20

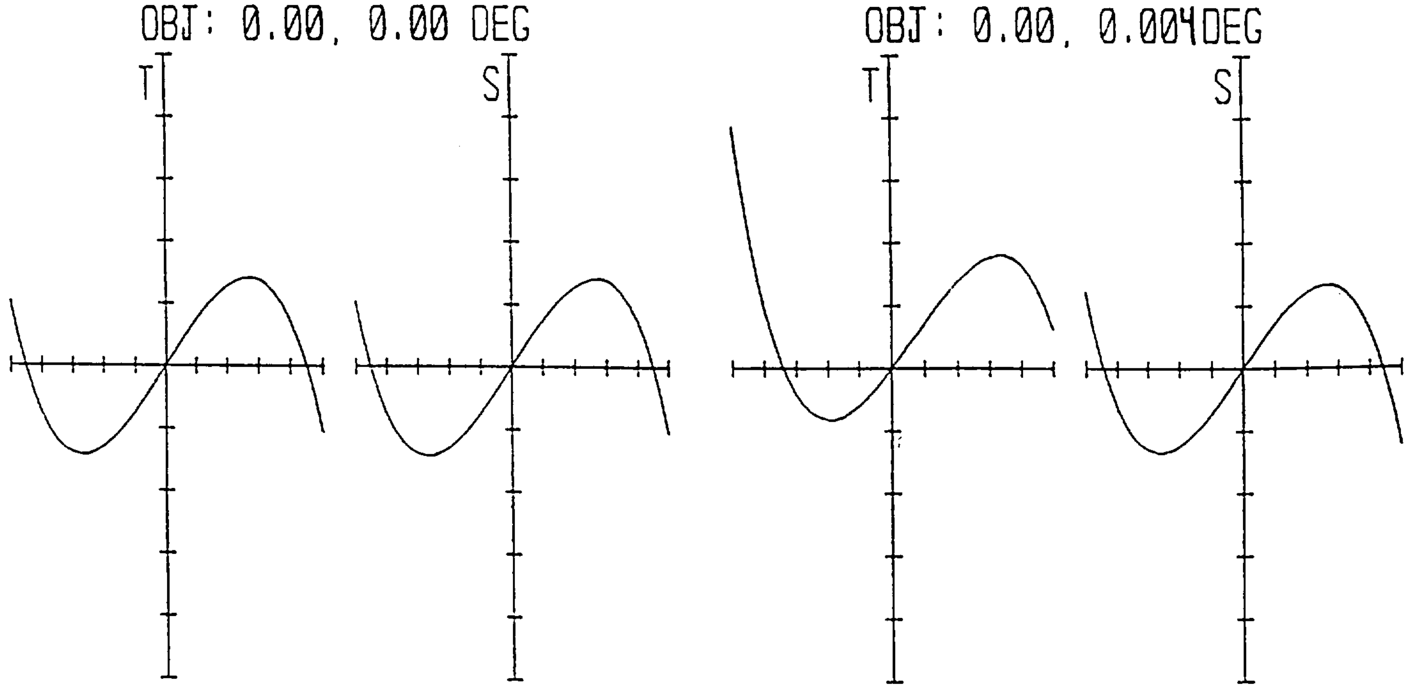

TRANSVERSE RAY FAN PLOT

24 EFL PRIMARY, 50 METER FOCAL RANGE
SUN MAR 14 1993
MAXIMUM SCALE: -50.0000 TO 50.0000 MICRONS.
9.300

BRET WHITESIDE
FIGURE 3.21

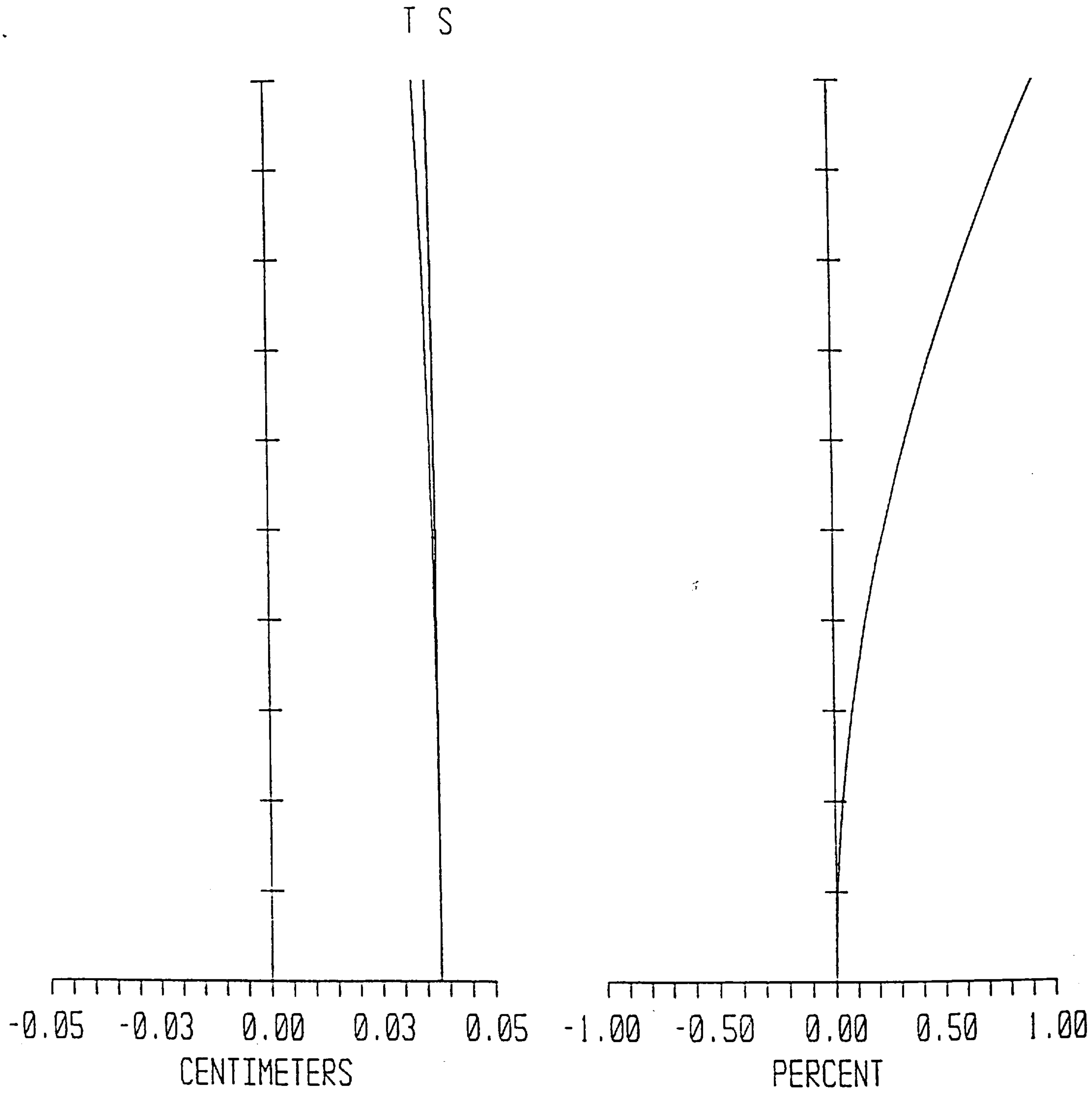

FIELD CURVATURE / DISTORTION

24 EFL PRIMARY, 50 METER FOCAL RANGE
SUN MAR 14 1993
MAXIMUM FIELD IS 0.004 DEGREES
WAVELENGTHS: 9.300

BRET WHITESIDE
FIGURE 3.22

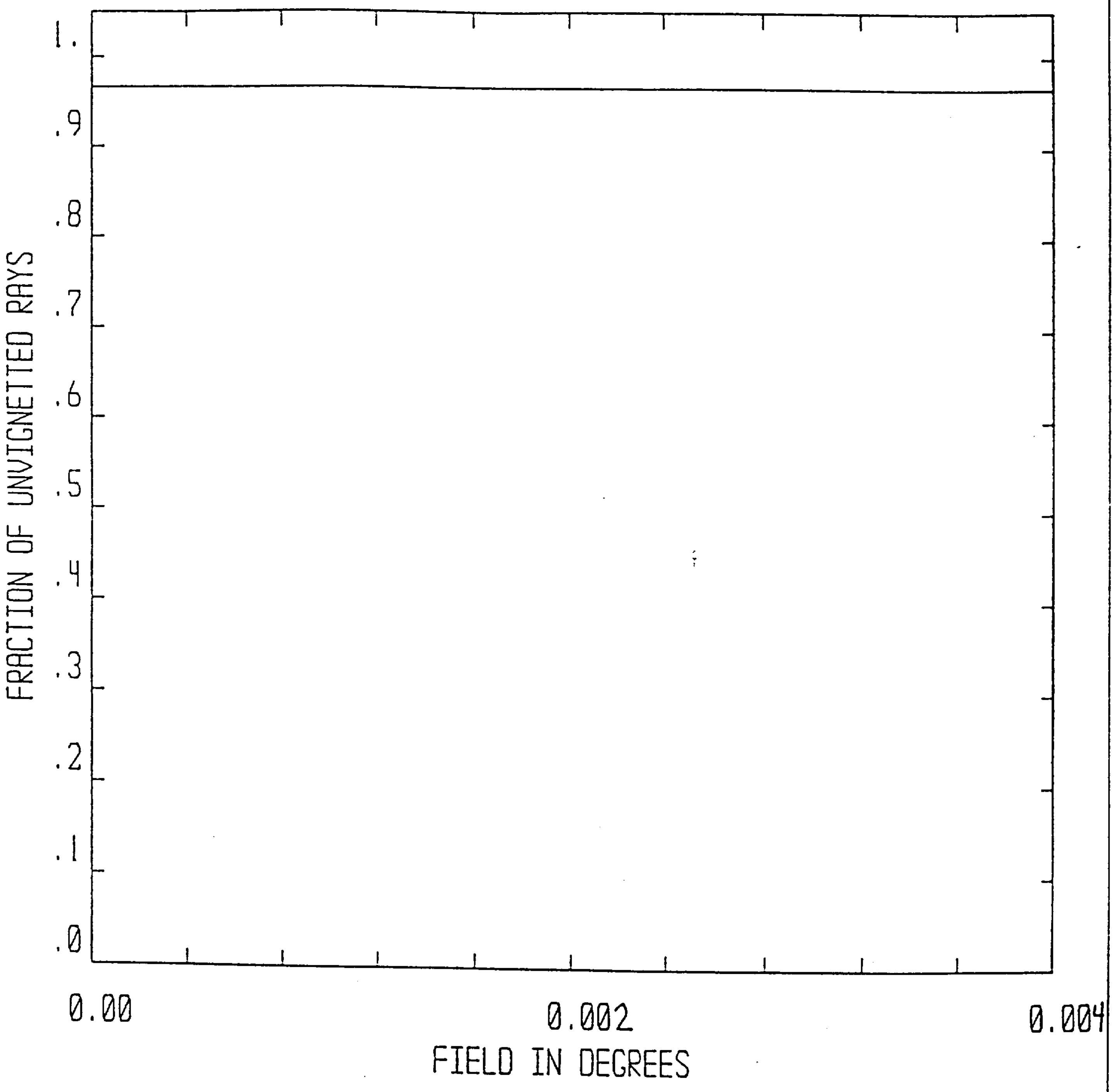

VIGNETTING DIAGRAM

24 EFL PRIMARY, 50 METER FOCAL RANGE
SUN MAR 14 1993

BRET WHITESIDE
FIGURE 3.23

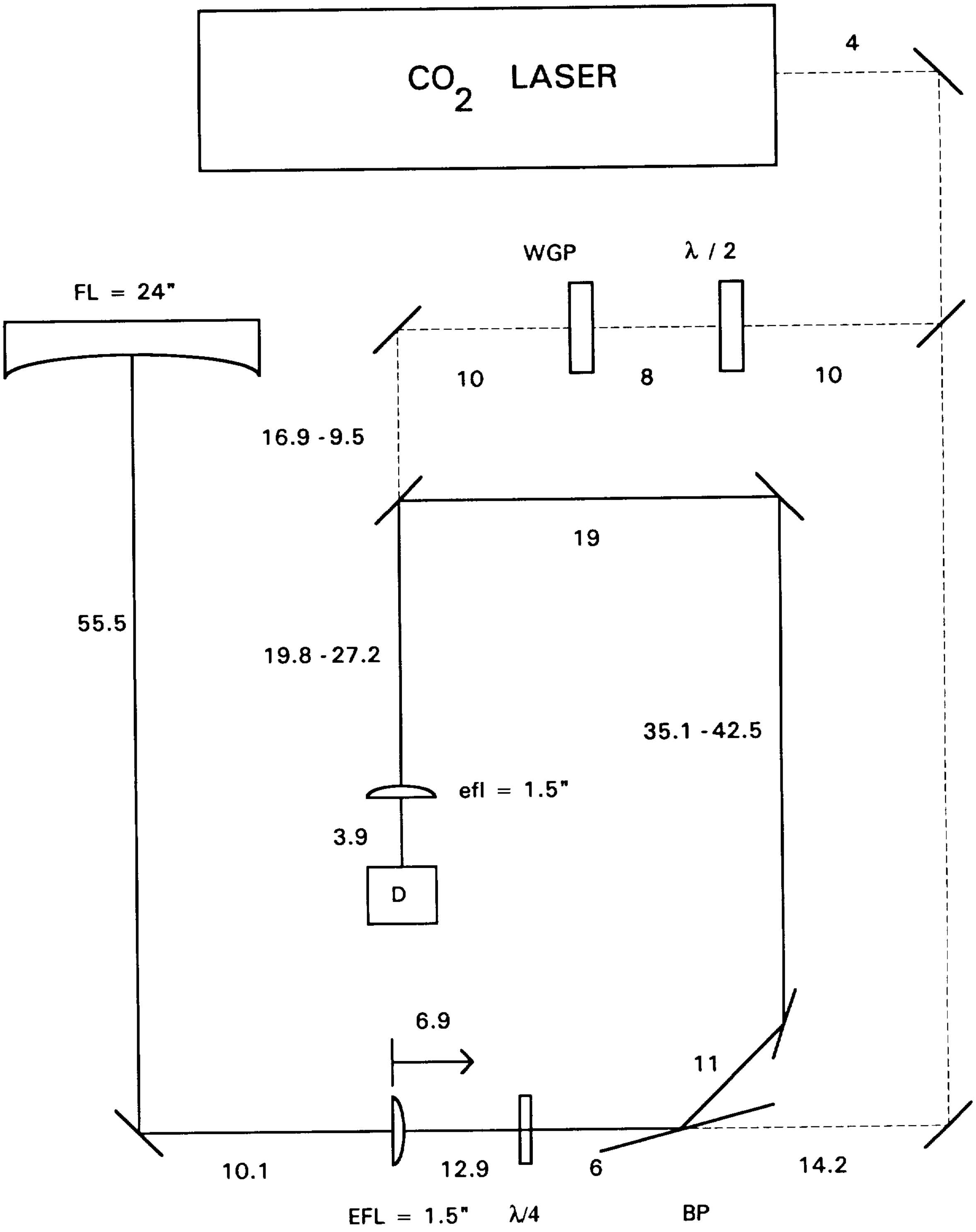

Figure 3.25. Layout of Receiver (component separations in centimeters)

CHAPTER 4

ASSEMBLY OF COHERENT LIDAR

Because of the fact that the CO_2 laser being used for our lidar has an output power of 7 Watts, and operates at a wavelength of 9.3 microns, it would be rather difficult to use it for rough alignment work. Therefore, a HeNe laser is mounted in tandem with the CO_2, in order to aid in alignment. The two beams were checked for alignment just after the first beam combiner and at a distance of 6 meters. It was estimated by visual means that the maximum separation between the two spots in the near and far fields would not be more than about 2-3 mm and thus the maximum misalignment between the two would be 1 mrad.

The center of the paraboloid mirror within its angle mount was 4.5" above the optical breadboard; therefore, a mount for the two lasers was machined, in order that both beams exit the laser cavities at this same height. In order to aid in locating the HeNe beam throughout the table, beam pointers were used. These beam pointers were aluminum rods having a tapered upper end that came to a point. These pointers could be installed in any of the 1/4-20 threaded holes on the table for precise alignment. In the following discussion, refer to Figure 4.1, where the various components described earlier are numbered for easy reference.

4.1 Transmitter Alignment

Note: Tip refers to changing the elevation angle of the surface normal, and tilt refers to changing the azimuthal angle. Component separations are given for a 5.5-meter target range from transceiver.

1. Adjust the height of a small iris by placing it at the output of the HeNe laser.

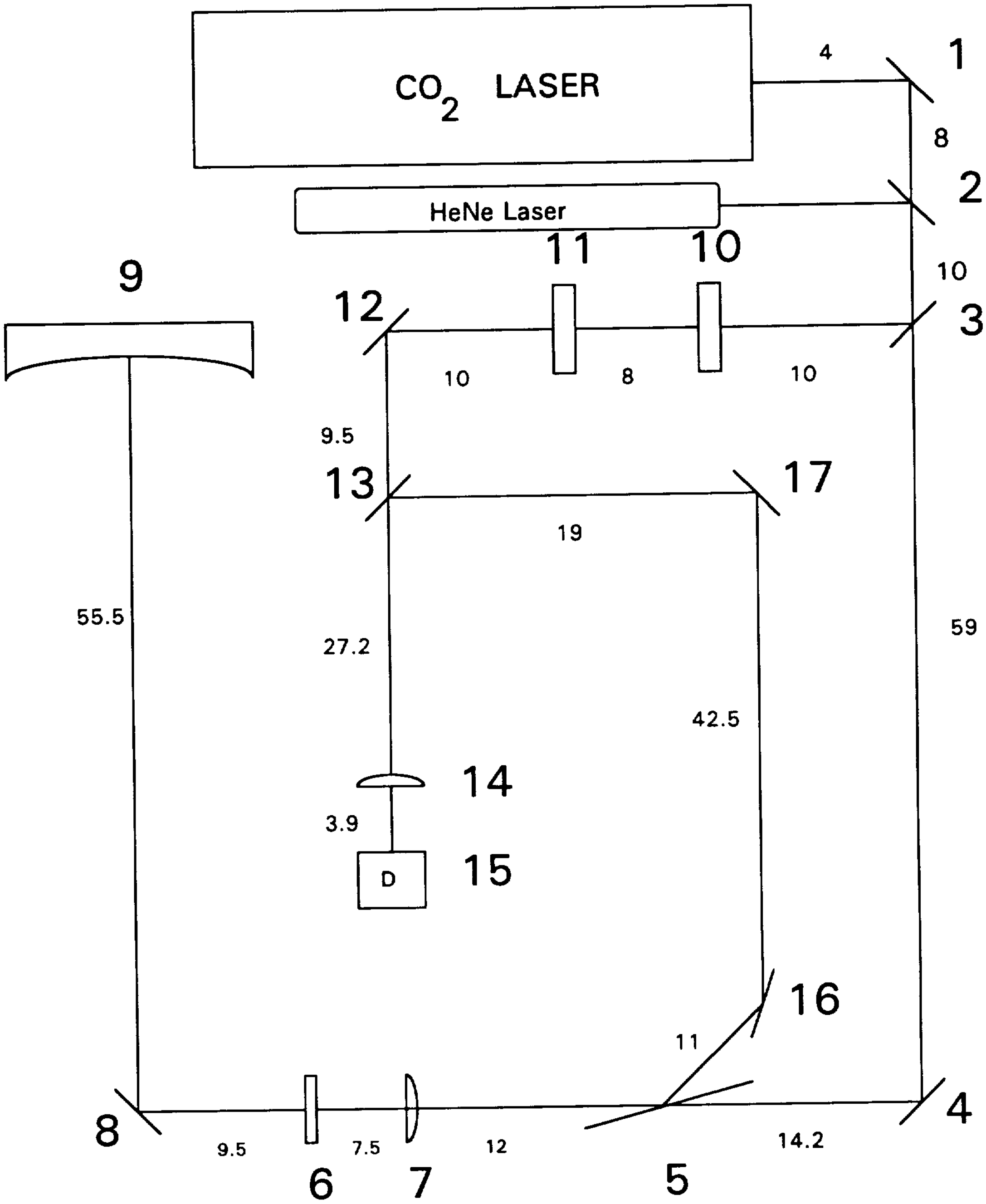

Figure 4.1. Layout of coherent lidar (components symbolized by large numerals and component separations given by small numerals) (Note: 6 = quarter-wave plate, 10 = half-wave plate, 11 = WGP)

2. Place the AR/AR coated beamsplitter (2) at the exit of the HeNe laser. Retroreflect the beam back toward the laser, as well as center the clear aperture in the beam.
3. Locate two beam pointers between (3) and (4) [one near (3), the other near (4)]. Adjust the tilt of (2) until the beam touches the beam pointer near (4).
4. Translate the base of (2) toward and away from the laser until the beam also touches the pointer at (2).
5. Continue steps 3 and 4 until the beam touches both pointers simultaneously.
6. Adjust the tip of (2) so that the beam passes through the iris placed near (4).
7. Insert the 5% beamsplitter, (3), and two more beam pointers along the local oscillator path between (3) and (12). Adjust tip and tilt and center the aperture within the beam to retro the beam to the laser.
8. Tilt (3), *i.e.*, rotate 45 degrees initially, in order to touch the pointer at (12). Translate the base along the axis defined by (2) and (4) to touch the pointer near (3).
9. Continue step 8 until the beam touches both pointers simultaneously. Adjust tip using iris located near (12).
10. With (3) aligned at 45 degrees, the finite thickness of the plate will introduce a displacement of the beam between (3) and (4) and so translate (2) toward the laser until the beam again touches the pointers between (3) and (4).
11. Translate (3) toward (2) until the beam touches the pointers between (3) and (12).
12. Insert a 100% reflector at (4), center the aperture, and adjust tip and tilt to retro the beam.
13. Insert a 100% reflector at (1), retro the beam and center the aperture.
14. Remove CO_2 laser from mount and place pointers on either side of the mount.

15. Adjust tilt, and translate the base of (1) along the axis defined by (1) and (4) until beam touches both pointers. Use iris to adjust tip.
16. Reinsert the CO_2 laser, and translate the base of (1) as in step 15, to center the beam within the laser aperture.
17. Remove (4) and insert a brick between (3) and (4), as close as possible to (3).
18. Translate (1) along the (1) - (4) axis until the CO_2 and HeNe spots coincide on the brick.
19. Adjust tip and tilt of (1) so that the two spots coincide at a range of 6 meters using a liquid crystal sheet or thermal paper.
20. Repeat steps 18 and 19 until the two spots coincide in the near and far fields simultaneously.
21. Turn off the CO_2 laser, remove the brick, reinsert (4), and place the pointers between (5) and (8).
22. Retro the HeNe beam, and center the aperture of (4).
23. Adjust tilt (rotate 45 degrees initially), and translate the base along the (1) - (4) axis to touch pointers between (5) and (8).
24. Adjust tip to send beam through iris at (8).
25. Insert the plane parallel plate, (5), retro the beam, and center the aperture.
26. Roughly tilt the plate to an incidence angle of nearly 70 degrees.
27. Adjust the tip so that the reflection from (5) is centered on the iris located as far from (5) as possible.
28. Locate a power meter at the beam reflected from (5) and turn on the CO_2 laser. (Be sure to warm up the CO_2 laser for at least 1 hour.)
29. Adjust the tip and tilt so that the reflected power from the *p*-polarized CO_2 laser is a minimum.
30. Turn off CO_2 laser and translate (4) along the (1) - (4) axis until beam touches pointers between (8) and (5).

31. Insert the elliptical reflector, (8), and retro the beam.

32. Insert the pointers between (8) and (9), and translate (8) along the (4) - (8) axis. Adjust tilt to touch both pointers, and then center the reflective surface by drawing the axes of an ellipse on a piece of paper and holding it up to the mirror.

33. Adjust tip of (8) to center beam on iris located near (9).

34. Place an additional iris between (7) and (8), centered and stopped down.

35. Insert 1.5" efl lens, (7), with the side with the shortest radius of curvature toward the laser source.

36. Center the lens aperture so that the beam is still centered on the iris at (9).

37. Adjust the tip and tilt of (7) to retro the beam toward the laser.

38. Repeat steps 36 and 37 until the lens is centered and untilted.

39. Using the iris at (9), insert another iris at a location along the (8) - (9) axis near (8), and center it in the beam.

40. Insert the 6" paraboloid, (9), and adjust tip and tilt to retro the beam through the iris at (8) and back to the laser.

41. Check to see that the beam reflected from (9) is centered about both irises simultaneously; if not, then translate the base of (8) and repeat this step.

42. Remove the iris at (8) and check for correct centering of the circular projected obscuration in the outgoing beam just behind the obscuration at (8).

43. If the diagonal is not correctly centered, readjust (8) vertically as much as required, and translate the obscuration along the (4) - (8) axis, if necessary.

44. If any horizontal translation was required in step 42, then (8) must be translated an equal amount along the (8) - (9) axis until the beam is centered about the beam pointers between (8) and (9). Repeat step 43 if necessary, and repeat step 41.

4.2 Local Oscillator Alignment

1. Since the (3) - (12) axis was already established in the above alignment procedures, begin by inserting the 5% reflector, (12). Retro the beam, and center the aperture.
2. Place two beam pointers between (13) and (15), and perform tilt and translation along (3) - (12) axis until beam touches both pointers.
3. Place iris near (15), and adjust tip.
4. Insert 96% reflector, (13), retro the beam, and center the aperture.
5. Place two more pointers along the axis formed by (13) and (17), but on the side of (13) where the reflection will be found.
6. Adjust tilt and translate (13) along the (12) - (15) axis until beam touches both pointers along (13) - (17) axis.
7. Place iris in beam reflected from (13), and adjust tip.
8. Translate (12) along (3) - (12) axis toward (9), until beam again touches pointers between (13) and (15).
9. Place iris on the other side of (15) along (12) - (15) axis, so that the aperture is centered on the beam.
10. Insert a mirror into the threaded lens holder, and adjust tip and tilt until the reflected beam is retro-reflected to the laser. Remove mirror.
11. Insert 1.5" efl lens with longest radius of curvature towards (15).
12. Adjust lens along x- and y-axis until beam is centered on iris.
13. Remove (14) from solid mount in threaded assembly.
14. Insert HgCdTe detector in dewar, (15), into mount.
15. Place iris near (13), with beam passing through aperture.
16. Adjust tip and tilt of (15) until beam is retro-reflected, and tighten firmly.
17. Insert the Wire Grid Polarizer, (11), retro the beam, and center the aperture.

18. Insert the λ/2 Plate, (10), retro the beam, and center the aperture.
19. Adjust the transmission axis of (11) to vertical (0 degrees).
20. Adjust the fast axis of (10) to horizontal (45 degrees).
21. Fill dewar with N_2, and block entrance aperture.
22. Turn on CO_2 laser. Warm-up for at least 1 hour before unblocking detector.
23. Monitor detector current with ammeter, being careful not to exceed one (1) milliampere.
24. Unblock the detector, and translate the detector along x- and y- axis until the current increases.
25. If the detector current shows no change, rotate the fast axis of (10) by 5 degrees, and repeat step 24.
26. Once detector is centered on the CO_2 beam, rotate the fast axis of (10) back to 45 degrees and re-insert (14).
27. Adjust detector as described above until centered.

4.3 Receiver Alignment

1. Insert a 100% reflector temporarily between (5) and (7), and retro the beam.
2. Insert a 100% reflector, (16), retro the beam, and center the aperture.
3. Place two pointers between (16) and (17).
4. Adjust tilt, and translate, as necessary, to align beam with pointers.
5. Place iris at (17), and adjust tip.
.6. Insert 100% reflector, (17), retro, and center.
7. Place pointers between (13) and (17), and adjust (17) as required.
8. Translate (13) along the (12) - (15) axis until the two beams coalesce horizontally on a card located near the surface of (13) closest to the detector. Alternately block and unblock either the local oscillator or the receiver to aid in this procedure.

9. Adjust the tip of (17) until the two beams coalesce vertically on a card located near the surface of (13).
10. Check that the two beams are concentric along the (13) - (15) axis, and adjust the tip and tilt of (13) as required. Using a card, alternately block and unblock either the local oscillator or the receiver to aid in this procedure.
11. Remove 100% reflector between (5) and (7), and insert $\lambda/4$ plate, (6). Retro the beam, center the aperture, and rotate the fast axis to 0 degrees.
12. Block detector, turn on CO_2 and warm up for at least one hour, then unblock detector.
13. Use a rotating solid target within the scattering volume and slowly rotate the fast axis of (10) until the local oscillator provides sufficient shot noise, while keeping the dc current under 1 mA.

4.4 Tolerance

In the above alignment procedures, it should be noted that the two most critical areas of alignment involve: 1) the co-alignment of the optic axis defined by the secondary diagonal mirror with the optic axis of the primary paraboloid mirror, since the paraboloid is designed for on-axis use, and 2) the co-alignment of the local oscillator and receiver beams.

An analysis was performed to determine the maximum tilt angle of the paraboloid before it no longer behaves as a diffraction limited element. From Figure 4.2, note that this maximum tilt angle is about 0.2 degree; thus, the maximum angle between the axis defined by the secondary and the axis of the primary is about 0.4 degree. Using the alignment techniques described above will enable a maximum misalignment of less than 0.2 degree. Using equation (2.12) to determine the maximum misalignment between the local oscillator (assumed to be incident normally on the detector) and the received beam, the angle is about 3 degrees. Using the above alignment procedures should yield a maximum misalignment of less than 0.3 degree. Figure 4.3 shows the fully assembled lidar.

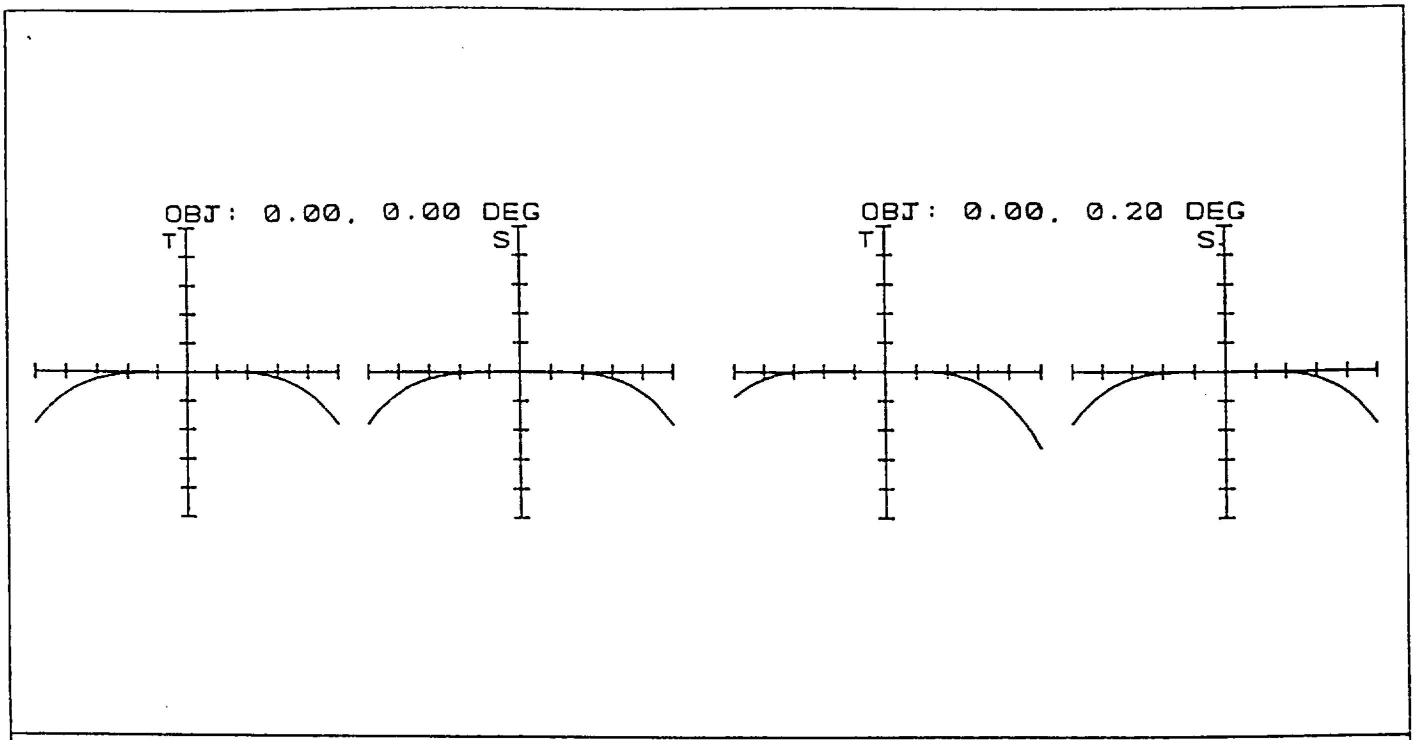

OPTICAL PATH DIFFERENCE

F/4 PARABOLOID, 5.5 METER TARGET RANGE
FRI JUN 04 1993
MAXIMUM SCALE: -0.5000 TO 0.5000 WAVES.
9.300

BRET WHITESIDE
UNIVERSITY OF ARIZONA

Figure 4.2a

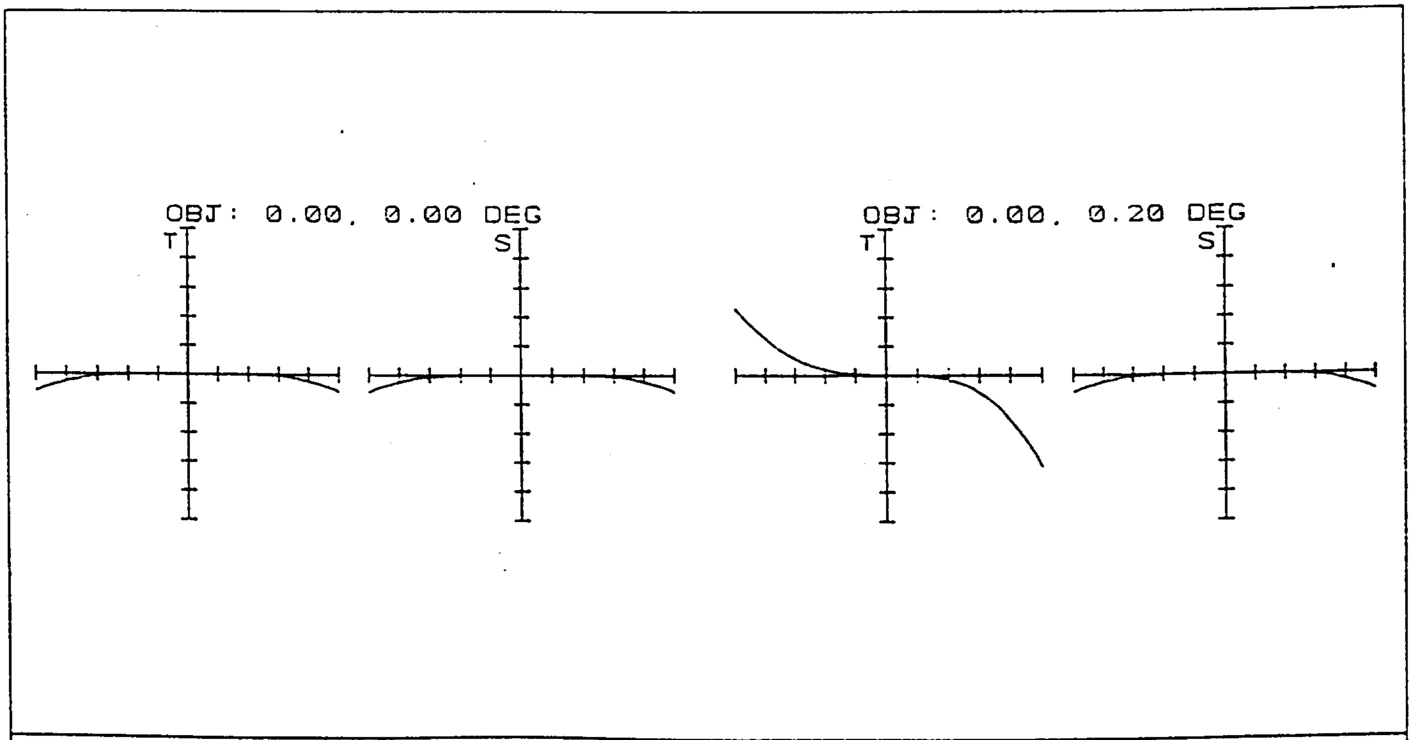

OPTICAL PATH DIFFERENCE

F/4 PARABOLOID, 50 METER TARGET RANGE
FRI JUN 04 1993
MAXIMUM SCALE: -0.2000 TO 0.2000 WAVES.
9.300

BRET WHITESIDE
UNIVERSITY OF ARIZONA

Figure 4.2b

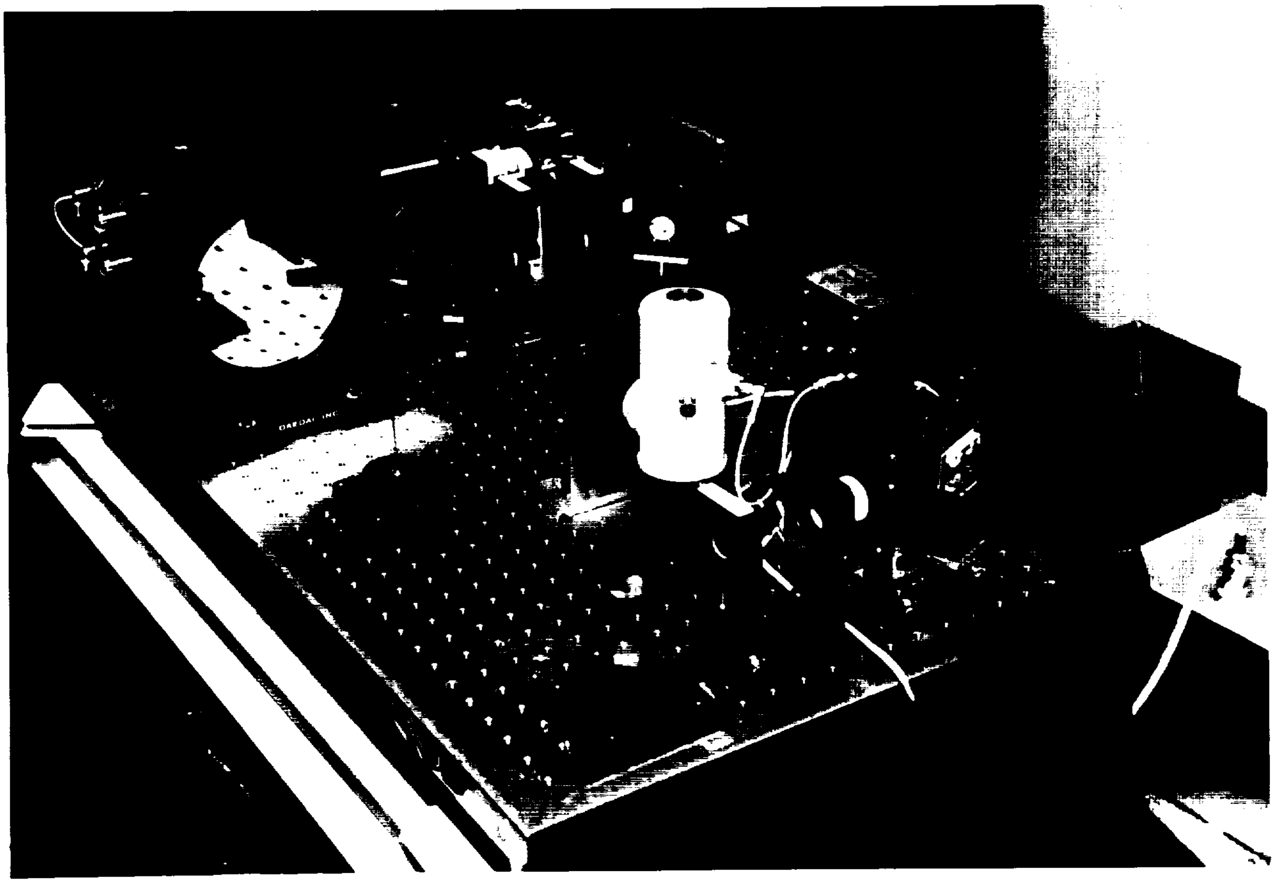

Figure 4.3. Photograph of assembled coherent lidar

CHAPTER 5

TESTING OF COHERENT LIDAR

5.1 Transmitter Performance

In order to test the transmitter portion of the lidar, several scans of the output beam were performed in the region of the waist. The various computations made earlier (see Tables 3.4 and 3.5) were based on purely aberration-free optics and did not take into account the circular obscuration of the diagonal mirror in the outgoing beam. In order to understand the effects caused by this obscuration, a theoretical discussion of apertured Gaussian beams was sought. A very detailed discussion of such effects is found in the paper entitled: "Parametric Study of Apertured Focused Gaussian Beams" (Holmes *et al.*, 1972).

For a beam radius, w, which is diffracted by an annular aperture that occupies a region, $a \leq \rho \leq b$, the irradiance is proportional to:

$$I(r,z) \propto \left| (2\pi/\lambda z) \int_a^b \rho \exp\left[-(\rho/w)^2 - \left(i\pi\rho^2/\lambda R \right) \right] J_0(2\pi\rho r/\lambda z) \exp\left(i\pi\rho^2/\lambda z \right) d\rho \right|^2 \qquad \textbf{(5.1)}$$

where r is the radial position coordinate, z is the axial position coordinate, R is the longitudinal distance from the annular aperture to the waist, and λ is, of course, the wavelength.

5.1.1 Irradiance along Optic Axis

An axial scan of the transmitted beam was performed using an aperture of 0.032 inch diameter placed in front of a thermopile detector. The range to the waist was determined to be 570 cm from the primary of the beam expanding telescope. As a check against the theoretical expression given above in equation (5.1), a theoretical curve was also plotted on the same graph after setting $r = 0$ and letting z vary over the same experimental values (see Figure 5.1). In order to get a good match between theory and experiment, the actual spot size at the paraboloid had to be changed from the theoretical value given in Table 3.5.

Based on diffraction alone, the spot size at the paraboloid for a waist located at the range given above was predicted to be about 4.5 cm, whereas in the theoretical expression (5.1), a value of 3.5 cm was used. Thus, the spot size at the paraboloid is 20% smaller than a perfect aberration-free system, and the waist formed within the beam expander must be about 20% larger than a perfect aberration-free spot size.

5.1.2 Irradiance in Plane of Waist

Once the peak in the axial irradiance was found, a scan was performed in the transverse plane along a horizontal and a vertical direction (see Figures 5.2 and 5.3, respectively). The same spot size at the paraboloid as was found for the axial scan, 3.5 cm, was used when fitting the theoretical curve to the data.

The scattering volume can be determined from this data. However, since the actual signal received depends on the characteristics of the receiver, the actual scattering volume cannot be strictly specified. If it is assumed for the moment that equation (2.31) is valid, then the scattering volume of:

$$V_{\text{scatter}} = 90 \text{ mm}^3 \quad \text{for} \quad R = 570 \text{ cm}$$

is obtained, where the theoretical data found in Figures 5.1-5.3 were used to determine the parameters z_R and w_0 ($z_R = 8$ cm, and $w_0 = 425$ μm).

FIGURE 5.1
NORMALIZED AXIAL IRRADIANCE

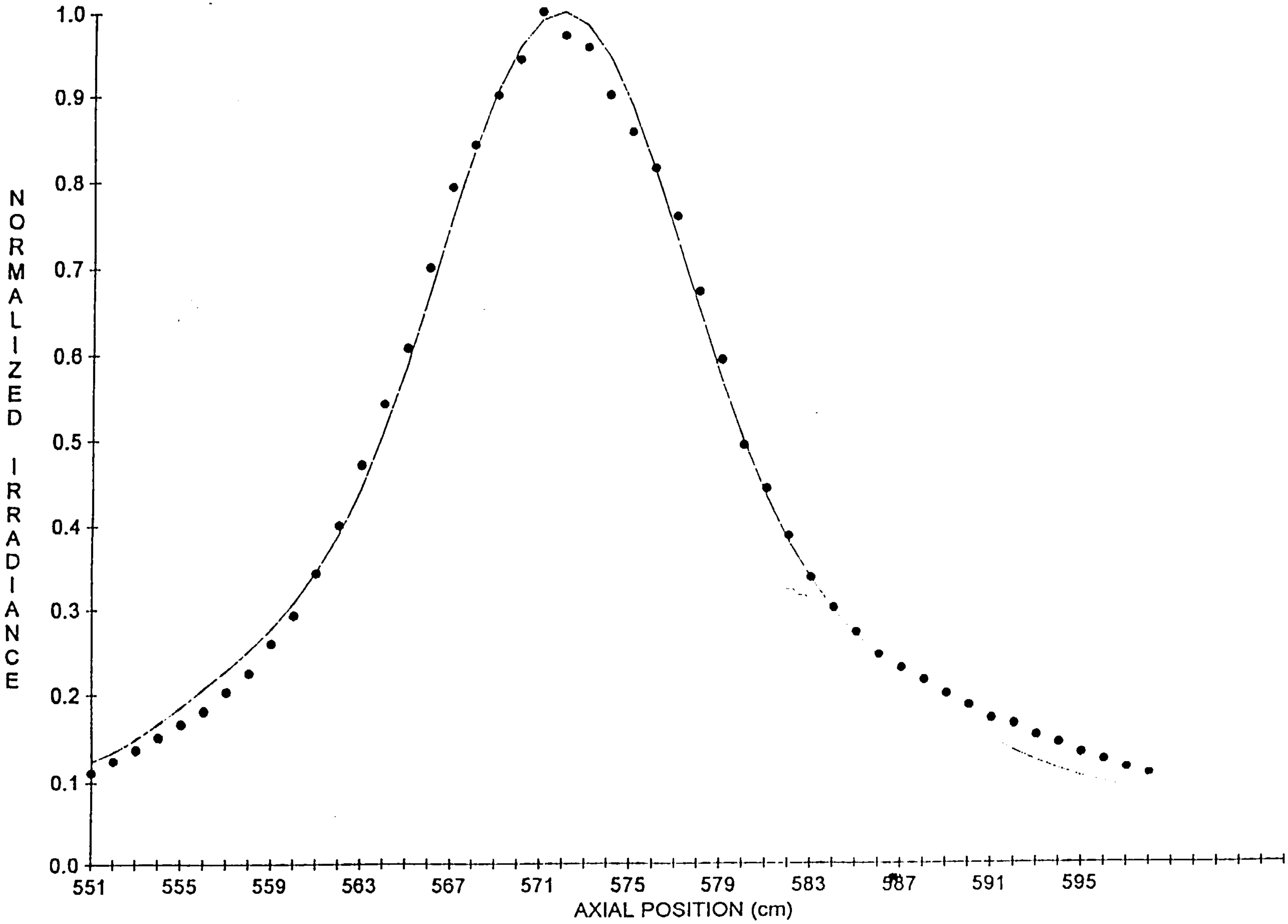

FIGURE 5.2

NORMALIZED RADIAL IRRADIANCE

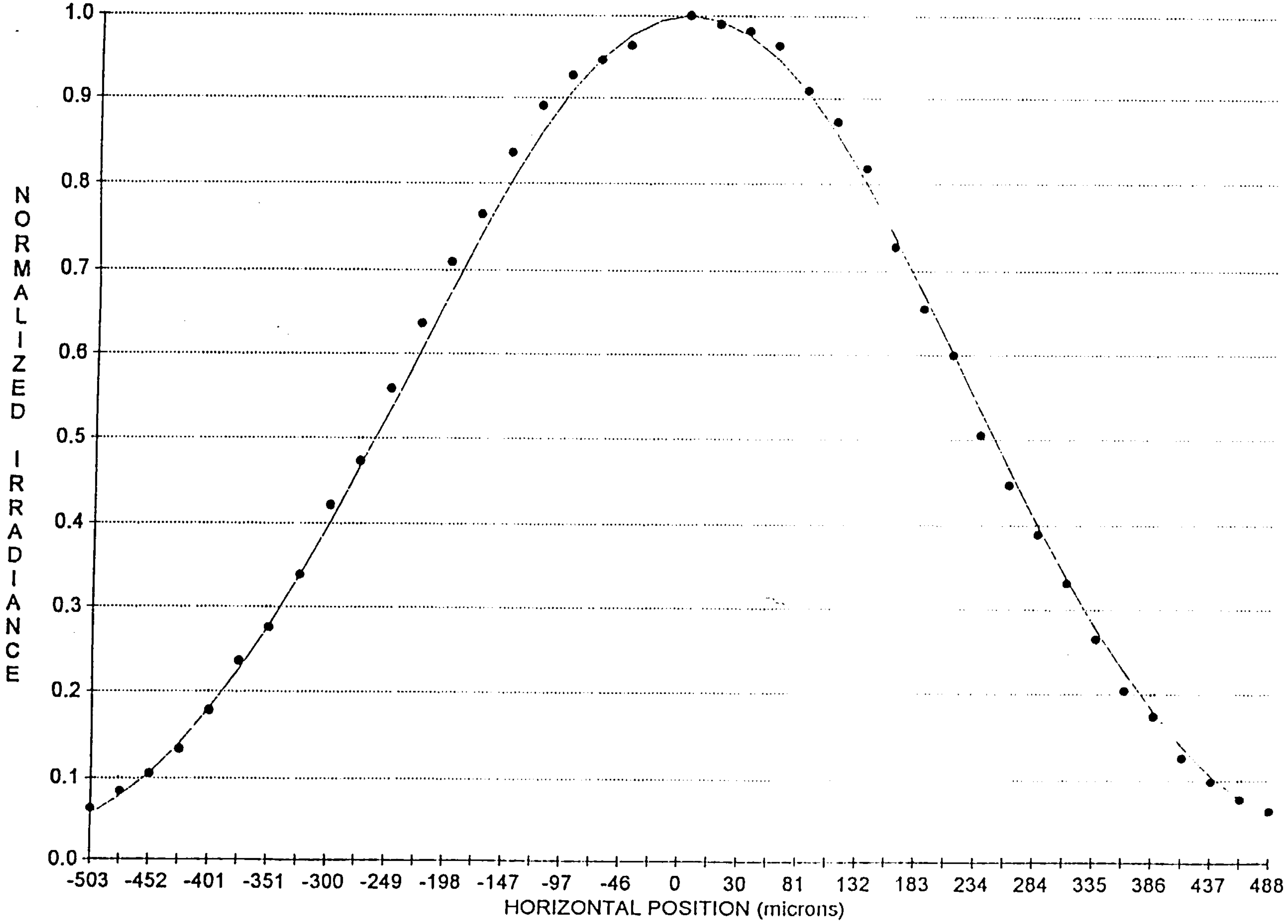

FIGURE 5.3
NORMALIZED RADIAL IRRADIANCE

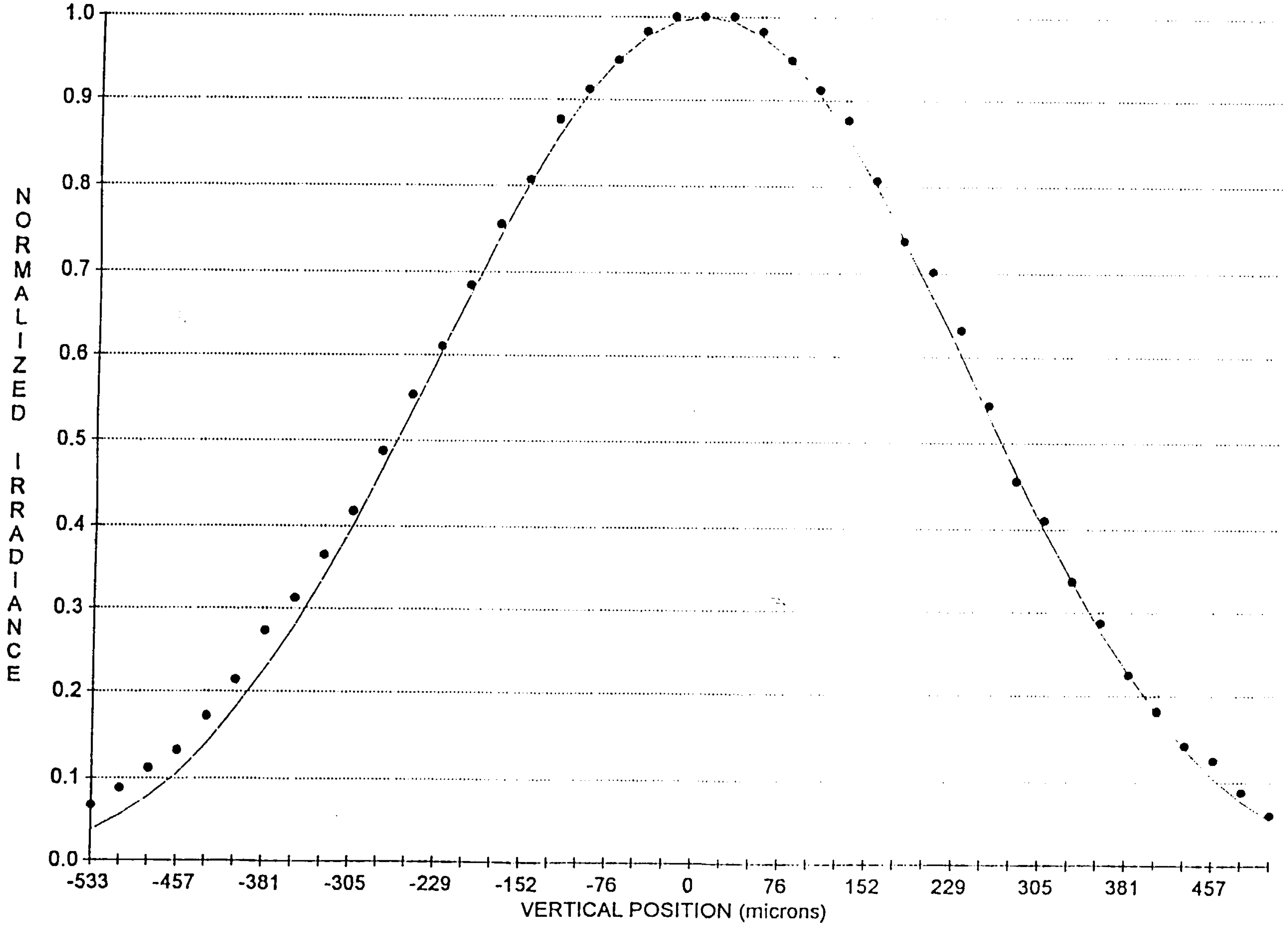

5.2 Local Oscillator Performance

5.2.1 Narcissus

Narcissus was a problem which plagued the lidar from the moment it was first tested. As is obvious from a careful look at the beam expander, the outgoing beam is directed back towards the diagonal mirror only to be sent through the quarter-wave plate a second time and then down the receiver path to the detector. Thus, any reflection from the optics following the quarter-wave plate will act like the local oscillator and will add to the dc signal detected by the system. The problem with this is that the optical attenuator described earlier cannot control the amount of local oscillator power needed for maximum detection sensitivity.

In addition, it was also discovered that because the two sources of local oscillator were nearly equal in magnitude and an optical path difference was present between the two, they were able to interfere and produce large fluctuations in the dc current through the photodetector.

5.2.2 Anti-Narcissus Stop

The most obvious solution to the paraboloid's contribution to narcissus was to insert an opaque obscuration centered on the primary axis near the paraboloid. The size of the stop was chosen to be smaller than the projected diameter of the diagonal mirror so that it would not increase the obscuration ratio and thus not increase diffraction effects. Even though some energy would leak around the Anti-N stop only to be bent toward the detector, the irradiance of this off-axis region would be reduced from the axial region, and these rays would refract through the expansion lens and be aimed off-axis.

This quick fix did, in fact, work quite well and did not produce any changes in the transmitted waist shown in the previous section. The dc current became much more stable with fluctuations of a few percent, rather than the 50% to 100% instabilties seen without the stop.

5.2.3 Relocation of Quarter-Wave Plate

After removing the largest source of narcissus as described above, several smaller sources became more pronounced. The biggest culprit was the quarter-wave plate itself. Being a flat, it tended to produce retro-reflections which would focus quite well in the plane of the detector and thus became a nuisance to handle. The trick was that these reflections which entered the receiver path had to be scattered at the second surface of the quarter-wave plate, which meant that the field vector was rotated by 90 degrees, as described previously, just as the scattered field from the aerosols. It was decided that a tilt of the plate at a slight angle (about 2-3 degrees) would be large enough to reflect the beam off-axis but would not be too much, so as to change the required thickness of the quarter-wave plate for the wavelength being used.

After employing a small tilt, the third and final source of narcissus became apparent - the expansion lens. With even the absolute lowest reflectance coating available, there was still a significant level of power being reflected from this component. The final solution was not to try and reduce the reflectance of the lens but to remove its effect. This was accomplished by placing the tilted quarter-wave plate after the lens, being careful to protect the plate from the extremely high irradiance at the waist following the lens. Now any reflected energy could reach the photodetector only through the local oscillator path, which could be precisely controlled with the attenuator.

5.3 Receiver Performance

5.3.1 Experimental SNR

In order to test the performance of the receiver, a solid target with a known reflectance, *i.e.*, 400 grit silicon carbide paper oriented at 45° to the laser beam and located at a range of 550 cm, was rotated at a constant angular velocity, in order to produce a doppler shift in the scattered electric fields as described previously. The average power signal-to-noise ratio was determined using an HP Scanning Spectrum Analyzer. The signal level was found to be -9 dBm, while the noise floor was measured at -76 dBm. Thus, the actual average power SNR was:

$$\langle \mathrm{SNR} \rangle_p = 67 \text{ dB}$$

5.3.2 Theoretical SNR

With reference to equation (2.6), it is known that the detector current will have a dc and an ac component. Both the local oscillator and the backscattered power will contribute to the dc term; however, in the case of heterodyne detection, the local oscillator power is deliberately designed to be the dominant source of detector current. If the local oscillator power is made large enough so that the random arrival of photons at the photodetector becomes the dominant source of noise, the detector will operate under so-called shot-noise limited or photon-noise limited performance (Saleh and Teich, 1991). Under these conditions, the total mean photocurrent through the detector will be given by:

$$\bar{i} = \bar{i}_{\mathrm{dc}} + \bar{i}_{\mathrm{ac}}$$

$$\bar{i} = \eta e \frac{P_L}{h\nu} + 2\eta e \frac{\left(P_L \bar{P}_r\right)^{1/2}}{h\nu} \cos \omega_D t \qquad \textbf{(5.2)}$$

and the photocurrent variance (assuming Poisson statistics) will be:

$$\sigma_i^2 = 2e\bar{i}\Delta f \tag{5.3}$$

The average power signal-to-noise ratio is defined as:

$$\langle \mathrm{SNR} \rangle_p = \frac{\langle \bar{i}_{\mathrm{ac}}^2 \rangle}{\langle \sigma_{\mathrm{i}}^2 \rangle} \tag{5.4}$$

where the average is taken over an interval which is long compared to $1/\omega_d$. The cosine term in the denominator will vanish to obtain the following theoretical average power signal-to-noise ratio:

$$\langle \mathrm{SNR} \rangle_p = \frac{\eta \bar{P}_r}{h\nu\Delta f} \tag{5.5}$$

Table 5.1 summarizes the data used for calculating the theoretical average power signal-to-noise ratio.

TABLE 5.1	
THEORETICAL AVERAGE POWER SNR	
Transmitted Power (Watts) =	0.08
Reflectance of Scattering Target (1/sr) =	0.01
Angle of Incidence (Degrees) =	45
Range to Target (cm) =	550
Radius of Receiver Aperture (cm) =	7.62
Solid Angle Subtended by Receiver (sr) =	6.03E-04
Power collected by Receiver Aperture (Watts) =	4.824E-07
Optical Efficiency =	0.29
Heterodyne Detection Efficiency =	0.5
Backscattered Power Incident on Detector (Watts) =	6.995E-08
Quantum Efficiency of Photodetector =	0.47
Planck's Constant (J-s) =	6.63E-34
Frequency of Optical Radiation (Hz) =	3.226E+13
Energy per Photon (J) =	2.139E-20
Bandwidth (Hz) =	30000
Theoretical Average Power SNR (dB) =	77

Although a 10 dB difference between the experimental and theoretical SNR might seem excessive, as a general rule, up to an order of magnitude degradation between theory and experiment is typical (Foord *et al.*, 1983). Foord *et al.* (1983) attribute speckle as one significant source of the discrepancies found between the theoretical and experimental values. It was determined experimentally that half of the total power in the power spectrum was contained in a circle of 6 cm diameter at the receiver plane. Thus, the effective solid angle subtended by the receiver plane would be:

$$\Omega_{\text{receiver}} = 9.3 \text{ x } 10^{-5} \text{ sr}$$

and thus the theoretical mean power SNR will decrease by 8 dB using this effective solid angle. The residual 2 dB discrepancy could be attributed to optical mismatching due to beam aberrations and misalignment.

The 6-cm diameter speckle size can be verified approximately using expression (2.10), where Ω_d represents the solid angle subtended by the transmitted waist at the plane of the receiver. The beam diameter was found experimentally to be about 1 mm at a range of 570 cm; thus, the solid angle subtended by the beam at the receiver is:

$$\Omega_d = 2 \times 10^{-8} \text{ sr}$$

After substituting the wavelength and the above solid angle into equation (2.10) and solving for the speckle area at the receiver plane, the result is:

$$A_r = 40 \text{ cm}^2$$

which yields a diameter of about 6 cm.

5.3.3 Receiving Efficiency as a Function of Target Location

As was mentioned previously (see section 2.3), scattered energy from aerosols which are located far from the transmitted waist does not mix as efficiently as that from particles near the waist. In order to determine the efficiency of the receiver as a function of target particle location relative to the transmitted waist, a rotating Silicon Carbide disk was translated along the optic axis of a laser beam with the waist located at a range of 570 cm, and the relative backscattered power was recorded (see Figure 5.4). This plot shows that the efficiency is 3 dB below the maximum found at the waist for points located a distance of about 12 cm from the waist. Thus, the scattering volume will be somewhat larger than that computed previously using the experimentally determined Rayleigh range of 8 cm.

Using the previously determined spot size at the waist, *i.e.*, $w_0 = 425\ \mu\text{m}$, and a longitudinal length of 24 cm, a better approximation to the scattering volume would be:

$$V_{\text{scatter}} = 140\ \text{mm}^3 \quad \text{for} \quad R = 570\ \text{cm}$$

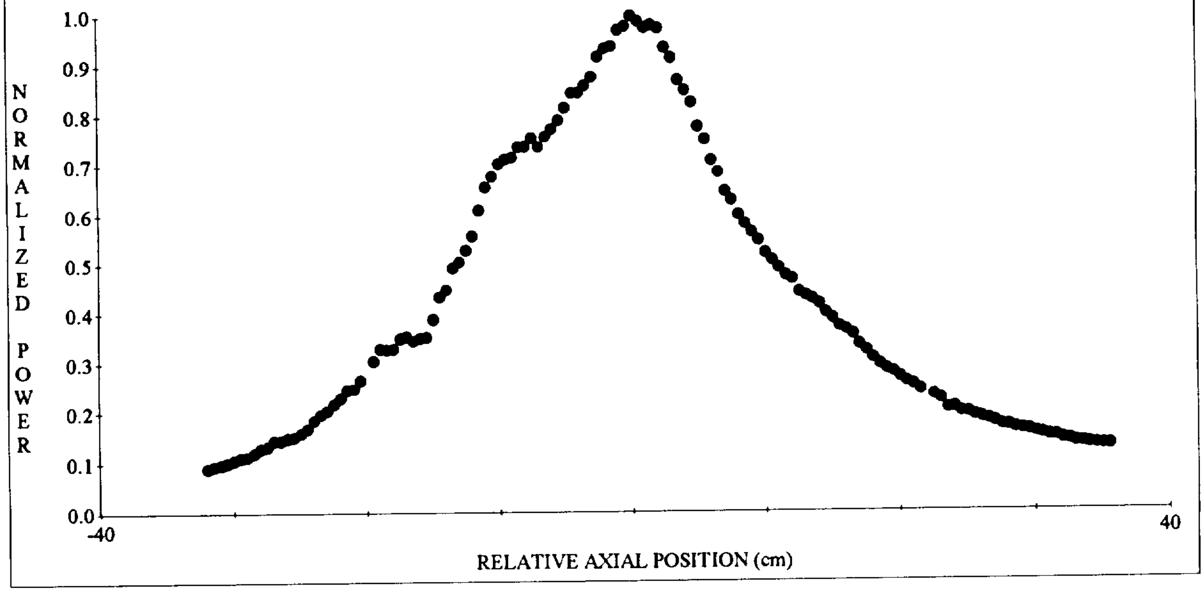

FIGURE 5.4

DETECTED POWER VS. DISTANCE FROM WAIST

APPENDIX

ANALOG-TO-DIGITAL CONVERSION SOFTWARE

Data acquisition for the coherent lidar is achieved through the use of a 4-band spectrum analyzer which includes four distinct band pass filters, four separate multipliers (for squaring the inputs), and four integrators. The analog-to-digital converter (Data Translation, Model DT2821-F-16SE) provides the TTL pulses for resetting the integrators, beginning and ending the integration, and then samples the four separate outputs. Once the analog output has been sampled and converted into an Analog Data Value by the Successive Approximation Register (SAR), the ADV's are stored into a file that is set up by the ATLAB subroutine library provided with the ADC. This file can be read sequentially using an ATLAB subroutine, and the ADV's can be converted into an analog voltage by use of the formula:

$$\text{Analog Voltage} = [\ \text{ADV}\ (\text{PFS} - \text{MFS}) / \text{NOC}] + \text{MFS},$$

where PFS = Plus Full Scale (+ 10 V for a gain of 1), MFS = Minus Full Scale (-10 V for a gain of 1), and NOC = Number of Codes (4096 for a 12 bit ADC).

The ADC is a 12-bit, 16-channel ADC which can be programmed to provide a gain of 1, 2, 4, or 8, allowing the input voltages to vary between +10V to -10V, +5V to -5V, +2.5V to -2.5V, or +1.25 to -1.25V, respectively. Due to the need for control of the integrators, a program (ATLAD03.FOR) was written using FORTRAN77 which called the ATLAB subroutines and accounted for the required time delays. In addition, this program also converted the analog data values into true analog voltages, which were subsequently stored in separate data files corresponding to each channel's output.

C ATLAD03.FOR -- ATLAB SOFTWARE TRIGGERED A/D CONVERSION

The program starts by including two programs provided with ATLAB, which serve to provide a subroutine entry point for FORTRAN callable subroutines and to provide error definition files. After the INCLUDE statements, PARAMETER statements are used to assign a constant to a symbolic name. The use of a PARAMETER statement invalidates any changes to the constant later in the program. Note that the first letter of the symbolic name must be a letter between I and N to represent an integer constant. INTEGER statements are used to define one-dimensional arrays for storing the channel number and channel gain information input by the user. The number following the asterisk declares whether the memory location for the variable must contain 1, 2, or 4 bytes of data.

C Storage for unit configuration data

An array is established that will store the data concerning the ADC unit configuration in an array of size determined by the variable KCONFIG, which has been defined within the program ATLDEFS.FOR. The named COMMON statement allows ATLAD03 to share the data stored in the array ICONFIG, which can also be manipulated by another program unit, *i.e.*, ATLDEF.FOR.

C Equivalence the data array with the variables

The data which is stored in the configuration file, ICONFIG, will be shared with the variables BASEADR, CDEVID, etc.

C Declare the header items

Type statements are used to declare the type of variable being defined to contain an integer or character data.

C Define the data equivalences for the file header

The data stored in the array IFHDR will be shared by the variables DEVID, DEVFLAGS, etc.

C Local variables

Type statements are used as described previously for the variables which are found only in this program and for data which are not shared by other programs. DATA statements are used to assign particular values to the variables and elements of the arrays. The variable(s) FNAME(_) is assigned a character name, which will later be used in an OPEN statement for writing data to a particular file.

C Begin program

A message is written to the user to explain the purpose of the software.

C Initialize the ATLAB subroutines

This subroutine initializes all the subroutines which will be subsequently called. All of the ATLAB subroutines are called as functions by ATLAD03.FOR, which is possible only because the program ATLDEFS.FOR declares all the subroutines as INTEGER*2. It should also be noted that the functions called by ATLAD03.FOR will return a value which corresponds to the error status. These error codes are provided by the program ATLERRS.FOR, and the argument passed by the function being called can be tested using logical expressions to determine the error status.

C Address the board

Since only one board has been inserted into the computer's AT Bus, it is referred to as board #1. ALSB selects the board to which all subsequent ATLAB subroutines apply.

C Perform a reset on the device

ALRSET resets the board to its initial power-up state.

C Warn the user about conflicting line drivers

Since damage can be done to the digital ports which will subsequently be enabled for output if they are being driven by the output of some other device, a warning message is given. The message asks the user whether or not he wishes to continue, and then accepts a single character response ignoring any leading blanks. If the user does not respond affirmatively, the program jumps to the end and quits. Note the use of "A" to specify a character response and the "\" to prevent an end-of-record mark being inserted by the format controller, allowing subsequent I/O statements to be written to the same record.

C Display the current unit configuration

A subroutine called DUMPCONFIGURATION is INCLUDEd with this program to give the user ADC configuration data.

C Open the data files

ALFOPN opens a data file which will store the ADV's for all channels selected. The second argument of this function, IALWRITE, passes an integer value of 1 in order to open the file for writing. This variable has been defined in the ATLAB software. The OPEN statements provide access to seven additional files, which will store the converted analog voltage data for each channel as a separate file. One additional file stores the file annotations, which allows the user to annotate each set of scan data. These files are given the names specified by the DATA statements found in the local variable section. Since the OPEN statements specify a particular unit number for each file, WRITE statements can use a particular unit number to write to a particular file.

C Request scan count, channels, gains, and comments

In the present version of ATLAD03.FOR, seven channels are "hardwired."

C Get the channel number

A DO loop is begun that prompts the user for channel gain information. A message is written to the screen to inform the user as to the "Entry #" and the " -Channel " number which are currently being selected.

C Get the gain

The user is prompted to provide the gain setting (1, 2, 4, or 8) for the particular channel. The response is stored in the array ADGAINS.

C Enter a comment for the channel. This is written to the data file header.

A comment can be input by the user to describe the function of a particular channel. These data are stored as a character string in the array CHANCOM and are stored in the data file header provided by ATLAB. This comment can be retrieved by calling the subroutine DUMP-FILEHEADER and is not written to the additional data files created by ATLAD03.FOR.

C Enter a comment for the file. This is written to data file header.

A comment can be written to annotate each scan's data. Besides being written to the data file header, this character string is also written to unit number 7, which is a text file created by ATLAD03.FOR.

C Set the A/D parameters

ALSETA establishes the ADC parameters including the timing source (*i.e.*, internal clock and internal trigger), the number of channels being scanned, the actual channel numbers, and the gains corresponding to each channel.

C Check for set-up errors

The numerical value returned by the function, ALSETA, and stored at the location of the variable, STATUS, can be tested to see if it is equivalent to the value of KNORMAL (*i.e.*, = 0), which means that the set-up was successful. If a gain for any of the seven channels is not a valid value or if the gain were left indeterminate, the program will jump to the end.

C Get the acquisition rate

The maximum acquisition sample rate was determined experimentally to be 10 kHz.

C Set the sampling rate

The sampling rate is "hardwired" at 10 kHz using the function, ALSF.

C Check for sampling rate errors

The error status is again tested.

C Ask the user for the number of series conversions to complete

The user is prompted to enter the number of conversion cycles to be completed by the ADC before control is relinquished to the user once again.

C Ask for the length of time to integrate

The user is prompted to input the number of milliseconds that the integrators in the spectrum analyzer will be active. The variable, INTPERIOD, can store up to a four-byte integer constant; however, ATLAD03.FOR accepts only up to a three-digit integer value, *i.e.*, up to 999 ms.

C Ask for the SCALE FACTOR for reading the RMS voltmeter

This factor allows the user to read an analog voltage from a voltmeter or other device into channel 4 and then scale the digitized value appropriately to correspond to the actual voltage read by the meter. The DELAY constant is used to allow the relay at the input of the spectrum to settle after being closed.

C Enable digital ports 0 and 1 for output

ALEFO enables either port 0, port 1, or both for output. In this case, both ports are enabled.

C Rewind the data file

ATLAB requires that the data file be rewound prior to writing to it. ALFREW sets the pointer to the beginning of the data file.

C Declare the buffer to ATLAB

The buffer which will store the ADV's for all the channels must occupy sequential addresses within RAM memory. The board uses direct memory access (DMA) to maximize the throughput to the computer's memory. If the total throughput were critical to the outcome of the experiment, we would want the buffer size to be as large as possible. A multi-dimension array is defined under the local variable section, *i.e.*, BUFFER(NBUFFSIZE, NBUFFERS), where NBUFFSIZE = 7 and NBUFFERS = 3. The first argument allows the array to hold the data for all seven channels, and the second argument determines how many sets of data per channel, *i.e.*, words, can be stored in the array. ALFDL returns the size of the buffer in words allowed for DMA operation. In the present case, since the array size was not critical for maximum throughput (the spectrum analyzer needs to be sampled only every 100 ms), the buffer length needed to be only a couple of words long. ALDB declares a user data area as a valid I/O transfer buffer. This routine will return an integer that will define the buffer, which can subsequently be written to using the ALADS subroutine.

C Give the user a message

Self-explanatory.

C First ground the input to the SPU

The analog spectrum analyzer had an offset problem with the integrators not giving a true zero output for zero input. The solution was to include a relay at the front panel that was sent a TTL pulse by the ADC board, which grounded the spectrum analyzer input. Ten consecutive offset checks are performed, and a mean offset for each channel is computed by ATLAD03.FOR. After the relay is reopened and the actual analog voltages are computed, the channel offsets are subtracted before the analog voltage data are stored in the separate channel files. ALODV writes the digital value to the specified port. In this case, all the bits of ports 0 and 1 are set low.

C Wait to begin next cycle until delay time has elapsed

The relay needs some time to settle. Experimentally it was determined that 5 msec was sufficient.

C Make ten zero check readings

Ten checks are made for statistical reasons.

C Call the subroutine INTEGRATE

A subroutine was written in order to perform the function of controlling the four integrators of the spectrum analyzer. The integration period is passed to the subroutine via the variable INTPERIOD, the subroutine resets the integrators, begins the integration, waits for the specified duration, holds the integrator outputs, and then returns control to the main program.

C Complete one A/D scan

ALADS will start a series of A/D conversions using the previously selected channels and gains. The ADV's will be stored in the buffer previously allocated for DMA operation and given by the number stored in BUFFNUM.

C Check for errors during A/D conversion

A test of the value returned by the previous function call and stored in STATUS is used to verify that the conversion was completed error-free.

C Write the buffer to the data file

Since the buffer holds only one set of data for each channel, it must be written to a data file at the end of each series conversion. ALFWRT uses the previously opened data file DATA.DAT for writing the ADV's.

C Open the SPU unit

The relay is sent a high TTL pulse to reopen the input of the SPU and allow normal signal processing functions to occur.

C Wait until the relay settles

A delay of 5 msec is included, as before, to allow the relay to settle.

C Complete the number of cycles given by seriescount0

The user defined number of series cycles to be completed is used to perform the correct number of conversions.

C Call the subroutine INTEGRATE

See previous explanation.

C Begin SERIES A/D Conversion

See previous explanation.

C Check for errors during A/D conversion

See previous explanation.

C Write the buffer to the data file

See previous explanation.

C Display the file header contents

The subroutine DUMPFILEHEADER provides a summary of the data file contents. A time stamp of the data acquired is given along with the channels being used, their respective gains, and the number of samples recorded during the entire set of series conversions.

C Close the data file before reading

The current data file, which was opened for writing, must be closed prior to opening the file for reading.

C Open the file for reading

ALFOPN opens the data file, "DATA.DAT", for reading, and ALFREW will rewind to the start of the file.

C Read the offset voltages for each channel and get an average

Since as was described earlier, a set of ten scans are performed when the input to the SPU is grounded, this offset data must be read first, a mean offset for each channel must be calculated, and the result should be subtracted from the rest of the channel data. ADV0 through ADV3 are used as storage for the channel offset data.

C Call the subroutine READCHANNEL

This subroutine decodes the analog data value passed by the variable ADVx (where x refers to the channel number) and returns the variable ANVALx, which corresponds to the actual voltage sampled at the input of the ADC.

C Get the sums of each channel

A running sum of each channel's offset voltage is stored in variable SUMx (where x refers to the channel number).

C Get the average offset for each channel

A mean offset is calculated for each channel and is stored in variable OFFSET(x), with x representing the channel number.

C Write the offset voltages to the screen

A WRITE/FORMAT combination is used to write the channel offsets to the screen. Note that these data are <u>not</u> stored in any data files.

C Read the rest of data in four different data files, one for each channel, after subtracting the offset voltage for each channel.

The variables SUMx are all reset to zero, and another set of variables, SUMSQx, are initialized. The channel scan data are read sequentially using ALFRD, and the data values are stored in an array where the first row of the column determined by the variable BUFFCOUNT contains the data value for channel 0, etc. These data values are then decoded using the subroutine READCHANNEL, and the mean channel offsets are subtracted from each channel's analog voltage, which is stored by variable ANVALx (where x refers to the channel number). A running sum and squared sum are stored by the variables SUMx and SUMSQx.

Note: In the present version of ATLAD, the mean channel voltages, instead of the actual voltage values for each set of scans, are stored. The "C" denotation can be removed from the lines with the WRITE statements, in order to store all the voltage values.

C Calculate the mean and standard deviation for each channel

The channel mean values and standard deviations are computed using the running sum and squared sum for each channel.

C Write the mean and standard deviation to the screen

WRITE/FORMAT combinations are used to give the user channel mean and standard deviation data for each channel.

C Ask the user if he wants to continue

The user is asked whether or not he wishes to perform another set of scans using the same channels and gains. Note that ATLAD03 looks only for an "N" or an "n" response, *i.e.*, hitting <ENTER> will repeat another series of scans. If the user does not respond with an "N" or an "n", then he will be asked to annotate the next set of conversions. In addition, the user can enter a different scale factor for channel 4 if he responds to the prompt with a "Y" or a "y", otherwise the current scale factor will be used.

C Close data file

If the user decides to exit the program, the data file must be closed using ALFCLO.

C Terminate ATLAB operations

ALTERM discontinues all DMA I/O operations.

SUBROUTINE INTEGRATE(INTPERIOD)

C Disable the system clock

The subroutine begins by disabling the system clock in order to prevent any interruptions during the integration period.

C Begin RESET period

ALODV outputs a digital value to the specified port ,which in this case is port 0 and port 1. A "1" is sent to bit 0 of port 0 to reset the four integrator outputs of the SPU to 0 Volts.

C End RESET period

A "0" is sent to bit 0 of port 0 to allow the integrator outputs to change.

C Begin INTEGRATION period

A "1" is sent to bit 1 of port 0 to begin integrating the inputs to the four integrators.

C Wait until end of INTEGRATION period

The integration period passed by the variable INTPERIOD is used in a DO loop to wait for the user-defined period.

C End INTEGRATION period

A "0" is written to bit 1 of port 0 to hold the integrator outputs constant.

C Re-enable the system clock

The system clock is re-enabled before returning control to the main program.

C Return to main program

Self-explanatory.

SUBROUTINE READCHANNEL(GAIN,ADV,ANVAL)

This subroutine is passed the gain for the particular channel data value being converted from offset binary to input voltage. The conversion formula given previously is used along with the appropriate values for PFS and MFS. Once the data have been decoded, the voltage data are passed to the main program using the variable ANVAL.

OPERATION

1. Turn on the computer.
2. The computer should boot-up and automatically change to the directory ATLFOR and then run the program ATLAD03, due to the inclusion of the following lines in the AUTOEXEC.BAT file in the main directory:

```
cd atlfor
atlad03
```

3. Since ATLAD03 sends control signals on the digital ports of the ADC, the program begins by warning the user that these lines are active for output and should not be externally driven. Press "Y" or "y", and then <ENTER>.
4. The program dumps the board configuration data and begins prompting the user with:

```
Entry #1 - Channel 0
Enter desired gain [1, 2, 4, or 8]:
```

Enter the desired gain followed by <ENTER>.

5. The computer responds with:

```
Channel name:
```

after which the user may enter any combination of numbers and letters up to a total of 40 characters. Press <ENTER>.

6. Repeat steps 4 and 5 until set-up data for channels 0 through 3 are complete.

7. The user will then be prompted with:

   File Annotation:

   after which a total of 80 characters may be input.

8. The user is asked to:

   Enter the number of scans to complete:

   after which he must enter a number larger than 2 followed by <ENTER>.

9. The program sends the message "ACQUIRING DATA..." to the user.

10 The resulting channel offsets, mean values, and standard deviations are written to the screen, and the mean values are written to the files data0.dat, data1.dat, etc.

11. The user is prompted with:

   Play it again Sam [Y/N]?

   after which the user must answer with "N" or "n" to stop the ADC, otherwise the specified series of scans will be repeated.

12. Subsequent to beginning a new set of conversions, the user is asked the question:

   Do you wish to enter a new SCALE FACTOR [Y/N]?

   after which the program will ask for a real number as a scale factor only if "Y" or "y" is pressed followed by <ENTER>.

REFERENCES

Cohen, Steven C., 1975. Heterodyne detection: Phase front alignment, beam spot size, and detector uniformity. *Appl. Opt.*, **14**, 1953-1959.

Foord, R., R. Jones, J. M. Vaughan, and D. V. Willetts, 1983. Precise comparison of experimental and theoretical SNRs in CO_2 laser heterodyne systems. *Appl. Opt.*. **22**, 3787-3795.

Hecht, Eugene, 1987. *Optics*. Addison-Wesley Publishing Company.

Holmes, D. A., J. E. Korka, and P. V. Avizonis, 1972. Parametric study of apertured focused Gaussian beams. *Appl. Opt.*, **11**, 565-574.

Saleh, Bahaa E., and Malvin Carl Teich, 1991. *Fundamentals of Photonics.* John Wiley and Sons, Inc.

Self, Sidney A., 1983. Focusing of spherical Gaussian beams. *Appl. Opt.*, **22**, 658-661.

Siegman, A. E., 1966. The antenna properties of optical heterodyne receivers. *Appl. Opt.*, **5**, 1588-1594.

-----, 1986. *Lasers*. University Science Books.

Sonnenschein, C. M., and F. A. Horrigan, 1971. Signal-to-noise relationships for coaxial systems that heterodyne backscatter from the atmosphere. *Appl. Opt.*, **10**, 1600-1604.

Wyatt, Clair L., 1978. *Radiometric Calibration: Theory and Methods.* Academic Press.

Zhao, Yanzeng, Madison J. Post, and R. Michael Hardesty, 1990*a*. Receiving efficiency of monostatic pulsed coherent lidars: 1. Theory. *Appl. Opt.*, **29**, 4111-4119.

-----, 1990*b*. Receiving efficiency of monostatic pulsed coherent lidars: 2. Applications. *Appl. Opt.*, **29**, 4120-4132.